

**Machine Learning: A novel approach to infer plasma parameters from
probe measurements**

by

Akinola Olowookere

A thesis submitted in partial fulfillment of the requirements for the degree of

Doctor of Philosophy

Department of Physics
University of Alberta

© Akinola Olowookere, 2022

Abstract

The research reported in this thesis is multidisciplinary in nature. It presents the use of kinetic simulations, state of the art data analysis, and machine learning techniques to infer plasma parameters and satellite parameter from Langmuir probe measurement. Physical parameters such as plasma state variables, are generally inferred from probe measurements using analytic or empirical formulas derived by applying different approximations to physical theories. The objective of this work is to develop more accurate techniques to infer physical parameters from probe measurements under more realistic plasma conditions with quantifiable uncertainties and with a potential for incremental improvements by adding more complex physical processes. Three-dimensional particle-in-cell simulations are used to calculate the current collected by fixed-bias spherical Langmuir probes relative to the satellite under conditions of increasing realism, starting with an isolated probe attached to a guard, to probes attached to a satellite. The advantage of fixed bias probes considered in cases studied throughout this thesis, is their higher temporal and spatial resolutions, compared to the more standard mode operation where bias voltages are swept in time. The calculated currents and the plasma and satellite parameters assumed in the simulations are then used to build a solution library or synthetic data set, to construct regression models to infer parameters of interest such as the satellite potential, the density, the plasma flow velocity, and the ratio between the plasma density and the square root of the temperature. The solution library is randomly split into two disjoint sets; one to train models, and the other to validate inferences, and assess the skill of the models and quantify their uncertainties. Different approaches are used

to train models, including radial basis function (RBF) regressions, deep neural networks, and combinations of these methods with analytic estimates using the boosting ensemble learning technique, and affine transformations. In the combined approach, the parameters of interest are first estimated using analytic expressions, followed by regressions to reduce inference errors. Simple affine transformations are also applied to improve the accuracy of analytic inferences, when the Pearson correlation coefficient R with known values is high. In each case, models' inference skills are assessed using different metrics to quantify discrepancies compared with known values in synthetic data sets. The models show excellent performance with the maximum relative error ranging from 7% to 12% for the density and the ratio of density and the square root of temperature, and a maximum absolute error in the range of 0.2 V to 0.4 V for the floating potential in all the cases considered. The models are applied to in situ data, and the inferences are compared to in-situ data from satellites, with which they show excellent qualitative agreement. Finally, the agreements between the models inferences and the synthetic data values indicate that the approaches used in this thesis are promising with the advantage of producing uncertainty margins that are specifically related to the inference techniques used.

Preface

Some of the research results presented in this thesis have already been published, while others have been submitted for publication in scientific journals. Chapter 2 of this dissertation is based on two published papers 1): A. Olowookere and R. Marchand, “Fixed bias probe measurement of a satellite floating potential,” IEEE Transactions on Plasma Science, vol. 49, no. 2, pp. 862–870, 2021, and 2) A. Olowookere and R. Marchand, “Density–temperature constraint from fixed- bias spherical Langmuir probes,” IEEE Transactions on Plasma Science, vol. 49, no. 6, pp. 1997–1999, 2021. In both papers, I carried out the simulations, developed the algorithm used, constructed the models, and wrote the manuscripts under the supervision of Professor Richard Marchand. Chapter 3 is based on a manuscript titled “Inference of fixed bias probe measurements - A machine learning approach” submitted for publication in Journal of Geophysical Research - Space Physics. In this paper, I did all the simulations and training of the models, while Professor Richard Marchand provided the geometry used in the simulation. Swarm satellite experimental data used was provided by Dr. Stephan Buchert at the Swedish Institute of Space Physics, Uppsala. The manuscript was written by me, while Professor Richard Marchand contributed to the composition and editing of the manuscript. Dr. Stephan Buchert also provided feedback in the writing of the manuscript. Finally, chapter 4 is based on a manuscript titled “A new technique to infer plasma density and flow velocity, and satellite potential from ion currents collected by a segmented Langmuir probe” which has been accepted for publication in IEEE Transactions on Plasma Science. In this work, I did all the simulations and training of the models used in the analysis. I

also ran and analyzed results from a test particle code provided by Professor Richard Marchand. The manuscript was written by me with feedback from my supervisor Professor Richard Marchand.

*This Thesis is dedicated to my family:
my lovely parents, Late Mr. Akin Olowookere and Mrs. Deborah A. Olowookere,
and
my lovely wife, Adenike Olowookere.*

Acknowledgments

I give the Almighty God, the maker of heaven and earth all the praise for making it possible for me to push through my research. Starting from my application to the University of Alberta, through the processing of my study permit application up till the end of my studies, He has been a faithful God. His name is praised forever and ever.

I want to thank my supervisor, Professor Richard Marchand for his guidance, suggestion, and continuous support during my PhD program. His selfless attitude towards the success of my program is magnificent, he is indeed a great leader and mentor. I want to thank my supervisory committee members, Professor Gordon Rostoker and Professor Wojciech Rozmus, for their comments and suggestions throughout my studies. I also thank Dr. Stephan Buchert for providing part of the experimental data set used in this thesis.

My unending gratitude goes to my parents and my first teachers: my late dad, Mr. Akin Olowookere, and my mum, Mrs. Debora Ayodele Olowookere for their support, advice, and prayers. I express my most heartfelt gratitude to my beautiful wife for her support, patience, endurance, and encouragement throughout the course of my studies. You are truly the best woman any man can ask for, and favour from God. I acknowledge my lovely kids, Olabisi and Akinola Olowookere for their understanding, daddy is now free to watch movies and go for outings with you. I also want to thank my siblings: Akinlolu, Olamide, Akinyemi, and Moturayo. Growing up with you guys has been a lot of fun. You have all been a blessing to me.

I want to say a very big thank you to Prof and Dr.(Mrs) Dapo Longe, Mr. Soji

Omodogbe, Prof(Mrs) M. Ojelabi, Dr. T. T. Ibrahim, Dr. Kehinde Oyewole, and Engr. Michel Omowaye who have contributed in one way or another to the success of my studies. I want to appreciate my friends Elvis Ibadin and his family, Jumoke Verissimo for their support especially when I just arrived in Canada, and my research colleague Guandong Liu.

Finally, I want to say a big thank you to the Department of Physics and my supervisor for their financial support through teaching and research assistantships. I also want to acknowledge Compute Canada whose platform I used to carry out all the simulations used for my research.

Table of Contents

1	Introduction	1
1.1	Space environment and space weather	1
1.2	Earth’s Magnetosphere	3
1.3	Earth’s Ionosphere	3
1.3.1	Variability of the Ionosphere	6
1.4	Instruments used to study Earth’s Space Environment	6
1.4.1	Spectrometers	7
1.4.2	Ionosondes	9
1.4.3	Incoherent Scatter Radars (ISR)	10
1.4.4	Magnetometers	11
1.4.5	Langmuir probes	12
1.5	Langmuir probe theory	13
1.6	Kinetic Simulations	18
1.6.1	Particle-in-Cell	19
1.6.2	Test Particle Approach	19
1.6.3	Vlasov Approach	20
1.6.4	Hybrid Approach	20
1.7	Machine Learning	21
1.7.1	Multivariate Regression	22
1.7.2	Regression error metrics	24
1.8	Motivation	26

1.9	Thesis Outline	28
2	Fixed bias spherical Langmuir probes	29
2.1	Introduction	29
2.2	Methodology	33
2.3	Construction of Inference Models	39
2.3.1	Analytic model	40
2.3.2	Regression with Radial Basis Function (RBF)	44
2.3.3	Combination of Orbital Motion Limited (OML) Approximation and Radial Basis Function (RBF)	50
2.4	Possible experimental verification	54
2.5	Summary and Conclusions	55
3	Swarm Spherical Langmuir Probes	60
3.1	Introduction	60
3.2	Methodology	64
3.2.1	Construction of a synthetic data set	64
3.2.2	Analytic estimates	67
3.2.3	Affine Transformation	67
3.2.4	Radial Basis Function (RBF) approach	68
3.2.5	Combination of Orbital Motion Limited (OML) and Radial Ba- sis Function	68
3.3	Construction of Inference Models with Synthetic Data	68
3.3.1	Spacecraft potential	69
3.3.2	Plasma density	72
3.3.3	Density divided by the square root of the temperature	72
3.4	Application of models to in-situ measurements	75
3.4.1	Inference of in-situ floating potentials	78
3.4.2	Inference of in-situ densities	80

3.4.3	Inference of in-situ $\frac{n}{\sqrt{T_{eV}}}$	83
3.5	Training with in-situ measurements	88
3.6	Summary and Conclusion	92
4	Segmented Spherical Langmuir Probes	96
4.1	Introduction	96
4.2	Methodology	98
4.2.1	Construction of the synthetic data set	99
4.2.2	Machine Learning Approach	102
4.3	Construction of inference models	105
4.3.1	Idealised probe geometry	105
4.3.2	Proba-2 probe geometry	108
4.4	Application to Proba-2 in-situ measurements	114
4.5	Summary and Conclusions	121
5	Conclusion	124
	Bibliography	131
	Appendix A:	148

List of Tables

2.1	Simulation parameters used in the construction of the solution library.	37
2.2	Sample probe voltages with respect to background plasma, for a spacecraft floating potential ranging from -2 V to $+2$ V, assuming probes with fixed bias voltages of $+3$ V, and $+2$ V.	37
2.3	Different measures of the combined model inference skill when applied to the validation data sets, with different levels of noise.	52
3.1	Sample probe voltages with respect to the background plasma, for a spacecraft floating potential ranging from -3 V to 0 V, assuming that probes are at a fixed bias voltages of $+4$ V, and $+5$ V.	65
3.2	Simulation parameters used in the construction of the solution library.	66
3.3	Summary of discrepancies between inferred satellite potentials, with values in the synthetic data.	72
3.4	Summary of errors between inferred $n/\sqrt{T_{eV}}$ and values in the synthetic data.	76
3.5	Summary of discrepancies between inferred satellite potentials, with those reported on the Swarm data portal, over three days considered.	82
3.6	Summary of RBF density inference discrepancies with reported values from the Swarm data portal, computed over three days	83
3.7	Summary of result discrepancies from the $\frac{n}{\sqrt{T_{eV}}}$ model.	88
4.1	Simulation parameters used in the construction of the solution library.	100

4.2	List of angles θ relative to the ram direction of points considered in each meridian.	103
4.3	Summary of the metrics of similarity between neural network and RBF inferences, and reported inferences of the densities for the six segments considered.	120
A.1	Sample of the synthetic data sets for the idealise probe. I_{1-10} are the currents collected by the 10 segments, V_X and V_Y are the components of the transverse velocity, and n is the plasma density.	148

List of Figures

1.1	Illustration showing a coronal mass ejection (CME) blasting away from the sun. Such storms can produce auroras and also damage different technologies. Image Credit: NASA	2
1.2	Ionospheric electron density profile showing diurnal variation for May 5, 2002 at latitude 20° and longitude 40° using the International Reference Ionosphere (IRI) model.	5
1.3	Illustration of a hemispherical electrostatic charged particle analyzer of an electron energy spectrometer used by Goembel to determine a satellite floating potential [33].	8
1.4	Illustration of the shifts in electron spectra at positive and negative satellite potential.	9
1.5	Illustration of a Langmuir probe's current-voltage (I-V) characteristics.	14
1.6	Illustration of particle collection in the OML approximation.	16
2.1	Illustration of the two identical probes at fixed bias voltages with respect to the spacecraft.	34
2.2	Scatter plot of plasma parameters obtained using the International Reference Ionosphere (IRI) model. Parameters selected in the simulations are identified with black rectangles and one circle. The circle identifies the parameters used to produce the profiles illustrated in Fig. 2.3.	35

2.3	Cross section of the charge density profile ‘rhoAv’ in the upper half and ion density ‘dni’ in the lower half. Charge density and ion density are in SI units. The parameters used in the simulation correspond to the circle in Fig. 2.2	38
2.4	Current per surface area (A/m ²) collected by the probe and the equipotential supporting guard cylinder. The plasma parameters and voltage used in the simulation are the same as in Fig. 2.3.	39
2.5	Comparison between the satellite floating potential approximated with Eq. 2.6 and actual value in the synthetic data. The line corresponds to a perfect agreement between the two floating potentials	43
2.6	Comparison between $\frac{n_e}{\sqrt{T_{eV}}}$ obtained with Eq. 2.7 and actual value in the synthetic data, with the line corresponding to a perfect agreement. The maximum relative error (MRE), root mean square relative error (RMSrE) and correlation coefficient (R) are used as model skill metrics.	44
2.7	Comparison between floating potentials inferred with RBF using six centers and actual value in the synthetic data. The line corresponds to a perfect agreement between the two floating potentials	49
2.8	Comparison between $\frac{n_e}{\sqrt{T_{eV}}}$ inferred with RBF using six centers, and actual data in the validation set. The line corresponds to a perfect agreement.	50
2.9	Comparison between satellite floating potentials obtained from a combination of Eq. 2.6, and RBF with six centers, and potential values in the validation data set. The line corresponds to a perfect agreement between the two floating potentials. In panel <i>a</i> , no noise is added to currents in the validation set, while in <i>b</i> , <i>c</i> , and <i>d</i> , noise with a relative standard deviation $\sigma = 0.005$, $\sigma = 0.01$, and $\sigma = 0.02$ is added respectively.	53

2.10	Comparison between $\frac{n_e}{\sqrt{T_{eV}}}$ inferred with combined OML and RBF using four centers, against data in the validation set. The line corresponds to a perfect agreement.	54
2.11	Illustration of a two double-probe units at fixed bias voltages with respect to their units, which are biased to different voltages, V_1 and V_2 , with respect to the spacecraft.	56
3.1	Illustration of an approximate truncated Swarm geometry used in the simulation, as seen from the ram side. Except for the probes and the “stubs”, all satellite components are assumed to be at the same potential V_s	64
3.2	Comparison between spacecraft potentials inferred with (a) only the OML formula, and (b) a combination of OML and an affine transformation and known values in the synthetic validation set. The line corresponds to a perfect agreement between the two potentials. The maximum absolute error (MaxAE), the root mean square error (RMSE), the mean absolute error (MeanAE), and the Pearson correlation coefficient (R) are used as model skill metrics.	70
3.3	Comparison between spacecraft potentials inferred with RBF using six centers and known values in the synthetic validation set. The line corresponds to a perfect agreement between the two potentials. The maximum absolute error (MaxAE), the root mean square error (RMSE), the mean absolute error (MeanAE), and the Pearson correlation coefficient (R) are used as model skill metrics.	71
3.4	Comparison between spacecraft potentials inferred with a combination of analytic formula, and RBF with six centers, and known values from the validation set. The line corresponds to a perfect agreement between the two potentials	71

3.5	Comparison between electron densities obtained using RBF with six centers, and actual densities in the validation data set. The line corresponds to a perfect agreement between the two densities.	73
3.6	Comparison between $\frac{n}{\sqrt{T_{eV}}}$ inferred with (a) OML only, (b) a combination of OML and affine transformation, and actual data in the validation set. The line corresponds to a perfect agreement.	74
3.7	Comparison between $\frac{n}{\sqrt{T_{eV}}}$ inferred with RBF using six centers, and actual data in the validation set. The line corresponds to a perfect agreement.	74
3.8	Comparison between $\frac{n}{\sqrt{T_{eV}}}$ inferred with combined OML and RBF using six centers, against data in the validation set. The line corresponds to a perfect agreement.	75
3.9	Current collected by the +4 V probe against the current collected by the +5 V probe, for both synthetic data and in-situ data.	77
3.10	Correlation plot of RBF inferred satellite potential, and values reported on the Swarm data portal for 04/02/14, from 00:00 UTC to 23:59 UTC. The solid line corresponds to a perfect agreement.	78
3.11	Correlation plot of the combined OML-affine transformation inferred satellite potentials, and values reported on the Swarm data portal for 04/02/14, from 00:00 UTC to 23:59 UTC. The solid line corresponds to perfect agreement.	79
3.12	Correlation plot of the combined OML- RBF inferred satellite potential, and that reported on the Swarm data portal for 04/02/2014, from 00:00 UTC to 23:59 UTC. The solid line corresponds to perfect agreement.	79

3.13	Plot of satellite potential using the OML-RBF model (black), OML-affine transformation model (purple), the satellite potential reported on the Swarm portal (red), and the latitude (green) against time for a twelve-hour period on 04/02/2014. The panels show four consecutive three-hour periods from 00:00 UTC to 12:00 UTC that day.	81
3.14	Correlation plot of density inference using the RBF model and reported density on the Swarm portal for 04/02/2014, from 00:00 UTC to 23:59 UTC. The solid line corresponds to perfect agreement.	83
3.15	Plot of densities inferred using the RBF model and densities reported on the Swarm portal against time for a twelve-hour period on 04/02/2014. The panels show four consecutive three-hour periods from 00:00 UTC to 12:00 UTC that day.	84
3.16	Correlation plot of RBF inferred $\frac{n}{\sqrt{T_{eV}}}$ and calculated values from densities and temperatures reported on the Swarm portal for 04/02/2014, from 00:00 UTC to 23:59 UTC. The solid line corresponds to perfect agreement.	85
3.17	Correlation plot of the combined OML-affine transformation inferred $\frac{n}{\sqrt{T_{eV}}}$ and calculated values from densities and temperatures reported on the Swarm portal for 04/02/2014, from 00:00 UTC to 23:59 UTC. The solid line corresponds to perfect agreement.	86
3.18	Correlation plot of combined OML-RBF inferred $\frac{n}{\sqrt{T_{eV}}}$ and calculated values from densities and temperatures reported on the Swarm portal for 04/02/2014, from 00:00 UTC to 23:59 UTC. The solid line corresponds to perfect agreement.	86

3.19	Comparison between inferred $\frac{n}{\sqrt{T_{ev}}}$ using RBF models (blue colour), OML-RBF model (black colour), OML-affine transformation model (purple colour) and calculated values from densities and temperatures reported on the Swarm portal as a function of time for a twelve-hour period on 04/02/2014. The panels show four consecutive three-hour periods from 00:00 UTC to 12:00 UTC that day.	87
3.20	Correlation plot (a) of RBF inferred floating potentials with six centers and reported values on the Swarm portal, and (b) histogram of the distribution of the absolute errors in the model inferences.	89
3.21	Correlation plot (a) of RBF inferred electron densities with six centers, and reported validation values from the Swarm portal, and (b) histogram of the distribution of the relative errors in the model inferences.	90
3.22	Correlation plot (a) of RBF inferred $\frac{n}{\sqrt{T_{ev}}}$ with six centers and calculated values from densities and temperatures reported values on the Swarm portal, and (b) histogram of the distribution of the relative errors in the model inferences.	91
4.1	Illustration of the geometry of the segmented probe used in the simulation (right) and an icosahedron (left).	101
4.2	Illustration of a feedforward neural network.	105
4.3	Comparison between inferred densities using (a) neural network, (b) RBF with six centers, and actual densities in the idealised probe validation data set. The straight line corresponds to a perfect agreement between the two densities.	107
4.4	Inferred transverse velocities in the range of -1000 m/s to 1000 m/s using the neural network model for the idealised probe. The colour scale shows the absolute errors in the velocity model inference.	109

4.5	Histogram showing the distribution of the absolute error in the velocity inference model for the idealised probe.	109
4.6	Illustration of the position of the segments relative to the direction of plasma flow.	111
4.7	Inferred densities against validation data set densities for the Proba-2 synthetic data. Neural network inferences are shown on the left, and RBF inferred densities using 6 centers, on the right. The line corresponds to a perfect agreement between the two densities.	112
4.8	Comparison between satellite potentials inferred using the neural network model, and actual potentials in the synthetic data set constructed with the Proba-2 geometry. The line corresponds to a perfect agreement between the two potentials.	113
4.9	Inferred transverse velocities in the range of -1000 m/s to 1000 m/s using the neural network model, and actual velocities in the synthetic data set constructed with the Proba-2 geometry. The colour scale shows the absolute errors in the velocity model inference.	115
4.10	Histogram of the distribution of the absolute errors in the velocity inference model when applied to the synthetic data set constructed with the Proba-2 geometry.	115
4.11	Correlation plots for currents collected between pairs of currents collected by segments 2 and 3, and segments 4 and 7. The blue circles are taken from the synthetic data set, while the red squares are from Proba-2 measurements.	116

4.12 Comparison between densities inferred using the neural network model (red circles), with those reported for the guard (black circles), the upper (blue squares), and lower (green inverted triangles) density boundaries of the confidence interval. The confidence interval is calculated from the averages and standard deviations of densities reported on the Proba-2 portal for the six segments considered. The gaps in the comparison correspond to currents outside the range over which the models were trained. 118

4.13 Correlation plot of density inferences using the neural network model and reported density on the Proba-2 portal for SLPA (a) segment 1, (b) segment 2, (c) segment 3, (d) segment 4, (e) segment 5, (f) segment 7, and (g) the guard. The solid line corresponds to a perfect agreement. 119

Abbreviations & Acronyms

CME Coronal Mass Ejection.

IRI International Reference Ionosphere.

ISR Incoherent Scatter Radar.

MARE Mean Absolute Relative Error.

MaxAE Maximum Absolute Error.

MeanAE Mean Absolute Error.

MRE Maximum Relative Error.

MSE Mean Square Error.

OML Orbital Motion Limited.

PES Photoelectron Spectrometer.

R Pearson Correlation Coefficient.

R² Coefficient of Determination.

RBF Radial Basis Function.

RMSE Root Mean Square Error.

RMSrE Root Mean Square Relative Error.

Chapter 1

Introduction

1.1 Space environment and space weather

The effect of space weather on Earth-based and space infrastructures, due to the dynamic nature of the space environment, has motivated the continuous study of near-Earth space physics. The term space weather refers to the variability of the sun, which, through the interplanetary solar wind and magnetic field, affects Earth's magnetosphere, ionosphere, and surface. Abrupt changes in space weather can impact different Earth-based technologies, such as power grids, navigation systems, telecommunication equipment, and satellites in Earth orbit. The sun is the primary driving force in the variability of space weather due to its continuous release of magnetized plasma in the form of solar wind [1–7]. Solar eruptions termed coronal mass ejections (CMEs) (Fig. 1.1) can cause storms that can trigger disruptions or complete failures in Earth based infrastructures. For instance, the first large magnetic storm resulting from a CME impacting Earth magnetosphere known as the Carrington Event was reported in 1859 [8, 9]. This event led to telegraph failure in Europe, America, and some other parts of the world [10]. Other large storms, resulting in significant damage include the Québec blackout of 1989, and Sweden's power failure in 2003 [10–13]. Due to the risk posed by these storms, there is a need for reliable forecasting of these events either through the application of first-principle models, empirical models [6, 14, 15], and more recently, models relying on artificial intelligence, or machine learning

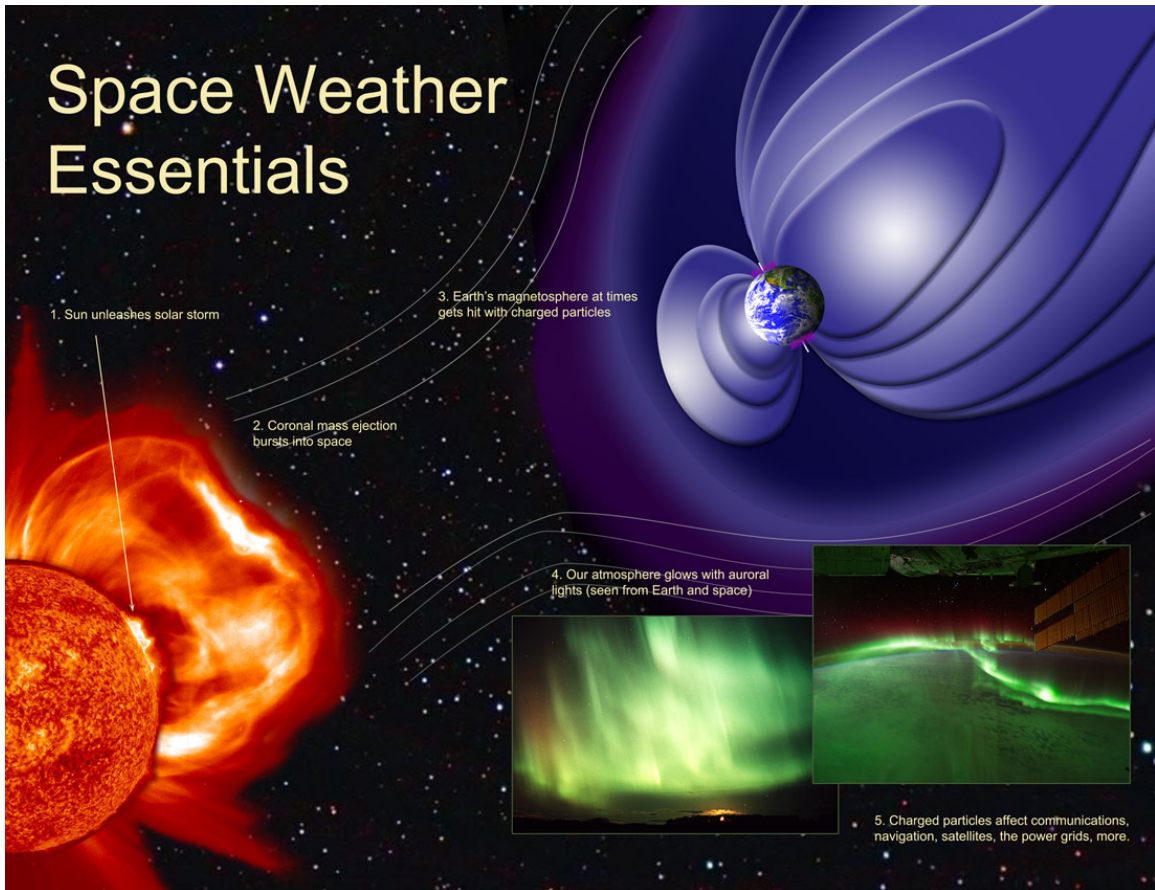


Figure 1.1: Illustration showing a coronal mass ejection (CME) blasting away from the sun. Such storms can produce auroras and also damage different technologies. Image Credit: NASA

techniques [16, 17]. These in turn will enable measures to avoid or mitigate negative impacts of extreme space weather events.

1.2 Earth's Magnetosphere

The magnetosphere is the region of space near Earth, where the magnetic field lines are connected to the Earth. It consists mainly of ionized particles that originate from Earth's ionosphere and the solar wind. It has an outer boundary called the magnetopause, which separates the magnetosphere from the interplanetary magnetic field embedded in the solar wind. The Earth's magnetosphere is distorted where the supersonic flow of solar wind encounters a bow shock, which slows down the supersonic flow to a subsonic flow of plasma behind the bow shock in the magnetosheath. The supersonic flow of the solar wind compresses the dayside of the magnetosphere and stretches out the field lines on the nightside. The solar wind plasma penetrates into the magnetosphere through reconnection at the dayside magnetopause [18]. This reconnection creates open field lines in the north and south polar cap, which are stretched out on the night side forming the magnetotail, which is a region featuring a warm plasma sheet at the center bounded by near vacuum conditions and a strong magnetic field between the plasma sheet and the magnetotail outer boundary, viz. the tail lobes [19]. The magnetotail stores enormous magnetic energy which is released during reconnection events in the form of substorms. Large storms and substorms in turn can be detrimental to satellites through spacecraft charging [20].

1.3 Earth's Ionosphere

Earth's atmosphere consists mostly of neutral gas molecules at lower altitudes, but at an altitude above 60 km, solar radiation strikes neutral gases, leading to dissociation of molecules, and ionisation of neutral particles. This region of the atmosphere where the ionization takes place is referred to as Earth's ionosphere. The ionosphere

is of great importance because of its influence on radio wave propagation due to the presence of ionized particles. The first reference to the existence of the ionosphere was made in 1839 by Gauss, who suggested that the variation in the Earth's magnetic field must be a result of an electrically conducting region in the atmosphere [21, 22]. The demonstration of the presence of a conducting medium was later confirmed when a radio signal was transmitted over a long-range from Cornwall, England to Newfoundland in Canada, by Marconi in 1901 [23]. It was concluded that the radio waves had followed the curvature of the Earth along the electrically conductive layers of the upper atmosphere [24, 25]. The ionosphere is divided into several layers or regions according to their different sources of ionisation, and density peaks as shown in Fig. 1.2. They are labeled with letters D, E, and F. The layers of the ionosphere have different characteristics such as critical frequencies, and virtual heights when they interact with radio waves. The electron density profile varies with height, time, latitude and longitude. The physical mechanisms responsible for these layers differs, as briefly described below:

The D-Layer is the lowest region of the Earth's ionosphere. It is approximately at an altitude range of 60 km to 90 km. It is sustained mainly by radiation from the sun, so it vanishes at night because of the absence of solar radiation and the recombination between electrons and positively charged ions. The layer is formed from the ionization of neutral gases such as nitric oxide NO , Nitrogen N_2 , and oxygen O_2 , by Lyman alpha radiation. Solar X-rays also contribute to the ionization process in this region.

The E-Layer is the region immediately above the D-Layer at an altitude of approximately 90 km to 140 km. The name E for this layer was chosen by Appleton [22] in reference to the electric field of waves reflected in this region. Ionization in the E-Layer is produced by extreme ultraviolet radiation and soft X-rays

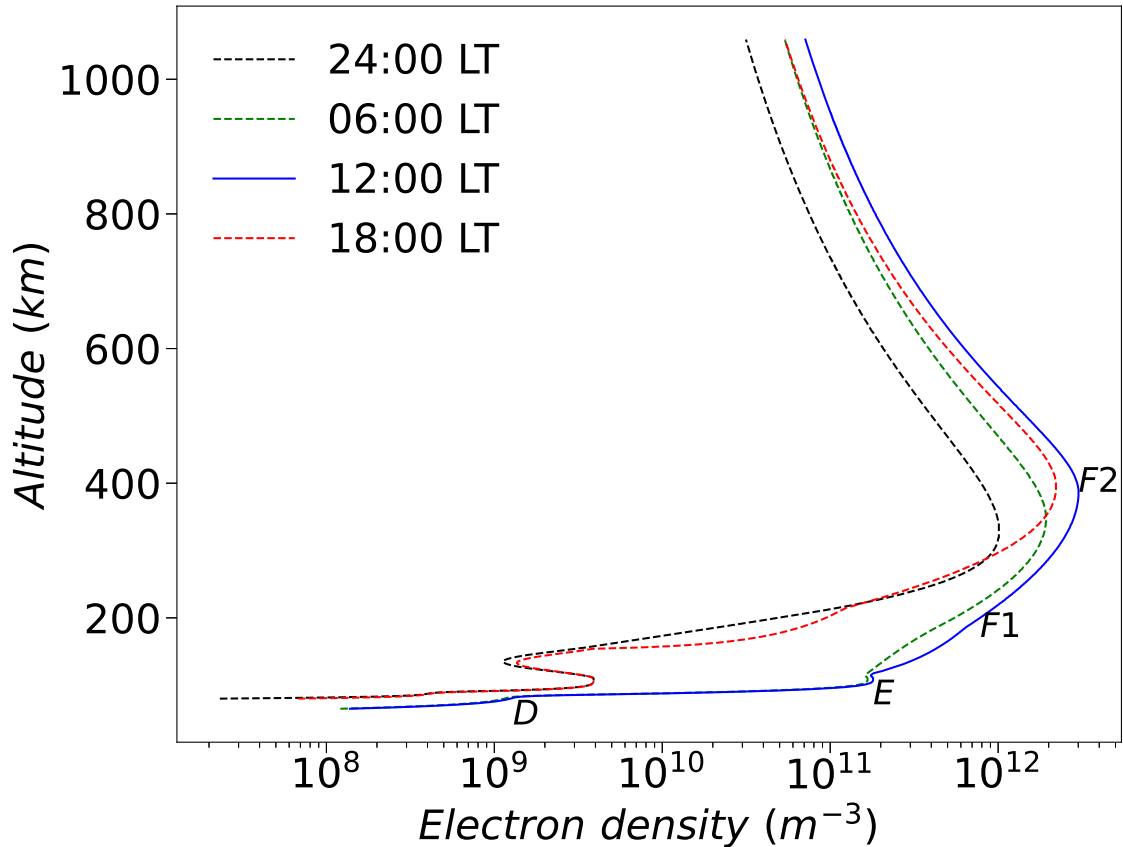


Figure 1.2: Ionospheric electron density profile showing diurnal variation for May 5, 2002 at latitude 20° and longitude 40° using the International Reference Ionosphere (IRI) model.

from the sun. Unlike the D-layer, ionization in this layer persists at night due to slower recombination rate although it is diminished.

The F-Layer extends upward above the E layer and it consists of the F_1 and F_2 regions during the day when radiation is incident from the sun. At night, the plasma density decreases in the F_1 region, which then merges with the F_2 layer which persists until dawn. The F layer is formed from the ionization of atomic oxygen by extreme ultraviolet solar radiation.

1.3.1 Variability of the Ionosphere

Earth's ionosphere is very dynamic, and it undergoes daily changes due to different processes such as the photo-ionization of the neutral gases, recombination of charged particles, and diffusion. The electron density increases during the day due to solar radiation, and it reaches its peak near 12 local noon (Fig. 1.2). As the sun sets, the production of ionized particles starts to decrease, causing a reduction in the electron density in some layers. Apart from diurnal variations which are due to the rotation of Earth on its axis, the ionosphere also undergoes seasonal variations which result from changes in the solar zenith angle or solar radiation flux, as Earth orbits around the sun. There is also a latitudinal variation of the ionosphere because solar radiation strikes the atmosphere more obliquely as the angle between the zenith and the sun (the solar zenith angle) increases. The equatorial ionosphere receives more solar radiation than the polar regions, which results in higher ionisation in the D, E, and F1 layers in the equatorial regions [26]. Solar activity which varies over a period of 11 years is another factor that plays a significant role in the variation of the ionosphere. An increase or decrease in solar activity affects the electron density in the ionosphere through an increase or decrease in the ionisation production rate.

1.4 Instruments used to study Earth's Space Environment

The Earth's space environment is impacted by space weather due to physical events such as solar flares and geomagnetic storms which induce ionospheric responses. The resulting ionospheric disturbances can impact, for example, the propagation of radio waves used in communications, Global Navigation Satellite Systems (GNSS) [27]. The monitoring of ionospheric anomalies and other physical events affecting the Earth's space environment is important in order to improve the performance of GNSS, radio communications and to have better space weather forecast models. Different types

of instruments are used to monitor the Earth’s space environment and the choice of instrument in a given study depends on the type of analysis or the physical parameter of interest. In general, the technique used in probing near Earth space environment can be classified into two categories: i) remote and ii) in situ. With remote sensing, measurements are mostly made using ground-based instruments. Conversely, in situ measurements are made in the vicinity of space plasma using instruments mounted on sounding rockets or satellites. In this section, some of the instruments used to monitor Earth’s space environment are briefly discussed.

1.4.1 Spectrometers

Spectrometers are used to separate and measure the spectral components of a physical phenomenon. Examples of this family of instruments include the mass spectrometers, which measure the distribution of particle masses in a gas, and electron or ion spectrometers which measure particle energy distributions. These devices have been deployed on rockets or low Earth orbit satellites for in situ measurements of space plasma parameters such as the density, temperature, and satellite floating potential in different missions [28–31]. For example, the Photoelectron Spectrometer (PES) which can be used to determine the floating potential of a satellite was part of the instruments on three NASA atmosphere Explorers (AE) [32]. It consists of two hemispheres as in Fig. 1.3, an electron detector, a control unit, and a data-handling processing unit [32, 33]. If the voltage difference between the hemispheres is ΔV and they are separated by δ , an electric field of approximately $\frac{\Delta V}{\delta}$ is created between them. Electrons entering through the collimator will travel to the electron detector without striking the two hemispheres only if their centrifugal force equals the electric centripetal force. For this condition to be satisfied, the electron kinetic energy to charge ratio should be $\frac{R}{2\delta}\Delta V$, where R is the mean radius of the hemispheres. Electrons with energies lower or higher than this value are collected on the inner and the outer hemisphere respectively [32]. The hemispheres are enclosed in a magnetic

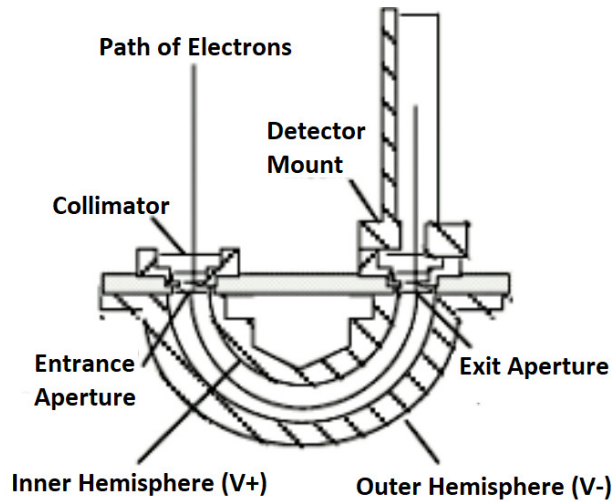


Figure 1.3: Illustration of a hemispherical electrostatic charged particle analyzer of an electron energy spectrometer used by Goembel to determine a satellite floating potential [33].

shielding material to prevent the surrounding magnetic field from distorting the path of the electrons. These magnetic shielding materials are called Mu-metal, and they are a ferromagnetic alloy with very high magnetic permeability and low coercivity. The PES is configured in such a way that the reference potential is maintained at the spacecraft chassis potential, so if the spacecraft is negatively charged, electrons will be decelerated and if it is positively charged, they will be accelerated as they enter the analyzer. Atmospheric photoelectrons are accelerated or decelerated exactly by the spacecraft potential, since the PES potential is equal to that of the spacecraft [32–34]. This causes a peak shift in the energy spectra of the photoelectrons when the satellite is positively or negatively charged with respect to as the surrounding plasma as shown in Fig. 1.4. The floating potential of the satellite is determined from the peak energy of the distribution, and the known energy peak of atmospheric photoelectrons is 23.9 eV [33]. Other plasma parameters like the plasma density and temperature can also be obtained from spectrometer measurements [35, 36]. The use of spectrometers is not limited to the study of Earth’s space environment. They have been used to study other planetary space environments, such as the Spectroscopy for

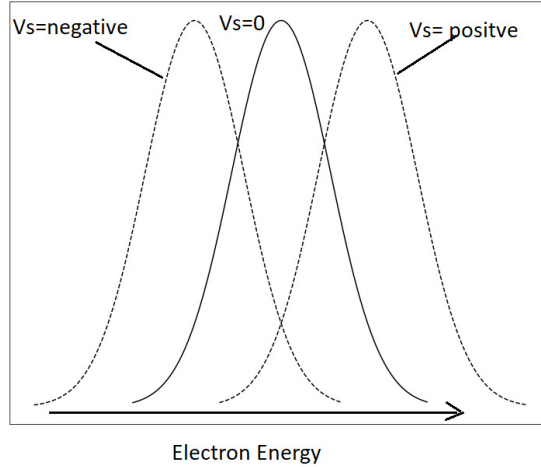


Figure 1.4: Illustration of the shifts in electron spectra at positive and negative satellite potential.

Investigation of Characteristics of the Atmosphere for Mars (SPICAM) which was flown on the European Space Agency’s (ESA) Mars Express satellite, Mars Atmosphere and Volatile Evolution Mission (MAVEN) spacecraft which carries a Neutral Gas and Ion Mass Spectrometer (NGIMS) also used to study Mars’s ionosphere, and SPICA for Venus on Venus Express in 2005 [37–42].

1.4.2 Ionosondes

Ionosondes are high-frequency radars consisting of transmitter, receiver, and antennas used to generate ionograms from which the structure and temporal evolution of the ionosphere can be inferred. They can be classified into three types: i) vertical incidence (VI) ionosondes, ii) oblique backscatter ionosondes, and iii) oblique incidence ionosondes [43]. This classification is based on the setup of the transmitter and receiver antenna. Ionosondes operate by transmitting short pulses of radio signals from the ground upward, and recording the time delay of received echoes reflected from layers of the ionosphere. The virtual heights of the reflected layers are calculated from the time delay, while the measured critical frequencies vary due to variations in the electron density in different regions of the ionosphere. Ionograms give traces

of heights (altitudes) at which the signals are reflected against frequencies of the received radio signals. Using ionogram traces, critical frequency¹ parameters foE, foF1, foF2 and virtual height² parameters h'E, h'F1, and h'F2 respectively for the E, the F1 and the F2 layers are determined. The plasma frequency as a function of altitude is also derived from ionosonde measurements by first correcting for the time delay between emission and reception of reflected pulses [44]. From the plasma frequency, the electron density can readily be obtained analytically, or numerically [45]. Ground-based ionosonde data are available only up to the plasma density maximum in the F2 region, which is mostly below satellite altitudes. This is why in-situ measurements are needed.

1.4.3 Incoherent Scatter Radars (ISR)

These are ground-based instruments used to measure electron density profiles, electron and ion temperature profiles in the ionosphere. The ISR technique was first developed by Gordon [46], who proposed the use of Thomson scattering of transmitted high power radio waves to sound the ionosphere. With this approach, radio waves are transmitted in the high to ultra-high frequencies, and they scatter incoherently on plasma electrons and ions in the ionosphere. The radio signals are scattered at a lower frequencies due to Doppler shifts and their wavelengths are not in phase. The radar receiver records spectra of scattered waves, from which the electron temperature, ion temperature, and electron density can be inferred [47–52]. An advantage of the ISR as a ground-based instrument is the possibility to monitor a single location in the ionosphere over a long period of time resulting in measuring signature of events in a fixed frame of reference. Another advantage is that, unlike ionosondes, ISR measurements are not limited to the bottom side of the ionosphere, below the electron density maximum, because they are applicable to lower densities above that

¹This is the highest magnitude of frequency at which radio waves are reflected from ionosphere layers.

²This is the height at which recorded radio waves are reflected from different ionosphere layers.

maximum density height. Several ISRs have been developed over the years to study the Earth's ionosphere which has helped researchers have a better understanding of the ionosphere. Examples include Arecibo in Puerto Rico(now decommissioned), Jicamarca in Peru, and Resolute Bay (RISR) in Canada [50, 53–57].

1.4.4 Magnetometers

Magnetometers are instruments used to measure the magnetic field. They come in two varieties; scalar magnetometers used to measure only the magnitude of the ambient magnetic field and vector magnetometers, which measure both the magnitude and the direction of the magnetic field. These instruments are particularly important in space research due to the significant effect of the geomagnetic field on both space and ground-based infrastructures. Different magnetometers have been deployed in different space missions to monitor the geomagnetic field and other physical phenomena associated with it. For example, data obtained with the Geostationary Operational Environmental Satellite (GOES) magnetometer are used to monitor daily variations of the Earth's magnetic field, to assess the level of geomagnetic disturbances, and to detect magnetopause crossings by a spacecraft, which are used to improve space weather forecasting and monitoring [58, 59]. Another example is the Swarm satellites, which carry both the Vector Field Magnetometer (VFM) which measures the magnetic field vector, and the Absolute Scalar Magnetometer (ASM) used to measure the magnetic field strength to calibrate the VFM [60]. Magnetometers can also be deployed as ground-based instruments to measure variations in surface magnetic fields, associated with changes in current systems in the ionosphere and magnetosphere. Examples include i) the fluxgate magnetometer at Jicamarca used to monitor processes leading to ionospheric anomalies such as equatorial spread F in response to geomagnetic storms, and the determination of the $\vec{E} \times \vec{B}$ drift velocities [61–63], and ii) the Canada Array for Realtime Investigations of Magnetic Activity (CARISMA) which consists of an array of magnetometers used to measure disturbances in the Earth's

magnetic field [64].

1.4.5 Langmuir probes

A Langmuir probe is an electrode which, when inserted into plasma and biased to different voltages, collects currents from plasma ions and electrons. Langmuir probes come in different geometries, including spherical, cylindrical, and planar geometries. The determination, or inference of physical parameters from probe measurements, relies on the relation between collected currents and probe bias voltages relative to a reference object called the “common” or “ground”. In space, the ground is usually the satellite or rocket bus, and the relation between collected current and bias voltage is referred to as the current-voltage (I-V) characteristic. The probe collects mostly electron current when the bias voltage V_b is more positive than the plasma potential V_p ($V_b > V_p$), and ion current when $V_b < V_p$. There are different parts or regions in the I-V characteristics of a probe as illustrated in Fig. 1.5 from which different plasma parameters can be determined:

The ion saturation region is the region where the probe is mainly collecting ion currents; i.e., the probe potential is sufficiently negative so as to prevent most electrons from being collected, and it mostly collects ions.

The floating potential V_f is the potential at which the ion and electron currents collected by the probe are equal, which implies that the net current collected is zero.

The plasma potential V_p is the potential of the background plasma relative to the satellite.

The transition region is the region of the I-V characteristics where the probe potential is greater than the floating potential but less than the plasma potential; i.e., $V_f < V_b < V_p$. The ion current is negligible in this region and the electrons

are partially repelled. In a Maxwellian plasma, the collected current grows exponentially until the probe potential reaches the plasma potential.

The electron saturation region is where the probe potential V_b is greater than the plasma potential. In this region, the electron current grows linearly with the probe voltage.

Langmuir probes are commonly used instruments in space research, and they have been flown on different scientific satellites such as Dynamics Explorer, Proba2, and Swarm [65–67]. In this thesis, I present novel techniques with a potential to make better inferences of plasma and satellite parameters from Langmuir probe measurements, for selected probe geometries, and operating conditions. A brief overview of the current techniques used to infer plasma parameters is therefore presented in the next section, as background and reference, for the novel approaches to be presented in the following sections.

1.5 Langmuir probe theory

As mentioned previously, when a probe is biased at a potential greater than the plasma potential, it collects mostly electrons, while if it is at a potential sufficiently lower than the plasma potential, ions are collected, while only electrons with enough energy to overcome this potential barrier are collected by the probe. The attraction and repulsion of charged particles from the probe leads to the formation of a plasma sheath, which is a region where plasma quasi-neutrality breaks down. The surrounding charged particles in that region redistribute themselves so as to shield the electric field induced which would otherwise exist, due to the probe’s presence. For a spherical probe in a stationary and thermal plasma, the resulting potential extends in the plasma at a distance of the order of few Debye lengths λ_D , and it is written as

$$V(r) = V_0 \frac{R}{r} \exp\left(-\frac{r-R}{\lambda_D}\right), \quad (1.1)$$

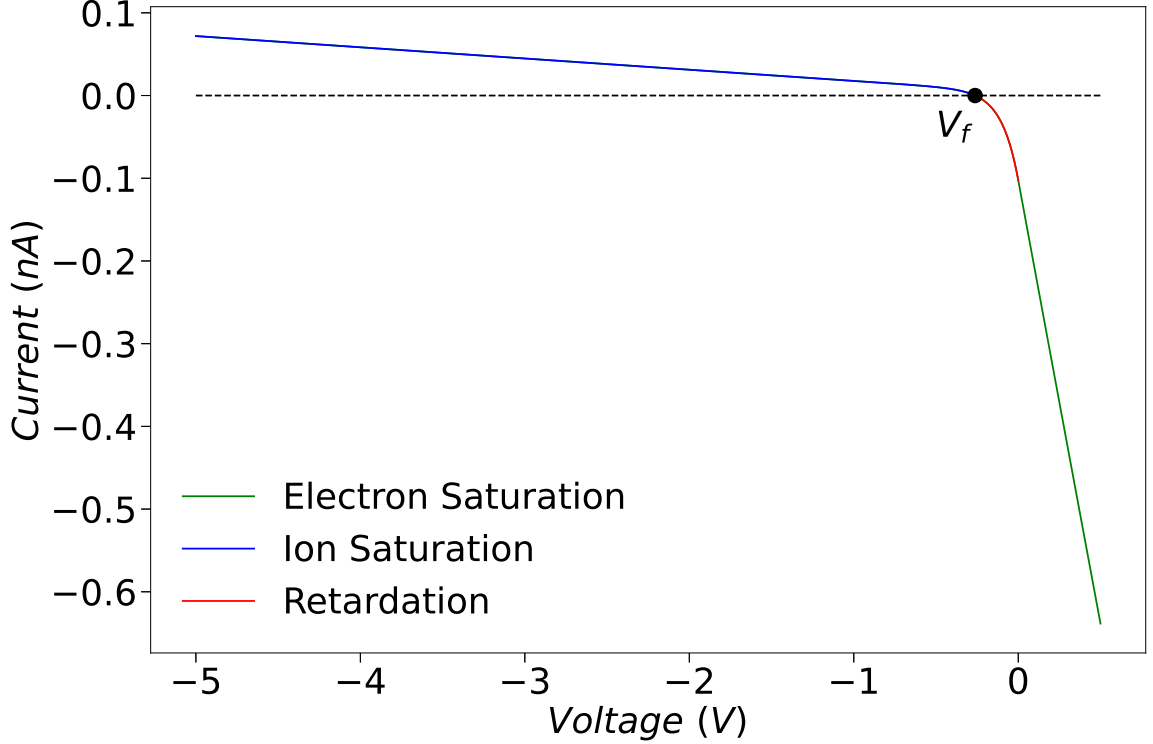


Figure 1.5: Illustration of a Langmuir probe's current-voltage (I-V) characteristics.

where V_0 is the potential on the sphere surface, R is its radius, and $V(r)$ is the potential at distance r from the probe center. The effective Debye length in plasma consisting of a single ion species is given as

$$\lambda_D = \left(\frac{1}{\lambda_{De}^2} + \frac{1}{\lambda_{Di}^2} \right)^{1/2}, \quad (1.2)$$

where $\lambda_{De} = \sqrt{\epsilon_0 k T_e / e^2 n_e}$ and $\lambda_{Di} = \sqrt{\epsilon_0 k T_i / Z e^2 n_i}$ are the electron and ion Debye lengths, ϵ_0 is the permittivity of free space, k is the Boltzman constant, T_e is the electron temperature, T_i is the ion temperature, e is the elementary charge, Ze is the ion charge, n_e and n_i are the electron and ion densities respectively. The current collected by a Langmuir probe is not only dependent on the probe potential with respect to the background plasma, but also on different characteristic lengths including the probe radius, and the thickness of the plasma sheath. In a magnetised plasma, the gyration of electrons and ions around field lines can also influence the current, as well as the collision mean free paths between charged particles or charged particles

and neutral atoms and molecules in a collisional and weakly ionized plasma. Collected currents can also be affected by the proximity to the wake and other satellite components. While several theories have been developed to describe currents collected by Langmuir probes, under different idealized conditions, none are capable of accounting for all these physical conditions and processes, which is why theories are based on several simplifying assumptions. One commonly used approach is based on the orbital motion limited (OML) theory derived a century ago by Mott-Smith and Langmuir [68, 69], leading to relatively simple analytic expressions for the current collected by probes as a function of the probe voltage, and plasma parameters. In the OML approximation, the following assumptions are made:

- Plasma is assumed to be collisionless and the radius of the probe, to be very small compared to the Debye length.
- The energy and the angular momentum of a charged particle is conserved as it approaches the probe.
- The plasma is not magnetised.
- The surface of the probe is far from any objects which could intersect or deflect incoming particles.
- All particles species are often assumed to have Maxwellian velocity distribution functions given as

$$f(\vec{v}) = n \left(\frac{m}{2\pi kT} \right)^{3/2} \exp \left(-\frac{m |\vec{v} - \vec{v}_d|^2}{2kT} \right), \quad (1.3)$$

where m is the mass of the particle, n is the particle density, T is the temperature, k is the Boltzman constant, and \vec{v}_d is the drift velocity.

The current collected by a spherical probe due to the contribution of each particle species is obtained from the flux of charges through the effective surface area of the probe, that is

$$I_s = q_s \int A_{eff} \vec{v} \cdot \hat{n} f_s(\vec{v}) d^3v, \quad (1.4)$$

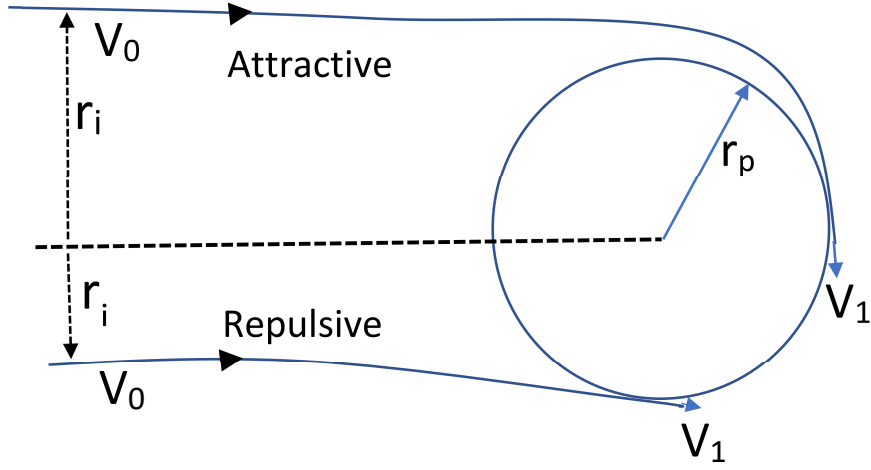


Figure 1.6: Illustration of particle collection in the OML approximation.

where s denotes the particle species, A_{eff} is the effective surface area of the probe, q_s is the particles charge, v_s is the velocity, and \hat{n} is the unit vector pointing into the sphere. In the OML approximation, the effective cross-sectional area of the probe is a function of the incoming particles' speed, and probe bias voltage. The effective collection area A_{eff} can be determined from the conservation of particle energy and angular momentum. Specifically, let r_i be the largest impact parameter for which a particle moving with speed v_0 far from a probe, would be collected at a grazing angle, while all particles with impact parameter $r < r_i$ and the same initial speed, would hit the surface of the probe and be collected (Fig. 1.6). Making use of particle energy and angular momentum conservation, we write

$$\frac{1}{2}mv_0^2 = \frac{1}{2}mv_1^2 + qV, \quad (1.5)$$

and

$$mv_0r_i = mv_1r_p, \quad (1.6)$$

where qV is the particle electric potential energy at the sphere. From equation 1.5 and 1.6, an expression for the maximum impact parameter and the effective cross-section area are obtained, and they are given as

$$r_i = r_p \sqrt{1 - \frac{2qV}{mv_0^2}}, \quad (1.7)$$

and

$$A_{eff} = A_p \left(1 - \frac{2qV}{mv_0^2}\right), \quad (1.8)$$

where $A_p = \pi r_p^2$ is the geometrical probe cross section. Following a similar approach as in [70], an analytic formula is derived for the net current collected by the probe as follows: equation 1.8 is substituted in equation 1.4 for the effective cross-section area, and the current I_{att} collected from attracted species is obtained by performing the integration below in spherical coordinates

$$I_{att} = q \int_0^{2\pi} d\phi \int_0^\pi \sin \theta d\theta \int_0^\infty v^2 f(\vec{v}) A_{eff} v dv, \quad (1.9)$$

where A_{eff} is a function of V and v . Assuming a drifting Maxwellian distribution function as in Eq. 1.3 and substituting for A_{eff} , we find

$$I_{att} = qn\pi r_p^2 \left(\frac{m}{2\pi kT}\right)^{3/2} \int_0^{2\pi} d\phi \int_0^\pi \sin \theta d\theta \int_0^\infty v^2 \exp\left(-\frac{m|\vec{v} - \vec{v}_d|^2}{2kT}\right) \left(1 - \frac{2qV}{mv^2}\right) v dv, \quad (1.10)$$

where the drift velocity \vec{v}_d is assumed to be along the z axis for simplicity. Integrating equation 1.10, the current I_{att} is of the form

$$I_{att} = \pi r_p^2 qn \left(\frac{2kT}{\pi m}\right)^{1/2} \left[e^{-x_d^2} + \left(1 + 2x_d^2 - \frac{2qV}{kT}\right) \frac{\sqrt{\pi} \operatorname{erf}(x_d)}{2x_d} \right], \quad (1.11)$$

where $x_d = \frac{v_d}{\sqrt{2kT/m}}$. The same procedure is used for repelled species. In this case, however, the integration over speeds must be over sufficiently large values, for the

particle to overcome the repulsive potential of the probe qV . The current I_{rep} from repelled species is then calculated with

$$I_{rep} = q \int_0^{2\pi} d\phi \int_0^\pi \sin\theta d\theta \int_{v_m}^\infty v^2 f(\vec{v}) A_{eff} v dv, \quad (1.12)$$

where $v_m = \sqrt{\frac{2qV}{m}}$ is the minimum speed far from the probe, for a particle to have sufficient energy to be collected. Substituting equation 1.3 for $f(\vec{v})$ and equation 1.8, we find

$$I_{att} = qn\pi r_p^2 \left(\frac{m}{2\pi kT}\right)^{3/2} \int_0^{2\pi} d\phi \int_0^\pi \sin\theta d\theta \int_{v_m}^\infty v^2 \exp\left(-\frac{m|\vec{v} - \vec{v}_d|^2}{2kT}\right) \left(1 - \frac{2qV}{mv^2}\right) v dv. \quad (1.13)$$

The integration in equation 1.13 yields the current I_{rep} for a repelled species given as

$$I_{rep} = \pi r_p^2 qn \left(\frac{2kT}{\pi m}\right)^{1/2} \left\{ \frac{x_d + x_m}{2x_d} e^{-(x_d - x_m)^2} + \frac{x_d - x_m}{2x_d} e^{-(x_d + x_m)^2} + \left[\frac{1}{2} + x_d^2 - \frac{qV}{kT} \right] \frac{\sqrt{\pi} \operatorname{erf}(x_d - x_m) + \operatorname{erf}(x_d + x_m)}{2x_d} \right\}, \quad (1.14)$$

where $x_m = \sqrt{\frac{qV}{kT}}$. Finally, the net current collected by the probe is obtained by adding 1.11 and 1.14 for all species involved. A similar expression for the net current was reported by Whipple, who attributed the derivation to Hinteregger and Kana1 [70].

1.6 Kinetic Simulations

Kinetic simulations are useful to study and understand the interaction of space plasma with satellites and instruments. These methods are applicable not only to space plasma, but also to laboratory plasma experiments [71]. They have been used to describe micro-scale phenomena in plasma such as the interaction of charged particles with waves, collisionless shocks, and magnetic reconnection [72–76]. Different approaches used in kinetic simulations are now briefly reviewed.

1.6.1 Particle-in-Cell

Particle-in-Cell (PIC) simulations are commonly used to simulate plasma dynamics. The PIC approach involves tracking charged particles' motion in their self-consistent fields, calculated from the charges and current densities created by the particles themselves. PIC simulations are used to study a variety of physical problems in the field of plasma and space physics such as the interaction of spacecraft with its environment [77], the study of plasma fusion [78, 79], and particle accelerators [80]. In this approach, the simulation domain is discretized using either a structured or an unstructured mesh. The fields are calculated on the vertices of these meshes at each time step, after which they are interpolated to the particle positions. The calculated fields are then used to advance particle positions and velocities, in time. Plasma densities are specified at the start of the simulation. However, a typical electron density in ionospheric plasma is of the order of $n_e \sim 10^{12} \text{ m}^{-3}$, which is too large and computationally expensive for tracing every particle, in a typical simulation domain of volume, which could extend to several cubic metres. In practice, simulations are therefore made using fewer “macro-particles”, which can represent a large number of particles in a given system. Each macro-particles has a statistical weight (w) equal to the ratio between the number of physical particles in a given volume, to the number of macro-particles used in a simulation, that is,

$$w_s = \frac{V n_s}{N_s}, \quad (1.15)$$

where V is the volume of the simulation domain, n_s is the density of species s , while N_s is the total number of macroparticles of species s .

1.6.2 Test Particle Approach

Test particle simulations are used to study plasma particles when their trajectories or velocity (energy) distribution functions are of interest. It has been used by different researchers to understand the behaviour of charged particles in space environments.

For example, it was applied to investigate the interaction of radiation belt electrons with magnetosonic waves [81], and the determination of particle distribution functions in the magnetotail [82–84]. In test particle simulations, the fields are specified a priori, which makes the approach not self-consistent. Test particle simulations can also make use of Liouville’s theorem in a collisionless plasma, which states that the particle velocity distribution function $f(\vec{r}, \vec{v}, t)$ remains constant along the particle trajectory in 6-dimensional phase space. There are different approaches to implementing test particle simulations, including; (i) Particle trajectory sampling, (ii) Forward Monte Carlo, (iii) Forward Liouville, and (iv) Backward Liouville. These four approaches have been described and illustrated by Marchand 2010 [85].

1.6.3 Vlasov Approach

In the Vlasov approach, the system of particles at a given time is described by the distribution function $f(r, v, t)$ in 6-dimensional phase space consisting of positions and momenta (or velocities). The method involves solving the Vlasov equation

$$\frac{\partial f_s}{\partial t} + \mathbf{v} \cdot \frac{\partial f_s}{\partial \mathbf{r}} + \frac{\mathbf{F}}{m} \cdot \frac{\partial f_s}{\partial \mathbf{v}} = 0, \quad (1.16)$$

for the distribution function f_s of a given particle species s in a collisionless plasma, where \mathbf{F} is the Lorentz force [86, 87]. Particle number densities and velocities are computed from the velocity distribution functions, and these are used in Maxwell’s equations to compute electromagnetic fields self-consistently. One of the advantages of the Vlasov approach over PIC approach is the absence of statistical noise due to the use of a finite number of discrete particles used in the PIC approach [88].

1.6.4 Hybrid Approach

The hybrid approach combines both the fluid and the kinetic approaches. In this method, some plasma species are treated kinetically, while others are treated in the fluid approximation [89, 90]. The electromagnetic fields used are calculated self con-

sistently by solving Poisson’s equation and/or Maxwell’s equations. The hybrid approach can be a combination of fluid and PIC, i.e hybrid fluid-PIC [91], or with Vlasov as hybrid fluid-Vlasov [92]. In the hybrid fluid-PIC, macro-particles are used instead of the actual physical particles as in the standard PIC approach. These particles are advanced in time using self-consistent fields computed from charge and current densities obtained from the particle distribution functions and the solutions to the fluid equations used in the model. The approach used to determine the distribution functions introduces statistical noise in the simulation. Conversely, in the hybrid fluid-Vlasov, there is no statistical noise either from the fluid, or the Vlasov contribution to the electromagnetic field. Particle distribution functions are obtained from the solution of the Vlasov equation at each time step, making the distribution functions noiseless compared to hybrid fluid-PIC [86].

1.7 Machine Learning

The use of machine learning has increased in recent years in all fields of life for analyzing and interpreting data [93–95]. In physical sciences, the use of machine learning has opened up new methods of comparing simulations and experiments, for instance, in data analysis, space weather forecasting and predictions [96, 97]. Machine learning methods are classified into supervised and unsupervised learning methods. The supervised approach involves the construction of inference or predictive models using pre-labeled data sets. In this method, the input data which are often referred to as the predictors (or independent variables), and the output data (responses or dependent variables) are specified in the model training process. Supervised learning can further be subdivided into a regression problem, which requires the prediction of continuous values based on the input values, and a classification problem which involves the identification of discrete output variables. Unsupervised learning makes use of an unlabeled data set, that is, only the input data are involved. Models are constructed to learn the relationship and structure between inputted data. This type of learning

technique is used mostly for clustering or grouping data based on their relationship or structure [98]. It can also be used for dimensionality reduction when dealing with data sets of very high dimensions. Several machine learning algorithms are used to solve different problems. Some examples are linear regression, radial basis function, support vector machine, deep neural network, Gaussian clustering, and K-clustering [99–102]. The selection of an algorithm for a specific problem depends on the nature of the problem. For instance, in a problem that requires prediction or inference of a numerical value based on prior learning, regression based algorithms are used. But in a problem in which prediction of data categories is done, classification algorithms such as support vector machine, and random forest are used [103]. Another key component in machine learning is model evaluation. There are several evaluation metrics used and here again, the choice depends on the nature of the problem. In classification, model evaluation is generally done using metrics such as accuracy, recall, precision, F1-score, and confusion matrix [104, 105], while in regression, the mean absolute error, the mean square error, the r-square, etc. are used [103]. Machine learning has also found many applications in the study of space weather. For example, it has been used for solar activity forecasting [106, 107], prediction of solar flares [108, 109], of ionospheric scintillation, and classification of plasma regions in near Earth space [110, 111]. In this thesis, the regression approach is used to construct inference models for different plasma and satellite parameters. Brief descriptions of how regression methods are constructed and metrics used to assess the skill of the model follow. However, detailed descriptions of the regression algorithms used in this thesis are explained in later chapters.

1.7.1 Multivariate Regression

In general, the use of multivariate regression algorithms can be done in two ways. The first involves the construction of a predictive (inference) model using one of the regression-based algorithms. The other approach combines two or multiple models

trained using the same regression algorithm or different algorithms. This procedure of constructing a predictive model is referred to as ensemble learning strategy [103]. The advantage of using an ensemble approach is that it reduces both the bias and the variance in a predictive model, leading to improvement in the model skill. The ensemble learning strategies are mostly done using three different techniques, namely bagging, boosting, and stacking and they are briefly described below.

Bagging Ensemble Learning This approach derives its name from “bootstrap aggregation”. It uses multiple samples of a training data set obtained using a bootstrap approach to construct multiple base learners that form an ensemble for prediction [112]. The bootstrap approach involves random sampling of the training data set with replacement, which means that if an observation is selected in a given sample, the observation is returned to the data for possible re-selection. Predictive models are then constructed for each of the selected samples, and the final prediction is obtained from averaging predictions made by all these models.

Boosting Ensemble Learning In this type of ensemble learning, the major aim is to develop a strong learner by combining multiple lower skill learners. The main component of boosting ensemble learning is to correct the errors made by a first predictive model. This is done iteratively by constructing a model to correct error, in a preceding model inference. That is, a first model is trained using the training data set, the errors are calculated from the differences between these first inferences, and known values in the training set, and a second model is constructed which corrects errors in the first and the third model corrects errors in the second, and so on. The final model is obtained from a combination of all the models.

Stacking Ensemble Learning This involves training multiple models on a single training data set followed by training a final model to aggregate the predictions

of all the multiple models. In this ensemble approach, each model in the multiple models is called the first-level learner, while the model used to aggregate their predictions is called the second-level learner, or meta-learner. Any machine learning algorithm can be used as the meta-learner, but it is better to use a simple model such as the linear regression, so that the complexity of the model resides at the first level [113].

1.7.2 Regression error metrics

The main objective, when training regression models, is to minimize the errors in the model's predictions. In practice, there are different metrics being used to assess the performances of a model. Some of these metrics are mentioned below:

Maximum absolute error (MaxAE) This is the maximum value of the absolute residual error i.e the difference between the inferred values and the actual data values. It is of the form

$$\text{MaxAE} = \max(|Y_{inf} - Y_{dt}|), \quad (1.17)$$

where Y_{inf} and Y_{dt} are respectively inferred values and the known values in the data set. Minimising the MaxAE brings down the uncertainties in the model to the most conservative value.

Mean absolute error (MeanAE) This measures the average magnitude of the residual error in a model inferences, and it is of the form

$$\text{MeanAE} = \frac{1}{n} \sum_{j=1}^n |Y_j^{dt} - Y_j^{inf}|. \quad (1.18)$$

Maximum relative error (MRE) This is the maximum value when the absolute difference between the inferred and data values is normalized with the inferred value as in

$$\text{MRE} = \text{Max} \left| \frac{Y_{dt} - Y_{inf}}{Y_{inf}} \right|. \quad (1.19)$$

It is recommended when data values all have the same sign, and vary over more than one order of magnitude. Note that in this definition of the relative error, the inferred value Y_{inf} rather than the known value Y_{dt} from the data set appears in the denominator. This is to facilitate the interpretation of relative uncertainties, considering that exact values are generally not known, while inferred values are known from model inferences.

Root mean square error (RMSE) This gives an absolute measure of lack of fit of the model; that is, it provides the standard deviation of the model inferences from the actual values. It is calculated using

$$\text{RMSE} = \sqrt{\frac{1}{n} \sum_{j=1}^n \left(|Y_j^{dt} - Y_j^{inf}| \right)^2}. \quad (1.20)$$

Root mean square relative error (RMSrE) This gives the root mean squared error of the normalized square of the residual error as in

$$\text{RMSrE} = \sqrt{\frac{1}{n} \sum_{j=1}^n \left(\frac{Y_j^{dt} - Y_j^{inf}}{Y_j^{inf}} \right)^2}. \quad (1.21)$$

Coefficient of determination or R-square (R^2) This measures the proportion of the variance in the dependent variable that is accounted for in the inference model. It is calculated using

$$R^2 = 1 - \frac{\sum_{j=1}^n (Y_j^{dt} - Y_j^{inf})^2}{\sum_{j=1}^n (Y_j^{dt} - Y_{mean})^2}, \quad (1.22)$$

where Y_{mean} is the mean value of the dependent variable in the data set. The value of R^2 is between 0 and 1, with a value close to 1 indicating that a large fraction of the dependent variables in the data set are well approximated by the model. Conversely, a value close to zero, corresponds to model with low predictive skills.

Pearson correlation coefficient (R) This measures the linear relationship between two variables. It is defined as

$$R = \frac{\sum_{j=1}^n (X_j - X_{mean})(Y_j - Y_{mean})}{\sqrt{\sum_{j=1}^n (X_j - X_{mean})^2} \sqrt{\sum_{j=1}^n (Y_j - Y_{mean})^2}}, \quad (1.23)$$

where X_j and X_{mean} are the values and mean of X-variables, and Y_j and Y_{mean} are the values and mean of Y-variables respectively. R has a value between -1 and 1, where -1 indicates a strong negative correlation between the two parameters, that is as one of the parameters increases, the other decreases. The value 1 indicates a strong positive correlation, while 0 indicates no correlation. R is not a measure of model accuracy, but a measure of affinity between model inferences and the actual data. An affine transformation can usually be used to improve the accuracy of a model if its affinity with data is strong; that is, if there is strong affinity (i.e R is close to 1 in absolute value) between the inferences and the actual data. An interesting property of this coefficient, is that it is invariant under an affine transformation applied to any one of the two sets. It follows that with a high $|R|$, it is often possible to improve the accuracy of a model with a simple affine transformation.

1.8 Motivation

Langmuir probes are one of the most commonly used instruments in space research to monitor plasma state parameters such as the density, the temperature, and the satellite potential. Like other instruments, probes don't directly measure physical quantities of interest. Instead, they provide "low level" measurements such as collected currents as a function of voltage, from which these physical quantities must be inferred. These inferences in turn are practically always based on theories leading to analytic solutions or empirical formulas. Several analytic solutions have been used to infer plasma parameters under different plasma conditions [68, 69, 114–117]. However, these inferences mostly come with unquantified uncertainties as a result of the

approximation made to derive analytic formulas. The objectives of this thesis are to:

(1) Develop new approaches that can be used to infer plasma and satellite parameters from fixed bias probe measurements under more realistic plasma conditions than what is possible with analytic or empirical formulas using different probe geometries.

(2) Develop a systematic strategy to quantify uncertainties, or confidence intervals in model inferences.

(3) Develop approaches for which it is possible to make incremental improvements, by accounting for more specific physical processes or geometrical features, in a given problem.

These objectives are achieved by:

(a) Using kinetic simulations to calculate currents collected by different Langmuir probe geometries. In the simulations, different ionospheric plasma conditions are accounted for, including different plasma ion species, satellite potentials, and the presence or absence of the satellite.

(b) Simulation results are then used to construct solution libraries containing plasma and satellite parameters used in the simulations, and the calculated currents.

(c) The solution library is then randomly divided into two distinct sets. One, the training set, is used to construct inference models for plasma and satellite parameters, while the other, the validation set, is used to validate the skill of the models and also to quantify the uncertainty in each of the model inferences.

(d) Considering Langmuir probes operating at fixed voltages, because of their relative simplicity, and their advantages of providing measurements with significantly higher temporal and associated spatial resolution, rather than measurements made with a swept-voltage probes.

1.9 Thesis Outline

The remainder of my thesis is organized as follows. Chapter 2 describes a simple concept of applying a combination of kinetic simulation of an isolated spherical Langmuir probe, analytic formulas, and regression techniques to infer plasma and satellite parameters from probe measurements. This concept is extended in Chapter 3 by considering the presence of a satellite. This is achieved by carrying out kinetic simulations for two Langmuir probes on a satellite using a truncated simplified Swarm satellite geometry. The currents calculated from the simulations with known plasma and satellite parameters used as input in the simulations are used to train models for the satellite potential, the electron density, and the electron density divided by the square root of the electron temperature. The trained models are applied to Swarm A in situ measurements. In Chapter 4, I explore the use of kinetic simulation and multivariate regression methods to infer plasma and satellite parameters from spherical segmented Langmuir probe measurements. Chapter 5 gives a summary and conclusion of the thesis.

Chapter 2

Fixed bias spherical Langmuir probes

This chapter is based on two published papers in peer-reviewed journals [118, 119]. A simple sensor to measure satellite potential and the ratio between the plasma density and the square root of the electron temperature is described. The proposed instrument consists of two small spherical Langmuir probes biased to different fixed voltages, from which currents are measured. Inference models are constructed for spacecraft floating potentials and the ratio of the plasma density and the square root of the electron temperature by combining the orbital motion limited (OML) approximation for the current collected by a spherical probe, and a multivariate regression algorithm. The construction of the models is based on a training data set obtained from 3-D simulation results, covering a range of plasma parameters of relevance to satellites in low earth orbit (LEO) at mid-latitudes. The models' skills are then assessed by comparing inferences with values in a distinct validation data set.

2.1 Introduction

Charging and resulting electric potentials are an important process affecting the state of spacecraft and their interaction with their environment. Satellite charging is caused by a combination of plasma particle collection, photoelectron emissions, and sec-

ondary electrons due to energetic electron and ion impact. Charging generally occurs at conducting surfaces, and when satellites are exposed to fluxes of energetic particles, charged particles can also penetrate satellites and cause “deep dielectric charging”. In the presence of large internal charging, electrostatic discharges can occur and damage sensitive electronic components. Discharges can also occur between different surface components when they are at significantly different potentials[120, 121].

Even in the absence of physical damage, charging is of concern when interpreting measurements involving charged particle sensors. Background particle energies and trajectories, and therefore the measurement of particle velocity distributions or the analysis of Langmuir probe measurements, are affected by sheath electric fields associated with satellite charging and potentials. Controlling, or at least monitoring, a satellite potential with respect to background plasma is critical in an optimal interpretation of particle sensor measurements.

Studies have been made over the years to monitor and understand spacecraft charging and potentials in-situ, theoretically, and using computer models capable of self-consistently accounting for the many physical processes responsible for spacecraft charging, with realistic geometries. Early on-orbit measurements of potential associated with charging were made with the Explorer VIII satellite [122, 123]. In space, SCATHA (P78-2) was designed specifically to study satellite charging in the magnetosphere where spacecraft are exposed to energetic particles [124–129]. Surface charging and potentials have also been monitored on the Engineering Test Satellite V of Japan [130]. More recently, the International Space Station has been equipped with the Floating Potential Measurement Unit (FPMU) developed at Utah State University [131]. For spacecraft in the right altitude range, on the dayside of their orbit, photoelectron energy spectra have been used successfully to infer their potential, from electron energy spectra. For spacecraft at altitudes up to 900 km on the dayside of the ionosphere, satellite potentials have been measured from shifts in atomic photoelectron energy peaks [31, 132, 133]. In addition to in-situ experiments, theoretical

models have been applied to explain the principles of surface and spacecraft charging [70, 134]. Theory plays a key role in the interpretation of measurements to determine a satellite’s floating potential. For example, Sanders and Inouye estimate a satellite floating potential by numerically solving the current balance equation for ion, electron, secondary emission and backscattered currents, from which they obtained multiple possible solutions for the floating potential V_f due to the two Maxwellian energy distributions assumed in their analysis and the secondary electron yield [135]. V_f is also determined in other cases where only the currents due to ions and electrons are considered in the current balance equation. This is done by fitting different analytic expressions derived for both the ion and electron current collected by a probe using different theories such as the Orbital Motion Limited (OML) theory and the radial motion limited (RML) theory also called the Allen, Boyd and Reynolds (ABR) theory [115–117]. The OML theory was developed by Mott Smith and Langmuir in 1926 [68, 69]. They assumed that the background plasma is Maxwellian, unmagnetized, and that the radius of the probe is much smaller than the Debye length. The model was later modified by Bernstein, Rabbets and Laframboise by accounting for the sheath formation around the probe in addition to the orbital motion of charged particles and this modified model is referred to as the BRL theory [136–138]. The radial motion limited (RML) theory derived by Allen, Boyd and Reynolds was first applied to spherical probes by considering the radial motion of the charged particle toward the probe, which requires solving Poisson’s equation for the potential in the sheath region around the probe. This theory was later extended to a cylindrical probe by Chen [136, 137, 139]. The analytic formulas derived from each of these theories relate the electron currents and the ion currents to the probe potential, density, temperature among the most important physical parameters. The I-V characteristic of a probe is fitted using the analytic formula for the current collected by the probe and since the floating potential is the potential when the probe is collecting zero current, the fitted equation is interpolated to the point where the current collected is

zero on the I-V characteristic and the potential at this point is the floating potential. Finally, several spacecraft environment computer models have been developed under national sponsorship, including NASCAP and NASCAP-2k developed under contract by NASA and the U.S. Air force, [140, 141], MUSCAT, developed in Cho's team for the Japan Aerospace Exploration Agency [142], and the open source SPIS program [143], developed for the European Space Agency.

In many cases, the focus is on a satellite floating potential; that is, the potential that a satellite has when it collects no net current. However the interest in monitoring a satellite potential is not limited to cases where the satellite is in electrostatic steady state. Such cases occur for example with satellites carrying active instruments such as thrusters or charged particle guns, or in the presence of rapidly varying environmental conditions, as when a satellite crosses the solar terminator. Therefore, considering that most studies on the subject of satellite potentials focus on satellite floating potentials, the satellite potential will be referred to as the "floating potential" in this part of the thesis, and will be written as V_f , with the understanding that the approach presented is more general, and applies to the determination of a satellite potential, whether or not it is collecting zero net current.

The motivation in this part is to go beyond analytic theories that have been used to determine many satellites' potentials and by extension other plasma parameters, by using simulations and multivariate regression techniques. The reason for this is that analytic formulas rely on assumptions and approximations which do not reflect the true conditions encountered in actual measuring conditions. In order to have an improved model, simulations are done for cases that account for more realistic conditions under which measurements are made and, hence, obtain more accurate interpretations of measurements. The range of satellite floating potentials considered extends from -2 to $+2$ V. This is relevant to satellites in low earth orbit (LEO) at low and mid latitudes. Under these conditions, plasma density is sufficiently high, and temperatures sufficiently low (< 0.3 eV) for charging to appear primarily at

surfaces, due to ion and electron impact. Under these conditions, secondary electron and photoelectron emission are of minor importance.

In Sec. 2.2, I describe the computational approach used to create a solution library, consisting of probe currents and associated floating potentials for a broad range of space plasma parameters. A subset of this solution library can in turn be used as a training data set to construct regression models. The remainder subset is then used as a validation data set, to test the inference skill of the models. A methodology to infer a satellite floating potential is presented in Secs. 2.3. While the primary objective is to infer the floating potential, the approach is also extended to construct an inference model for the ratio of the electron density divided by the square root of electron temperature. A summary of the findings and some concluding remarks are finally presented in Sec. 2.5.

2.2 Methodology

Kinetic simulations of the interaction between a small spherical Langmuir probe (SLP) and plasma are done for several ionospheric conditions using PTetra, a three-dimensional kinetic particle-in-cell code, in which electric fields and particle kinetics are calculated self-consistently. In PTetra, the simulation domain is discretized with an unstructured tetrahedral mesh, which makes it possible to represent different spacecraft geometries, on which different boundary conditions can be applied. PTetra has been validated by reproducing known analytic results, and it was benchmarked by comparing results obtained with other, independently developed models [77, 144–146]. This study considers the feasibility of determining a satellite floating potential V_f and the ratio of electron density and square root of electron temperature $n_e/\sqrt{T_eV}$ from currents measured with two identical spherical Langmuir probes of radius 4 mm with fixed bias voltages V_{b1} and V_{b2} , as illustrated in Fig. 2.1. Considering the fact that V_f represents the satellite potential with respect to the background plasma, it

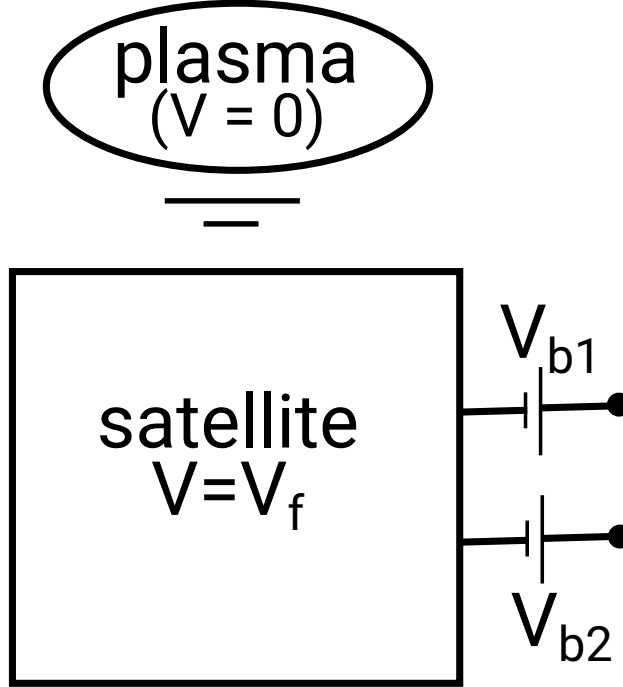


Figure 2.1: Illustration of the two identical probes at fixed bias voltages with respect to the spacecraft.

follows that the probe voltages with respect to background plasma are given by

$$V = V_f + V_b, \quad (2.1)$$

where V_b is the bias voltage of either probe with respect to the spacecraft. The simulations were made with different densities, temperatures, and ion compositions obtained from the International Reference Ionosphere (IRI) model, corresponding to mid latitude ionospheric plasma at different longitudes, latitudes and times, for satellites in low Earth orbit (LEO). The scatter plot in Fig. 2.2 illustrates the extent of the parameter space obtained with the IRI, with 14 squares and 1 circle, showing 15 specific cases for which simulations were made.

The goal here is to assess the feasibility of inferring floating potentials from currents collected with two fixed bias probes and then extend the approach to other plasma parameters. In doing so, the attention is limited to floating potentials ranging from -2 V, to $+2$ V. It should be noted that this approach is not limited to fixed bias

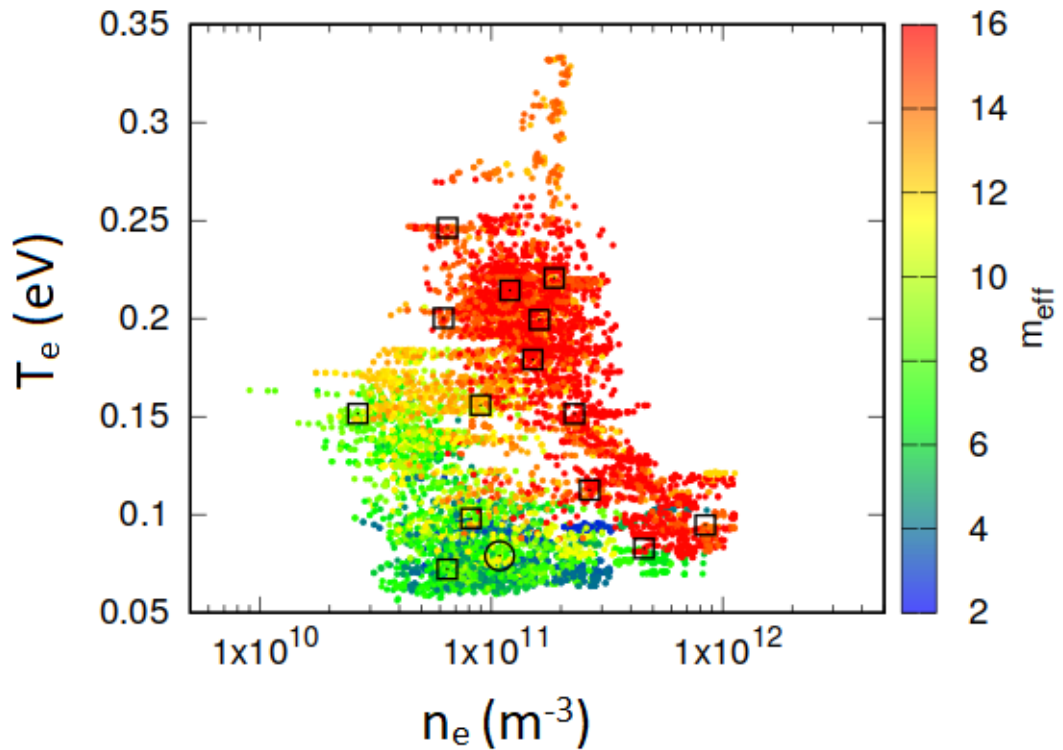


Figure 2.2: Scatter plot of plasma parameters obtained using the International Reference Ionosphere (IRI) model. Parameters selected in the simulations are identified with black rectangles and one circle. The circle identifies the parameters used to produce the profiles illustrated in Fig. 2.3.

probes however, as demonstrated in [147] where the same technique was applied to infer plasma densities and temperatures from characteristics of a sweep voltage probe. In this first assessment of the method, the probes are biased to +2 V and +3 V with respect to the satellite. Owing to Eq. 2.1, simulations are made for probes at voltages ranging from $2 - 2 = 0$ V, to $3 + 2 = 5$ V with respect to the background plasma. In order to develop the approach for arbitrary floating potentials in the specified range, currents are computed for arbitrary probe voltages in the range $[0, 5]$ V with respect to the background plasma. This is done for each of the 15 cases listed in Table 2.1, by carrying out simulations for probes and posts at discrete voltages from 0 to 5 V with increments of one volt.

For this range of voltages, and the plasma parameters considered, the current is found to vary almost linearly with voltage and it is fitted with a maximum relative error of 1.7% using a simple parabola. Given Eq. 2.1, the fit is then used to determine the currents collected by a pair of probes for arbitrary values of the floating potential between -2 and $+2$ V. As an example, Table 2.2 lists probe potentials corresponding to selected floating potentials. Sample simulation results are shown in Fig. 2.3 for cross sections of the average volume charge density, and the ion density at steady state. The parameters used in the simulations in this case correspond to the circle in Fig. 2.2; that is, $n_e = 1.08 \times 10^{11} \text{ m}^{-3}$, $T_e = 0.079 \text{ eV}$, an ion effective mass $m_{eff} = 7.39 \text{ amu}$, and a probe voltage $V = 5 \text{ V}$ with respect to background plasma. In the simulations only the 4-mm-radius probe and an equipotential 1.5-mm-radius guard cylindrical post are taken into account, and no other component of the satellite is accounted for. This is made under the assumption that the probes are supported by a sufficiently long boom on the ram side of the satellite, with the boom and guard aligned along the ram direction. For simplicity, Earth's magnetic field is not included, which is justified by the fact that the sphere radius $a = 4 \text{ mm}$ is small compared to a typical electron thermal gyro-radius $\rho_{eth} = \sqrt{2kT_e/m_e}/\Omega_e$, where $\Omega_e = eB/m_e$ is the electron gyro-radius, k is the Boltzmann constant, T_e and m_e are respectively

Table 2.1: Simulation parameters used in the construction of the solution library.

n	Te	m_{eff}	nO^+	nH^+	nHe^+	nN^+
10^{10} m^{-3}	eV	amu	%	%	%	%
2.6489	0.1516	8.31	93.15	6.06	0.53	0.26
6.2161	0.2003	13.87	94.44	0.95	0.16	4.45
6.4460	0.0722	6.28	86.39	10.2	0.62	2.79
6.4760	0.2464	15.93	99.73	0.00	0.15	0.12
8.1690	0.0981	11.01	96.57	2.95	0.37	0.11
8.9614	0.1559	12.91	95.49	1.53	0.23	2.76
10.859	0.0790	7.39	88.31	7.63	0.50	3.56
12.040	0.2144	15.83	94.73	0.00	0.11	5.16
15.110	0.1791	15.88	95.59	0.00	0.05	4.36
16.120	0.1994	12.83	94.03	1.58	0.17	4.22
18.730	0.2070	12.62	97.87	1.76	0.11	0.27
22.901	0.1515	15.86	95.07	0.00	0.06	4.88
26.629	0.1126	15.88	94.65	0.00	0.00	5.35
45.701	0.0828	15.86	94.65	0.00	0.05	5.30
84.190	0.0947	14.19	94.79	0.78	0.13	4.29

Table 2.2: Sample probe voltages with respect to background plasma, for a spacecraft floating potential ranging from -2 V to $+2$ V, assuming probes with fixed bias voltages of $+3$ V, and $+2$ V.

$V_f(\text{V})$	$V_1(\text{V})$	$V_2(\text{V})$
-2	1	0
-1	2	1
0	3	2
1	4	3
2	5	4

the electron temperature and mass, and B is the geomagnetic field at the satellite location. Indeed among all the cases considered in Fig. 2.2, and assuming $B \sim 30 \mu\text{T}$ at mid-latitudes, the smallest value of ρ_{eth} is approximately a factor 9 times larger than the probe radius. In the simulations, cases with multiple species are considered, with both electrons and ions being described by Maxwellian distribution functions at rest in the reference frame co-rotating with Earth. Thus, in the satellite (and probe) reference frame, plasma is drifting from the ram direction at approximately the orbital speed, assumed to be $v_{orb} = 7500 \text{ m/s}$. The distribution of current collected

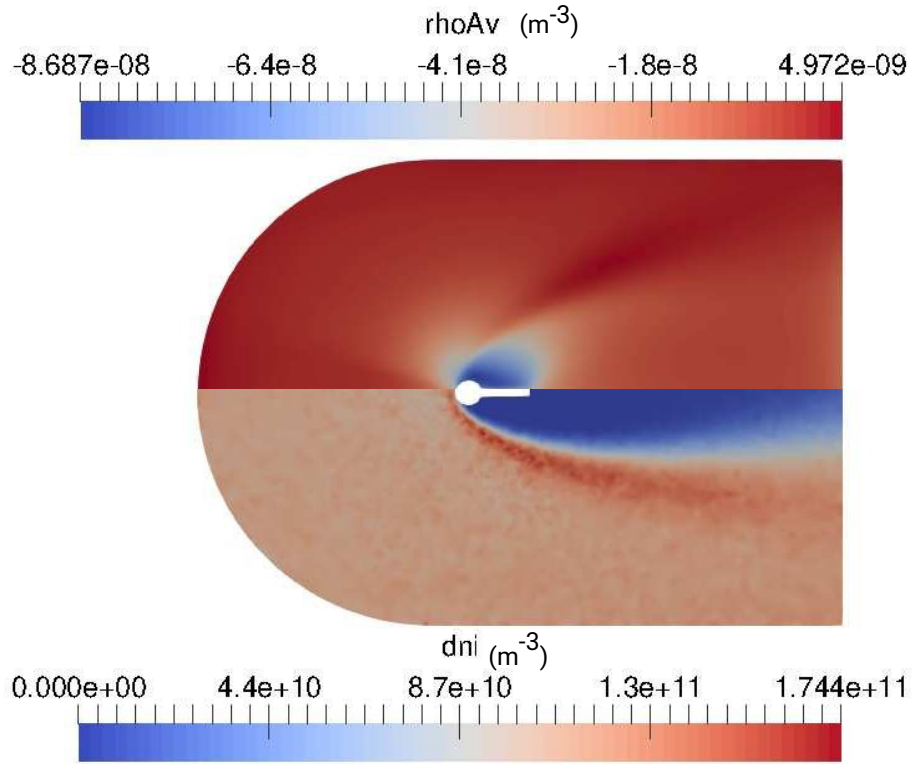


Figure 2.3: Cross section of the charge density profile ‘rhoAv’ in the upper half and ion density ‘dni’ in the lower half. Charge density and ion density are in SI units. The parameters used in the simulation correspond to the circle in Fig. 2.2

per surface area on the probe and supporting post is shown in Fig. 2.4, corresponding to the same case as in Fig. 2.3. With a positive voltage, the probe repels incoming ions, thus creating a wake downstream, and both structures collect negative current, as seen in the figure.

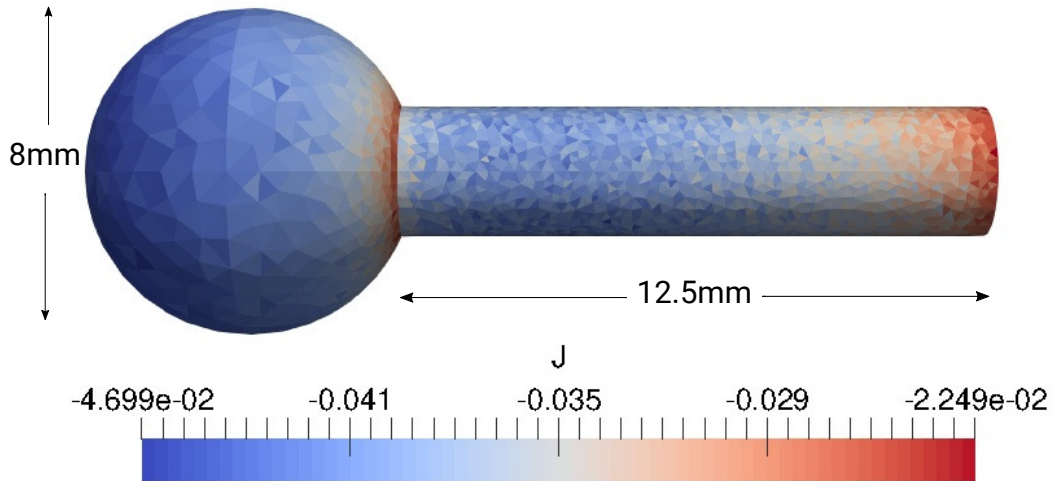


Figure 2.4: Current per surface area (A/m^2) collected by the probe and the equipotential supporting guard cylinder. The plasma parameters and voltage used in the simulation are the same as in Fig. 2.3.

Three dimensional kinetic simulation results are used to build a solution library \mathcal{L} , in which each data entry, or node in this multivariate space, contains currents collected by the two probes for randomly distributed floating potentials in the range $[-2, 2]$ V, followed by the floating potential, the electron density, the temperature, the calculated value of the electron density divided by square root of temperature and the effective mass, for each of the 15 cases in Table. 2.1. Sixteen randomly distributed floating potentials are considered for each of the 15 cases. This solution library, in turn, is used to construct disjoint training and validation sets from which models are trained and validated, respectively.

2.3 Construction of Inference Models

The approach adopted here to construct inference models makes use of a combination of theory and multivariate regression; that is, the interpolations of dependent variables in a multi-dimensional space of independent variables. The goal is to infer satellite

floating voltages V_f and the ratio of density to the square root of electron temperature given a two-dimensional vector (i_1, i_2) of currents collected by two fixed bias voltage probes attached to a satellite. An approximate analytic expression for the floating potential and the ratio $n_e/\sqrt{T_{eV}}$ based on the Orbital Motion Limited (OML) theory is first derived. A regression algorithm is then applied and assessed to perform the same task, followed by a combination of the two methods using boosting ensemble learning approach, in which multivariate regression is used to reduce the error in the analytically inferred values. These approaches and sample applications are presented in what follows.

2.3.1 Analytic model

The interpretation of currents collected by spherical Langmuir probes is commonly based on Mott-Smith and Langmuir’s OML theory [68, 69]. This theory has since been further refined and extended by many authors [136, 148], and continues to be used to diagnose many laboratory and space plasma experiments [149]. This success is due to the relatively simple analytic expressions that it produces in different asymptotic limits, which can be used to quickly infer plasma parameters from probe characteristics; that is, from collected currents as a function of applied voltage. OML is based on a number of assumptions as discussed in Section 1.5. A common assumption made for electrons is also that particles have zero mean velocity. This is justified by the fact that electrons with temperature $T_e = 0.1$ eV in the low Earth orbit have a thermal speed of the order 10^5 m/s which is much larger than the plasma drift velocity or the satellite ram speed. Under these conditions, OML predicts the following expression for the electron current collected by a spherical probe biased positively with respect to the background plasma:

$$I = -ner^2 \sqrt{\frac{8\pi kT_e}{m_e}} \left(1 + \frac{e(V_f + V_b)}{kT_e} \right), \quad (2.2)$$

where n is the electron density, and $V_b + V_f$ is the probe voltage with respect to background plasma. Using Eq. 2.2 as the first estimate, the currents I_1 and I_2 collected by two probes biased to voltages V_{b1} and V_{b2} are written as:

$$I_1 = -ner^2 \sqrt{\frac{8\pi kT_e}{m_e}} \left(\frac{e}{kT_e} \right) \left(V_f + \frac{kT_e}{e} + V_{b1} \right) \quad (2.3)$$

and

$$I_2 = -ner^2 \sqrt{\frac{8\pi kT_e}{m_e}} \left(\frac{e}{kT_e} \right) \left(V_f + \frac{kT_e}{e} + V_{b2} \right), \quad (2.4)$$

where $kT_e/e = T_{eV}$ is the electron temperature in units of electron-volts. Given the known values of the bias voltages, and the measured currents, it is a straightforward exercise to solve for $V_f + T_{eV}$ and obtain

$$V_f + T_{eV} = \frac{V_{b1}I_2 - V_{b2}I_1}{I_1 - I_2}. \quad (2.5)$$

which expresses the satellite potential and the unknown temperature in terms of known bias voltages and measured collected currents. Assuming for simplicity that T_{eV} , the temperature in units of eV, is small compared with the satellite potential, then the following approximation

$$V_f \simeq \frac{V_{b1}I_2 - V_{b2}I_1}{I_1 - I_2} \quad (2.6)$$

is obtained for the satellite potential. Also, if Eq. 2.5 is substituted in either Eq. 2.3 or 2.4, it gives

$$\frac{n}{\sqrt{T_{eV}}} = \frac{1}{er^2} \sqrt{\frac{m_e}{8\pi e}} \left(\frac{I_1 - I_2}{V_{b2} - V_{b1}} \right), \quad (2.7)$$

which expresses $n_e/\sqrt{T_{eV}}$ in terms of known physical quantities.

Equations 2.6 and 2.7 are used to first infer the floating potential and the ratio $n_e/\sqrt{T_{eV}}$ by direct substitution of the measured currents and known bias voltages in the two equations. The result obtained for the floating potential is shown in Fig. 2.5, where inferred potentials are plotted as a function of actual potentials in the library. The analytic approximation in Eq. 2.6 is seen to overestimate the satellite potential in all cases considered. This systematic discrepancy is due in part to the neglect of

T_{eV} in Eq. 2.5 since, from that equation, it is clear that the approximate expression for V_f in Eq. 2.6 should give satellite potential plus the electron temperature in units of electron-volts. This is not the only cause for the discrepancy because, if it were, the discrepancy between inferred and actual potentials would be approximately constant in the full range of potentials considered. Part of the difference might come from the neglect of the ion contribution to the collected current, but the larger overestimate at larger floating potentials suggests otherwise. Indeed, with a bulk kinetic energy of approximately 4.7 eV, oxygen ions can reach the probes for all floating potentials considered. When collected, positive ions contribute positive currents, thus reducing the magnitude of the negative currents from electrons. This reduction, however, is most important for the lower floating potentials (~ -2 V), and least important for the larger positive voltages, since the potential barrier is then the highest. Ion current collection should, therefore, lead to a larger discrepancy in Fig. 2.5 at lower values of V_f , which is not seen in the figure. Another cause of the discrepancy could be the presence of the post holding the spherical probe and the formation of a wake as shown in Fig. 2.3, which is not accounted for in the OML theory. Indeed, Fig. 2.4 shows that current is not collected uniformly around the probe as for an isolated sphere in an assumed non-drifting surrounding plasma in OML. This, combined with the supersonic ion drift and the resulting wake, are likely causes for the differences between inference and actual values of V_f in Fig. 2.5. Nonetheless, the analytically inferred floating potentials are in close proximity to actual values, both qualitatively, and quantitatively. Inferred V_f values are tightly distributed along a line that nearly parallels the solid line in Fig. 2.5 for an ideal correlation. The small scatter in the inferences is due to the different plasma conditions, corresponding to different densities, temperatures, and ion effective masses, accounted for in the solution library. Fig. 2.6 compares values obtained when equation 2.7 is used to infer the $n_e/\sqrt{T_{eV}}$, and actual values from the database. While the general trend of analytically inferred values agrees with actual data, analytically inferred values are systematically lower.

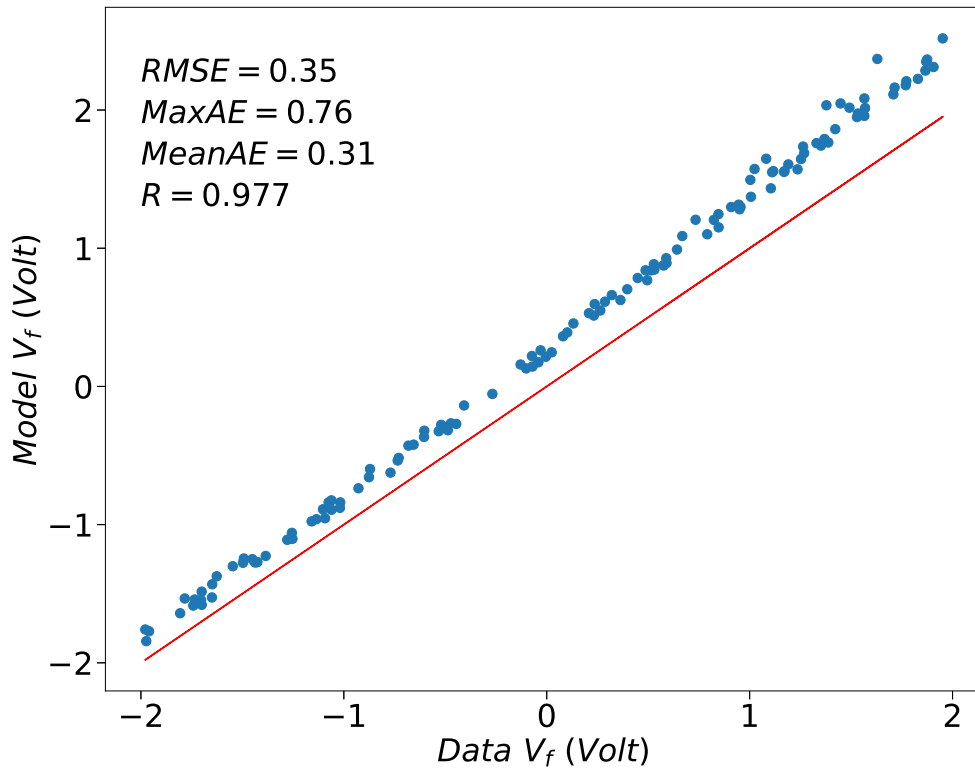


Figure 2.5: Comparison between the satellite floating potential approximated with Eq. 2.6 and actual value in the synthetic data. The line corresponds to a perfect agreement between the two floating potentials

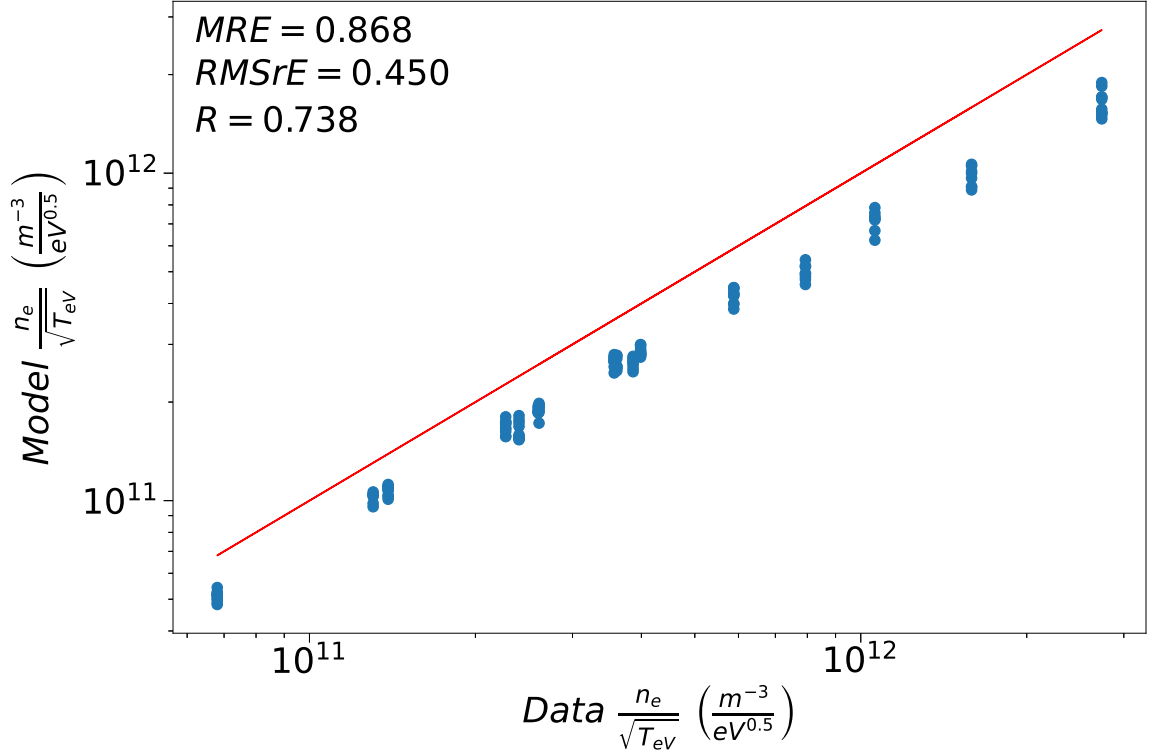


Figure 2.6: Comparison between $\frac{n_e}{\sqrt{T_{eV}}}$ obtained with Eq. 2.7 and actual value in the synthetic data, with the line corresponding to a perfect agreement. The maximum relative error (MRE), root mean square relative error (RMSrE) and correlation coefficient (R) are used as model skill metrics.

This observation is in contrast to what is observed when Eq. 2.6 is used for the floating potential in which the inferred values are higher than the actual value. The main cause of this discrepancy in the inferences made with Eq. 2.7 is likely due to post holding the probe, which reduces its collection area. This in turn reduces the probe's effective radius which, referring to Eq. 2.7 should lead to higher values of $n_e/\sqrt{T_{eV}}$ than the estimates (dots in the figure) made with the full $r = 4$ mm radius.

2.3.2 Regression with Radial Basis Function (RBF)

As mentioned in Section 1.7, several approaches have been developed to do multi-variate regression. For example, kriging was pioneered by Krige for geological survey

applications [150], and further developed on formal mathematical grounds [151–153]. Deep learning neural networks also offer a powerful means for constructing predictive regression models for large sets of data with complex interconnections between input and output [154, 155]. The regression approach used here is based on radial basis functions [156, 157]. In the following, RBF is used to directly infer a satellite floating potential and the ratio of electron density and square root of electron temperature from a pair of fixed bias probes.

This method is similar to kriging, in that it performs interpolations of dependent variables at locations in a multi-dimensional space, from their “distance” from selected reference points or “centers”. The advantage of RBF compared with neural networks or kriging, is its simplicity and the fact that, in many cases, it requires relatively few centers in order to provide accurate models. This is in contrast with neural networks, which require large data sets for training a model, as well as large sets for validation. This difference in the number of data entries or nodes required for training and validating is critical when constructing an inference model based on computed (or synthetic) data, because of the large computational resources often needed in order to carry out simulations.

In this application of the RBF approach, independent variables are therefore two dimensional vectors (i_1, i_2) , and dependent variables are scalars (one dimensional vectors) V_f or $n_e/\sqrt{T_{eV}}$. For more generality, however, assume that the independent and dependent variables are n-tuples X and Y , respectively. These n-tuples can be of arbitrary dimensions, and these dimensions need not be the same. Given a set of N centers consisting of vectors X_i and Y_i , $i = 1, N$, the method consists of approximating dependent variables for an arbitrary X within a given domain, as

$$Y \simeq \sum_{j=1}^N a_j G(|X - X_j|), \quad (2.8)$$

where the X_j are selected reference nodes, or centers, and G is a suitable regression or interpolation function. The argument of G is a scalar given by the “radial distance”

between X and the centers X_i . There is no constraint in the metric used to define this radial distance, but a common choice is the L^2 norm, or Euclidean distance. The accuracy of the model in a given data set depends on the number and location of the centers, as well as on the interpolation function G . Centers can be selected among nodes in the solution library, or they can be defined independently. For a library constructed from kinetic simulations requiring large computational resources, however, a practical choice is to select them from nodes in the library. Different strategies have been proposed for determining the selection of centers from a set of nodes. Here, a straightforward approach consisting of trying every possible combination of N centers among the \mathcal{N} nodes in a given training data set is used, for a total number of combinations

$$N_c = \binom{\mathcal{N}}{N} = \frac{\mathcal{N}!}{N!(\mathcal{N} - N)!}. \quad (2.9)$$

For large values of \mathcal{N} , this number increases very rapidly with N , and it may be necessary to restrict training to a small subset of randomly selected nodes in \mathcal{L} . In this study, a training set is made from 90 randomly selected nodes among the 240 nodes in the solution library. This then offers the possibility of validating the model with the remaining 150 nodes. The combination of centers selected for the construction of the model is the one that produces the highest inference skill over the full training set, as measured with a cost function. Different types of cost functions can be used as a measure of the discrepancy between inferred and data, provided that they be positive definite, and that they increase as inferred values deviate from data values. Examples include the mean square deviation, the maximum relative error, and the maximum absolute error. The next question concerns the determination of the regression coefficients a_j . In what follows, these are determined by requiring exact collocation at centers; that is,

$$Y_i = \sum_{j=1}^N a_j G(|X_i - X_j|), \quad i = 1, 2, \dots, N, \quad (2.10)$$

which can be written in matrix form as

$$\begin{pmatrix} A_{11} & A_{12} & \cdots & A_{1N} \\ A_{21} & A_{22} & \cdots & A_{2N} \\ \vdots & \vdots & \ddots & \vdots \\ A_{N1} & A_{N2} & \cdots & A_{NN} \end{pmatrix} \begin{pmatrix} a_1 \\ a_2 \\ \vdots \\ a_N \end{pmatrix} = \begin{pmatrix} Y_1 \\ Y_2 \\ \vdots \\ Y_N \end{pmatrix}, \quad (2.11)$$

where A_{ij} are matrix elements defined as

$$A_{ij} = G(|X_i - X_j|) \quad (2.12)$$

and a_j are regression or fitting coefficients. If dependent variables are scalars, then the regression coefficients a_i are also scalars; otherwise, they are vectors with the same dimension as the Y vectors. More generally, collocation can be relaxed at the centers in order to improve a model skill (reduce the cost function) by introducing “smoothing” or the “nugget” effect as in geostatistics [158]. This can be achieved by adding non-zero elements to the diagonal elements of matrix A in Eq. 2.11, or to each component of the center Y_i dependent vectors, and minimizing the cost function with respect to these values. In this work, smoothing was not applied, as it was found to lead to minimal improvement in the model inference skill. Smoothing should be considered, however, when model training is made on data with statistical noise.

Floating potential inferences

The procedure described above is now applied to infer floating potentials from a 2-tuple of currents (i_1, i_2) measured by the probes. The number of centers N used in training this model is important, as the accuracy of the model inference generally increases with increasing values of N . However, too large a value of N can lead to over-fitting. While the model skill may improve with larger values of N , when applied to the training data set, it can deteriorate on the validation set. The cost function used in constructing the model is the MaxAE defined in equation 1.17. The model uses six centers, which is the combination that minimizes the MaxAE when inferring

the floating potential for the 90 entries in the training set. The validation data set consisted of the remaining 150 nodes. Several interpolating functions were used for training, and the one found to give the best results is

$$G(x) = 0.5x^\lambda \ln x, \quad (2.13)$$

where x is the Euclidean distance, or $L2$ -norm of the difference between two current vectors, defined as $\sqrt{(I - I_j) \cdot (I - I_j)}$ and $\lambda = 1.6$. The trained model was then applied to the validation set in order to assess its skill. A comparison between inferred potentials with known potentials from the validation set is shown in Fig. 2.7. The distribution of points in this plot is clearly different from the one in Fig. 2.5. While the maximum error is comparable (1 V vs. 0.8 V) the distribution around the solid line, corresponding to a perfect agreement, shows more scatter than in Fig. 2.5 where points are more tightly aligned above the solid line.

Density divided by square root of temperature

An inference model is also constructed for $n_e/\sqrt{T_{eV}}$ using RBF. The model makes use of the same interpolating function as the one used for the floating potential model. However, the cost function used in training the model is the maximum relative error MRE (in absolute value) due to the fact that this ratio varies over more than one order of magnitude. This choice is preferred to the maximum absolute error because training the model by minimising the maximum absolute error would lead to inferences with excellent skill when applied to larger values of inferred values of $n_e/\sqrt{T_{eV}}$, but large relative errors for smaller values. With MRE, the absolute difference is normalized by dividing by the inferred $n_e/\sqrt{T_{eV}}$ as in equation 1.19. Figure 2.8 shows a correlation plot of RBF inferences of $n_e/\sqrt{T_{eV}}$ with values used in the simulations contained in the validation set when applied to the model trained with 6 centers. This approach shows an improvement to the inferences made when using Eq. 2.7 with a reduction in the maximum relative error from 87% to 33%. The points in Fig. 2.8 are distributed

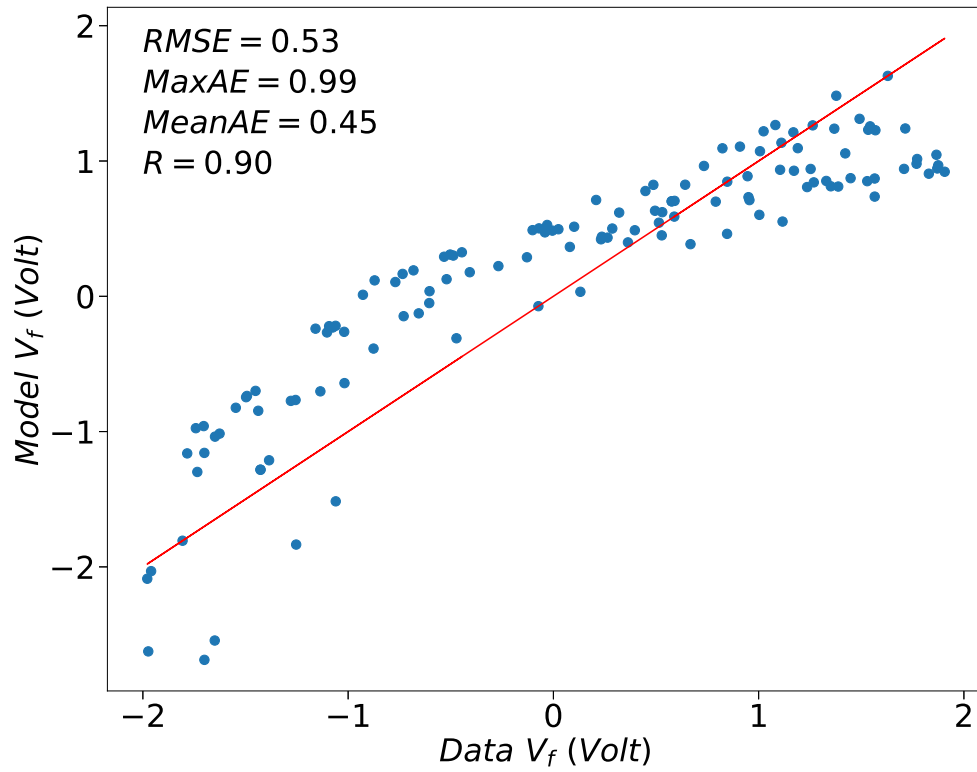


Figure 2.7: Comparison between floating potentials inferred with RBF using six centers and actual value in the synthetic data. The line corresponds to a perfect agreement between the two floating potentials

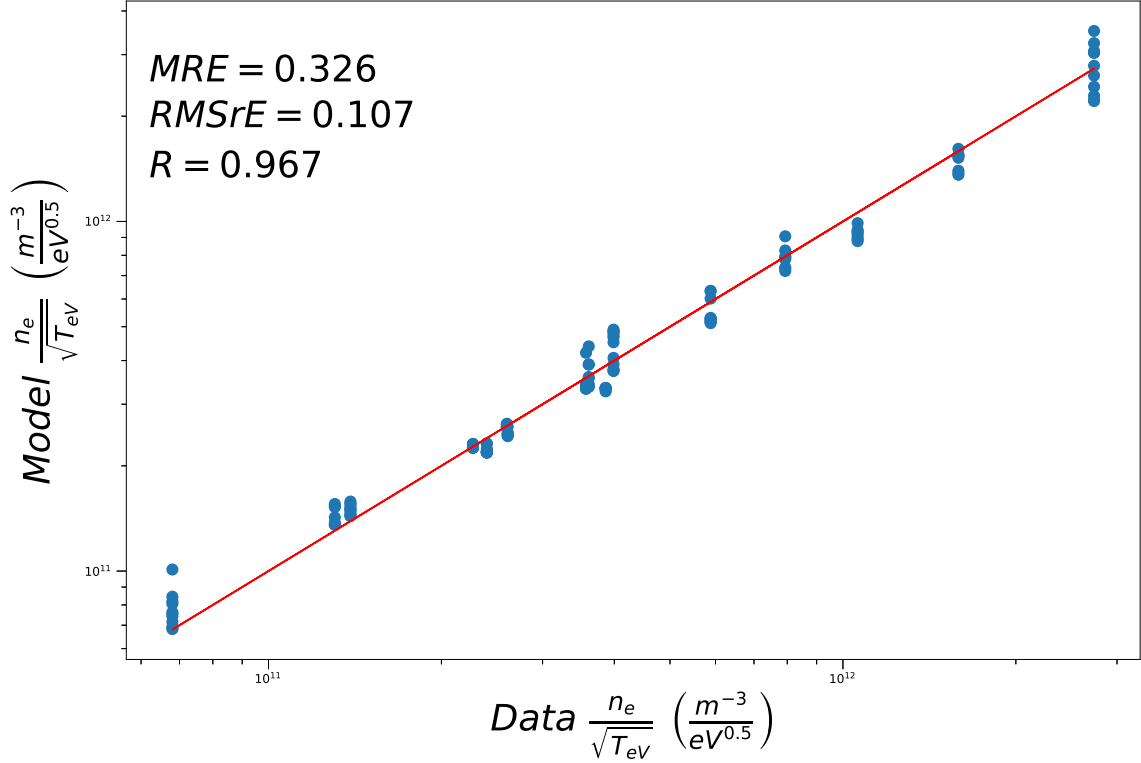


Figure 2.8: Comparison between $\frac{n_e}{\sqrt{T_{eV}}}$ inferred with RBF using six centers, and actual data in the validation set. The line corresponds to a perfect agreement.

on either side of the solid line, which is in contrast to Fig. 2.6 where all the points fall below the solid line.

2.3.3 Combination of Orbital Motion Limited (OML) Approximation and Radial Basis Function (RBF)

The regularity in the difference between OML-inferred and actual potential shown in Fig. 2.5, and that of $n_e/\sqrt{T_{eV}}$ in Fig. 2.6 suggests that it should be possible to use regression to correct for this difference and construct an improved combined model for both parameters. This is done by first using Eq. 2.6 and 2.7 to estimate the parameters, and then using RBF to model and correct the error between data values and the analytic estimates. The improved models resulting from these combinations

are written as

$$V_f^{model} = \frac{V_{b1}I_2 - V_{b2}I_1}{I_1 - I_2} + \sum_{j=1}^N a_j G(|I - I_j|), \text{ and} \quad (2.14)$$

$$\frac{n}{\sqrt{T_{eV}}} = \frac{1}{er^2} \sqrt{\frac{m_e}{8\pi e}} \left(\frac{I_1 - I_2}{V_{b2} - V_{b1}} \right) + \sum_{j=1}^N a_j G(|I - I_j|). \quad (2.15)$$

The results obtained when this boosting ensemble approach described in Section 1.7 is used to train inference models for both the floating potential and the ratio $n_e/\sqrt{T_{eV}}$ as presented below.

Floating potential

Following the same procedure as in Section 2.3.2, the model is first constructed using a training data set consisting of 90 randomly selected nodes in the solution library, and it is validated using the remaining 150 nodes. In doing so, training is done assuming different numbers of centers, and here also, increasing N generally leads to better inferences in the training set, but for validation, the model skill deteriorates when N exceeds a certain value. In this case, training with four centers, the maximum absolute error (MAE) is 0.15 V on the training set, but 0.2 V on the validation set. With six centers, however, the MAE in training is 0.13 V, and 0.18 V in validation which correspond to errors of 3.3% and 4.5% relative to the range of floating potentials considered. Larger numbers of centers result in larger errors in validation, so in this case, the optimal number of centers used is $N = 6$. The excellent correlation between inferred and actual voltages is shown in Fig. 2.9a for which a correlation $R = 0.998$ and a root-mean-square difference of 0.07 V are calculated. The combination of Eq. 2.6 derived from OML theory and RBF, therefore, leads to a significantly improved inference model.

As a final exercise, the robustness of the model to noise in the collected currents is assessed. This is done by applying the same trained model constructed from the training data set with no noise to sets obtained by adding increasing levels of normal

Table 2.3: Different measures of the combined model inference skill when applied to the validation data sets, with different levels of noise.

σ	MAE	RMSE	Correlation
0.0	0.18	0.07	0.9983
2×10^{-3}	0.18	0.07	0.9980
5×10^{-3}	0.31	0.10	0.9959
1×10^{-2}	0.43	0.15	0.9919
2×10^{-2}	0.85	0.28	0.9728

distributed noise to all currents in the validation set. To be specific, noise is added to each current in the validation set using

$$I_n = I + \sigma r I, \quad (2.16)$$

where I is the data (simulated) current without noise, σ is a specified relative noise standard deviation, and r is a zero-mean random number with normal (Gaussian) distribution. The results in Table 2.3 show a steady degradation in the inference model skill as noise increases, as expected. With $\sigma = 0.2\%$, the effect is negligible, but for larger values, the maximum absolute errors increase steadily, and the loss of inference skill is clearly visible in Fig. 2.9d. With $\sigma = 2\%$, the maximum absolute error in the inferences is about 0.85, and the RMS error is 0.28 V. Interestingly, while deviations from a perfect agreement increase as noise increases, the points remain distributed along the solid line, with apparently equal probability for over- and underestimates.

Density divided by square root of temperature

Using the same procedure as for the floating potential, equation 2.15 is now applied to infer the ratio $n_e/\sqrt{T_{eV}}$. The RBF model is constructed using four centers for optimal validation skill. The correlation plot in Fig. 2.10 for resulting model inferences shows

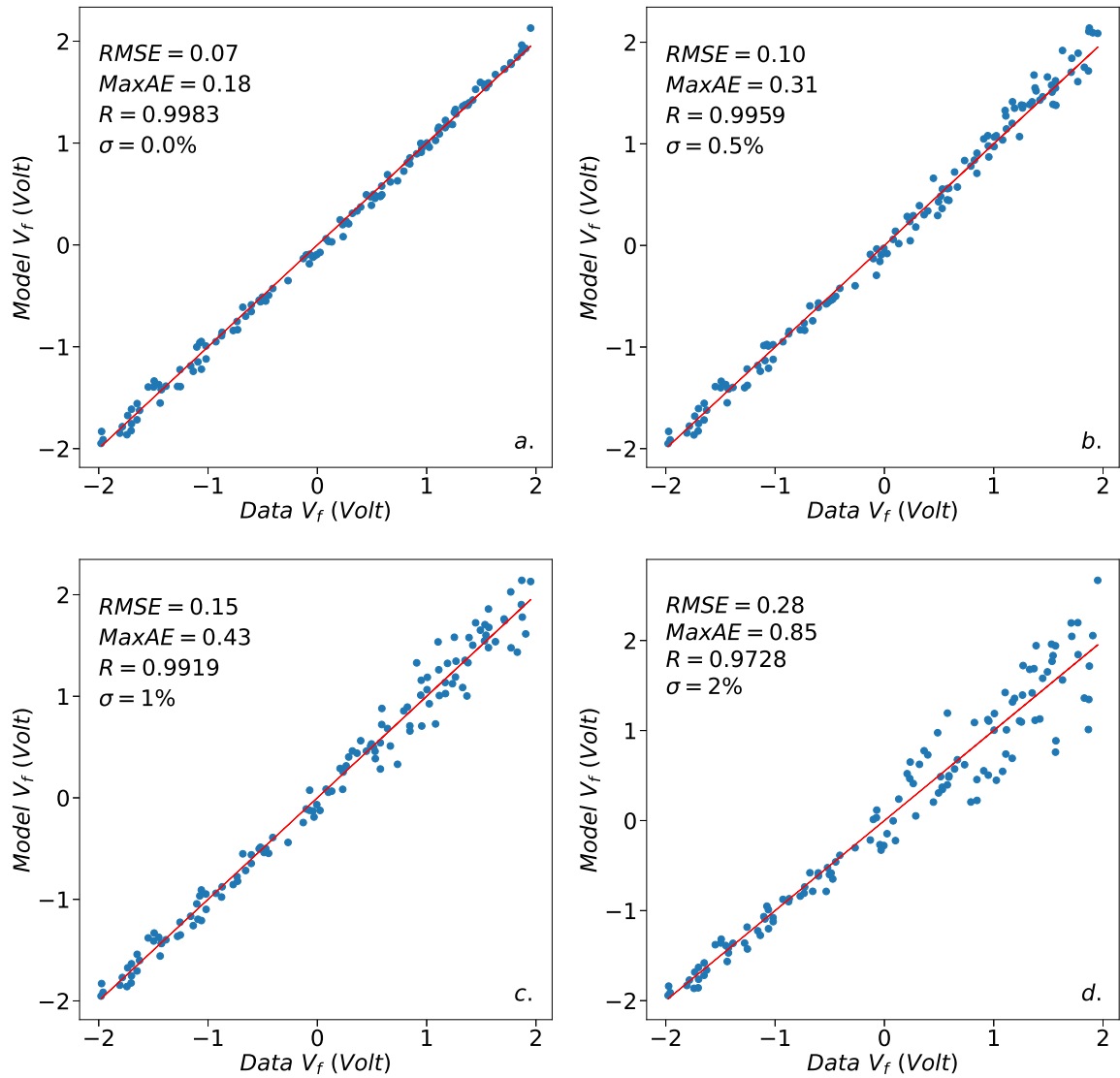


Figure 2.9: Comparison between satellite floating potentials obtained from a combination of Eq. 2.6, and RBF with six centers, and potential values in the validation data set. The line corresponds to a perfect agreement between the two floating potentials. In panel *a*, no noise is added to currents in the validation set, while in *b*, *c*, and *d*, noise with a relative standard deviation $\sigma = 0.005$, $\sigma = 0.01$, and $\sigma = 0.02$ is added respectively.

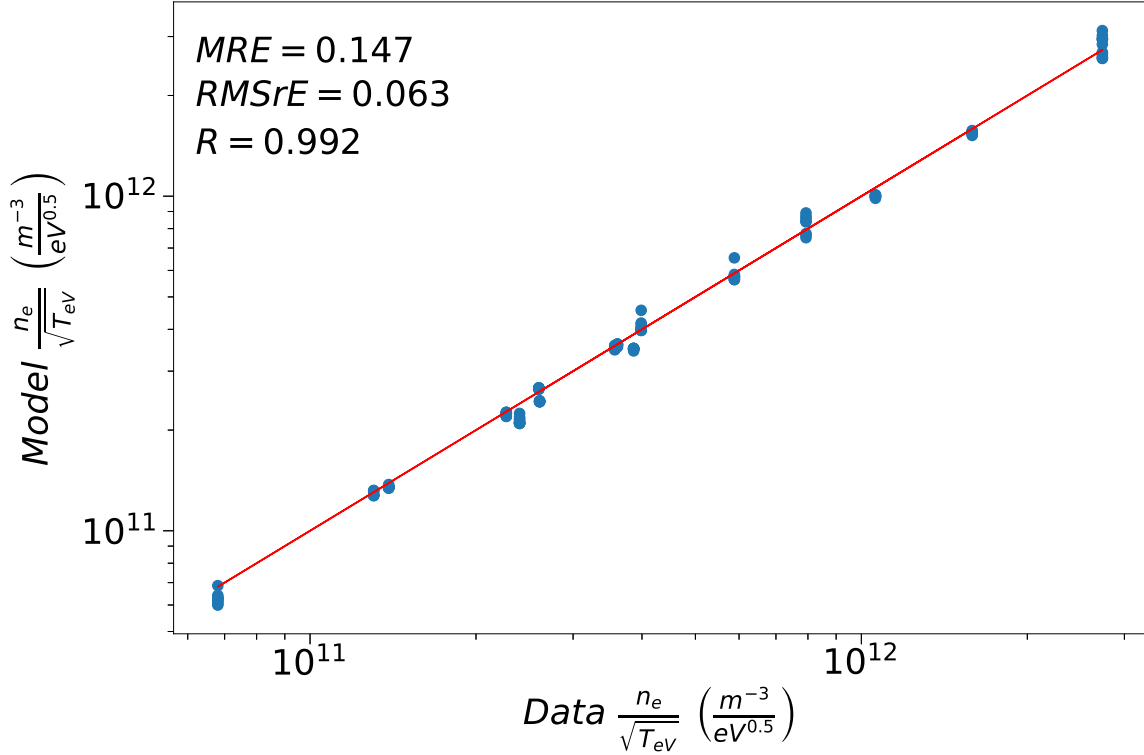


Figure 2.10: Comparison between $\frac{n_e}{\sqrt{T_{eV}}}$ inferred with combined OML and RBF using four centers, against data in the validation set. The line corresponds to a perfect agreement.

a significant improvement in the model skill compared to those when only OML or RBF are used. The points align very closely to the line indicating excellent model inference, and the vertical spread in the distribution of points are very small compared to the ones in Fig. 2.6 and Fig.2.8. This model produces a MRE of 15%, a root mean square relative error (RMSrE) of 6%, and a Pearson correlation $R = 0.992$ when the skill of the model is assessed using the validation data set.

2.4 Possible experimental verification

While beyond the scope of this study, ways by which the proposed technique could be verified experimentally are of interest, and are briefly discussed here for a spacecraft potential. One obvious approach would be to compare floating potentials of a rocket

or a spacecraft inferred with this technique, with those obtained from an independent measurement. A possibility would be to use an electron spectrometer to measure the energy of known peaks resulting from upper atmospheric photoelectron emission, as described by Goembel, et al. [31, 159]. Another approach could consist of equipping a rocket or satellite with two double-probe units as illustrated in Fig. 2.11. Each unit would support a double-probe sensor with fixed bias voltages of say, +2 and +3 V with respect to their respective units. The two units would be biased to different and variable voltages, V_1 and V_2 , with respect to the spacecraft bus which would be at potential V_f with respect to the background plasma. The technique presented above would then be used to infer the potentials \tilde{V}_1 and \tilde{V}_2 of units 1 and 2, with respect to the background plasma. According to the analysis presented above, \tilde{V}_1 and \tilde{V}_2 should approximate $V_f + V_1$ and $V_f + V_2$ respectively. Thus, the difference $(\tilde{V}_1 - \tilde{V}_2) - (V_1 - V_2)$, which should ideally be zero, would provide a straightforward validation of the method used in this work. The possibility exists of course, for inferences of V_f made with this approach to be in error by a systematic and constant voltage, independent of the floating potential. While possible, this appears to be unlikely, and should it be the case, the method could be recalibrated, for example, using the method described above to correct for such a constant error. Since this second validation method is independent of the actual potential of a satellite, it could be carried out in space, as well as in a lab experiment, in which space plasma conditions could be suitably reproduced [160, 161]. Also noteworthy, this validation technique is not limited to the double-probe unit considered here. It could also be applied by replacing either one or both units with any two instruments capable of measuring a satellite potential.

2.5 Summary and Conclusions

Three approaches are presented to determine the satellite floating potential and the ratio between the electron density and the square root of the temperature from cur-

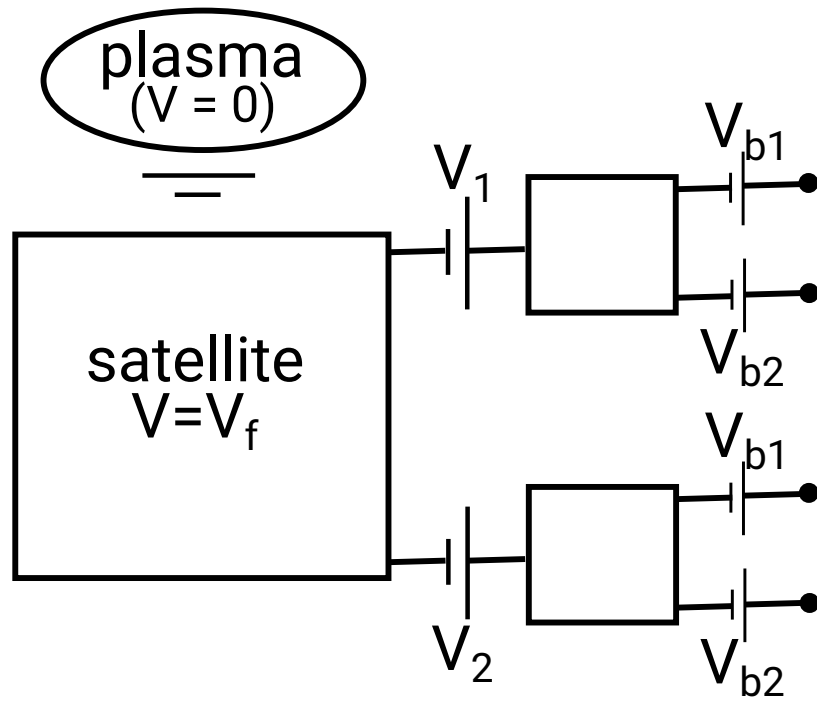


Figure 2.11: Illustration of a two double-probe units at fixed bias voltages with respect to their units, which are biased to different voltages, V_1 and V_2 , with respect to the spacecraft.

rents collected with a pair of fixed-bias Langmuir probes. This relatively simple sensor would provide measurements with higher temporal and spatial resolution than possible with swept-voltage Langmuir probes. This ability to monitor rapid responses in a spacecraft floating potential would be useful in active experiments where short ($\lesssim 1$ ms) intense beams of charged particles are emitted periodically [162–164], or in the presence of high frequency waves. All approaches are assessed using a solution library in which currents collected by the two probes are obtained from kinetic simulations, assuming different plasma environment parameters and satellite potentials with respect to the background plasma. The first approach is based on simple analytic expressions, derived in the Orbital Motion Limited (OML) approximation. While the results obtained with this approximation systematically overestimate the potential and underestimate the value of $n_e/\sqrt{T_{eV}}$, they both produce very regular inferences that tightly parallel actual values. In the second approach, inference models are constructed, based exclusively on RBF regression. The comparison between inferred and actual potentials shows less regularity and more scatter than with the analytic approach, but the model skill, measured as the MaxAE, is comparable in magnitude with that found with the OML analytic model. When applied to $n_e/\sqrt{T_{eV}}$ however, the RBF model performs better than the analytic model with an improved MRE of 32.6% compare to 86.8% obtained using OML analytic model. The third approach is a combination of the first two, with RBF being used to correct the differences between OML inferred values, and actual values in the training set. The floating potential model using this approach is found to have the highest inference skill, with a MaxAE of 0.18 V and a relative error of 4.5% when applied to a validation set without noise. The tolerance of this model to statistical noise is assessed by adding normal noise to currents with different standard deviations σ in the validation set. As expected, the model skill decreases with noise, whether measured in terms of the maximum inference error, the root mean square deviation, or the correlation coefficient R . The acceptable uncertainty in the inference of course depends on the application, and on

the parameters being considered. Assuming that an upper acceptable limit to the skill degradation corresponds to doubling the MaxAE in a noiseless validation set, it is found that the noise level that would be tolerable in the range of parameters considered, would be reached with a value of σ between 0.5 and 1.0%. Similarly, the best technique to infer the ratio $n_e/\sqrt{T_{eV}}$ is obtained by combining the analytic expression in equation 2.7 with RBF regression, in which RBF is used to correct the offset in the analytic inferences. While the ratio $n_e/\sqrt{T_{eV}}$ is generally not a physical parameter of prime interest, it can be a useful constraint to check the consistency of independently measured densities and temperatures or to estimate one of these parameters when the other can be measured accurately. Two possible approaches have also been described, for validating the proposed approach applied to infer the floating potential experimentally.

Several assumptions are made in this analysis. In particular, background electrons are assumed to be unmagnetized, with a drifting Maxwellian distribution function, secondary electron, and photoelectron emission are neglected. These assumptions are justified in mid-latitude ionospheric plasma encountered by satellites along nightside low Earth orbits (LEO) where collisions with neutrals are sufficiently frequent for electrons to be approximately Maxwellian. The neglect of the Earth's magnetic field is justified by the fact that a typical electron thermal gyro-radius ($\gtrsim 3.5$ cm) is larger than the probe radius considered ($r = 4$ mm). Finally, the analysis in this work is based on a solution library constructed with kinetic simulations assuming a greatly simplified geometry consisting of a single spherical probe attached to a guard post at the same potential. In this geometry, the presence of the satellite bus and other payloads is not accounted for. This implies that the probes and guards would be held at the ends of sufficiently long booms extending in the ram direction (the direction in which the satellite is traveling). Even under such idealized conditions, one could expect effects caused by the proximity to the satellite, owing to the presence of geomagnetic fields, and the fact that electrons gyrate around and travel along

magnetic field tubes. Perturbations in collected currents could occur when magnetic field lines passing through the probes also intersect other satellite components, the electric sheath around the satellite, or the wake region. Those considerations are mentioned here with the caveat that they would depend on the specifics of a given mission and should be included in the creation of a model in support of a mission, prior to deployment in space. In this study, the range of satellite potentials considered has been limited to $[-2, 2]$ V, which is deemed relevant to LEO orbits. The approach, however, is not limited to this range, as it could readily be adapted to cover a wider range of satellite potentials.

Chapter 3

Swarm Spherical Langmuir Probes

This chapter is based on a manuscript titled “Inference of fixed bias probe measurements - A machine learning approach” submitted for publication in the Journal of Geophysical Research (JGR) by Akinola Olowookere, Richard Marchand, and Stephan Buchert. In this chapter, both kinetic simulation and regression techniques are used to interpret Langmuir probe measurements by considering a truncated simplified Swarm satellite geometry, in which the two probes are biased to a fixed potential.

3.1 Introduction

The importance of Langmuir probes in the study of both space and laboratory plasma cannot be overstated. This instrument is used routinely in lab and space experiments to infer plasma densities, temperature, and plasma potential from measured currents as a function of bias voltage. However, despite a century of experimentation, theory, and more recently computation, accurate inferences of parameters such as plasma density, temperature, and spacecraft potential, with quantified uncertainties using this relatively simple instrument remain elusive. Most approaches used in the interpretation of probe’s measurements rely on analytic expressions obtained theoretically for probe characteristics; that is, currents collected as a function of bias voltages. A common framework used in interpreting probe measurements is the orbital motion limited (OML) theory which was developed a century ago by Mott Smith and Lang-

muir[68, 69, 149]. Many authors have contributed improvements to this theory, so as to account for conditions not considered in OML [115, 116, 165]. Lam proposed a theory [166] to solve the Langmuir problem in a quiescent, collisionless plasma in the limit where the probe dimension is large compared to the Debye length, in contrast with the limit considered in OML which assumes a small probe radius compared to the Debye length. These theories were validated numerically by Chen [167] on the assumption of zero ion temperature made in the Allen, Boyd, and Reynolds (ABR) theory [115–117] and for monoenergetic ions in the Bernstein, Rabinowitz theory [168]. These authors validated the applicability of the Lam theory to large probes while other theories are primarily useful for small probes. Niyogi and Cohen in their work developed a theory for an ionized collisional plasma from which space plasma parameters can be determined [169]. In addition to theory, other authors have carried out experiments to verify the accuracy of the proposed theoretical formulas. Saudit and Woods experimentally verified the accuracy of the OML and radial motion theories by comparing the result obtained with these theories, to measure ion and electron densities in long, low pressure cylindrical nitrogen and helium dc discharge when using a computer controlled Langmuir probe [139]. Also, Tuszewski and Tobin experimentally determined the ion densities in a low frequency inductively coupled discharge using ion saturated currents of a Langmuir probe [170]. However, the determination of plasma parameters experimentally in the laboratory is not the same as in space. This is due to plasma inhomogeneities in laboratory experiments resulting from the proximity of probes to the vacuum vessel walls and other components. Despite these shortcomings, analytic expressions have been and continue to be largely used to infer plasma parameters from probe characteristics, due to their relative simplicity. In space, other instruments such as incoherent scatter radars(ISR), digitalized ionosonde, global navigation satellite systems(GNSS), are also used to infer plasma parameters such as densities, temperatures, and flow patterns [171–174]. The interpretation of measurements obtained with these instruments also relies on different

theories and approximations as explained in Section 1.4 for incoherent scatter radars and ionosondes. Yet another technique, GNSS, is used to determine ionospheric slant and vertical total electron contents (TEC). From there, standard tomographic techniques can be used to construct 3D maps of ionospheric electron densities [175]. Detailed explanations on how different plasma parameters can be determined from digitalized ionosonde, ISR, and GNSS measurements can be found in the literature [45, 176–178]. These instruments have been used to independently validate or correct measurements made with Langmuir probes in space [179–182]. Comparisons between ground based observations and in-situ measurements nonetheless come with appreciable uncertainties, owing to significant differences in temporal and spatial resolutions. While probe measurements on a satellite in low Earth orbit can have a temporal resolution of ~ 10 ms, with a spatial resolution ~ 100 m along track, ground based measurements have a spatial resolutions of order 10 km horizontally and vertically, and temporal resolutions of order of many seconds. In this chapter, a new and promising approach to infer plasma parameters from Langmuir probe measurements, with quantified uncertainties, and a high potential for improved accuracy is presented. This approach combines results from 3D self-consistent kinetic simulations of probes in their environment, and adapted multivariate regression techniques. Computer simulations are used to calculate the currents collected by probes under a range of selected space environment conditions. These currents and the known environment conditions (densities, temperatures, ion masses, etc.) used as input in the simulations, are then used to construct a solution library, or synthetic data set from which inferences can be made using adapted regression techniques. The advantage of this simulation-regression approach is that it makes it possible to account for more realistic conditions and physical processes than what is possible analytically. Also, by following a machine learning technique, whereby models are trained on subsets of the synthetic data set, and validated on different subsets, it is possible to quantify uncertainties with which inferences are made. In this study, a simplified Swarm ge-

ometry is considered, which includes a segment of the ram-facing side of the satellite, the Electric Field Instrument faceplate, and the two Langmuir probes at the base of the satellite. The two probes are assumed to be at fixed potentials of 4 V and 5 V with respect to the satellite. Satellite potentials relative to the background plasma are varied between -3 V and 0 V, consistently with floating potentials inferred for the Swarm satellites, and reported in the Swarm data portal [183]. The resulting synthetic data set, covering a range of plasma densities, temperatures, effective ion masses, and satellite potentials, is then used to train inference models, and assess them against known input parameters used in the simulations.

In Section 3.2, I present the approach used in creating the solution library which covers a broad range of densities, temperatures, spacecraft potentials used as input in the simulations, and the computed currents collected by each of the two Langmuir probes. I describe three approaches used to construct models for the satellite floating potential V_s , the electron density n , and the ratio $n/\sqrt{T_{eV}}$, where T_{eV} is the electron temperature in electron-volts. Validation results obtained from applying these approaches to the synthetic data set are presented in Section 3.3. The models are then applied to Swarm in-situ measured currents, and inferences are compared with data reported on the Swarm satellite data portal. Also, using the same regression technique, models are trained using a subset of currents and reported electron densities, temperatures, and satellite potentials from in-situ measurements. These models are then applied to infer densities, satellite floating potentials and ratios $n/\sqrt{T_{eV}}$ from currents in a distinct subset, and regression inferences are compared with reported values in a different subset of data portal values. The differences in all these cases, are comparable to those found when training and validation are made with synthetic data. These comparisons show that this regression approach is not biased to synthetic data, and that given accurate data, the regression technique can be used to make good inferences, with known uncertainty margins. Finally, a summary of the

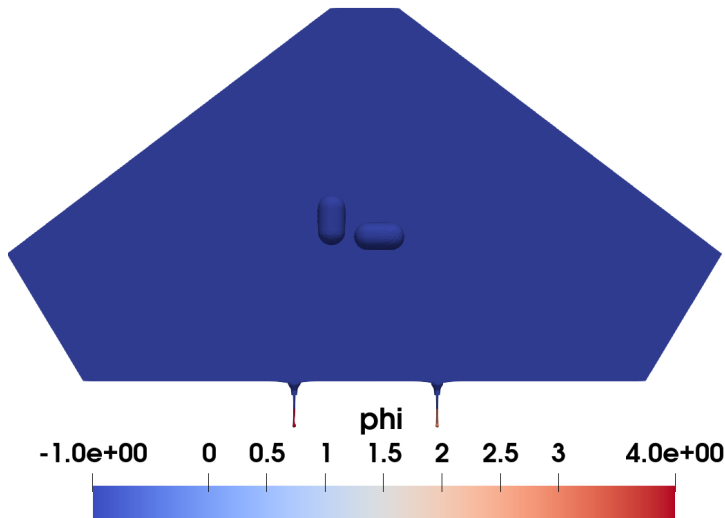


Figure 3.1: Illustration of an approximate truncated Swarm geometry used in the simulation, as seen from the ram side. Except for the probes and the “stubs”, all satellite components are assumed to be at the same potential V_s .

results and concluding remarks are presented in the Section 3.6.

3.2 Methodology

The approach adopted here to infer satellite and plasma parameters while accounting for a more realistic geometry of the Swarm satellites, closely follows the one used in Chapter 2 [118, 119]. It is summarized here for completeness.

3.2.1 Construction of a synthetic data set

The data set used in this chapter is derived from kinetic simulations of an approximate truncated Swarm geometry shown in Fig. 3.1. Cases where the two probes on the satellite are biased at fixed voltages of 4V and 5V with respect to the satellite, while varying the satellite potential with respect to the background plasma are simulated. It is assumed in the simulations that the spherical probes and the “stubs”; that is, the last segments of the post attaching the probes to the satellite, are at the same potential. All other satellite components, including the faceplate and the two shells of the thermal ion imagers (TII), are assumed to be at the satellite potential

Table 3.1: Sample probe voltages with respect to the background plasma, for a spacecraft floating potential ranging from -3 V to 0 V, assuming that probes are at a fixed bias voltages of $+4$ V, and $+5$ V.

$V_s(\text{V})$	$V_1(\text{V})$	$V_2(\text{V})$
-3	1	2
-2	2	3
-1	3	4
0	4	5

V_s . In recent years, the faceplate and the TII shells have often been biased to -3.49 V relative to the satellite, but for the period considered in Section 3.4, when settings were optimised for the TII, it was grounded to the satellite bus. Plasma with multiple ion species are considered, with both background ions and electrons described by Maxwellian velocity distribution functions with different drift velocities. Also, the presence of the geomagnetic field is neglected in the simulations. This is justified by the fact that, with positive probe voltages relative to the background plasma, probes mainly collect electrons for which a typical gyroradius ($\rho_e \gtrsim 2$ cm) is larger than the 4 mm probe radius. The relation between the satellite potential V_s , the probe bias voltage V_b , and probe voltage V relative to the background plasma is given in Eq. 2.1. This relation is illustrated in Table 3.1 with sample floating potentials assumed in the simulations. In the simulations, different space plasma parameters, including densities, temperatures, and ion compositions are assumed. These parameters are obtained from the International Reference Ionosphere (IRI) model, for plasma conditions at mid-latitudes, at different longitudes, and altitudes (from 450 to 500 km), and times of the day. The electron temperature ranges from 0.15 eV to 0.28 eV, the effective mass, from 8.3 amu to 15.9 amu, and the density from 10^{10} m^{-3} to 4×10^{11} m^{-3} . A summary of the plasma parameters used in the simulations is presented in Table 3.2, and the currents collected by each of the probes for these parameters are

Table 3.2: Simulation parameters used in the construction of the solution library.

n	T_e	m_{eff}	n_{O^+}	n_{H^+}	n_{He^+}	n_{N^+}
10^{10} m^{-3}	eV	amu	%	%	%	%
2.16	0.1613	8.30	93.14	6.07	0.53	0.26
2.33	0.1715	12.35	97.78	1.90	0.32	0.00
2.65	0.1516	8.31	93.15	6.06	0.53	0.26
2.67	0.1723	10.10	91.93	3.81	0.27	4.00
3.09	0.1778	12.73	97.92	1.66	0.27	0.15
4.40	0.2470	14.52	99.17	0.64	0.19	0.00
5.27	0.2470	14.30	99.01	0.75	0.19	0.05
6.48	0.2464	15.88	99.7	0.00	0.148	0.12
6.79	0.2722	14.59	99.16	0.61	0.17	0.06
7.18	0.2743	14.09	98.92	0.86	0.22	0.00
8.41	0.2772	13.80	98.69	1.02	0.22	0.07
10.32	0.2741	13.67	98.52	1.09	0.22	0.18
29.4	0.2426	15.87	95.37	0.00	0.05	4.58

calculated using PTetra, a three-dimensional particle-in-cell (PIC) code in which ions and electrons are treated kinetically [77, 144]. Collected probe currents calculated from the simulations made with satellite potentials 0, -1 , -2 , and -3 V are fitted using a simple second degree polynomial for each of the 13 sets of plasma parameters separately. In all cases, the maximum relative error between currents found from simulations and fitted values does not exceed 2%. Using these fits, a synthetic data set, or solution library, is constructed, which consist of a total of 200 nodes; each one consisting of currents and bias voltages for the two probes, followed by the corresponding plasma density, the electron temperature, the ion effective mass, and the satellite potential assumed in the simulations. The solution library is then subdivided into two disjoint subsets made of randomly selected elements; one being used to con-

struct the inference models and the other to assess, or validate the model skills. The models are then applied to in-situ measured currents obtained from Swarm satellite portal.

3.2.2 Analytic estimates

This approach leverages the approximate OML expression for the current collected by a spherical probe at a positive potential with respect to background plasma, to derive a simple formula for the satellite potential V_s and the ratio $n/\sqrt{T_{eV}}$ in terms of the currents collected by the two probes and their bias voltages with respect to the spacecraft as in Chapter 2. Equation 2.5 is used as a first approximation to determine the satellite potential by neglecting the term T_{eV} , due to the fact that this term is generally small compared to V_s in absolute value, and Eq. 2.7 is used to make a first estimate of $n/\sqrt{T_{eV}}$. This is done by direct substitution of the currents and bias voltages in the data set, for the two probes considered. These first analytic estimates can then be combined with regression techniques to produce more accurate inferences.

3.2.3 Affine Transformation

An affine transformation is a simple transformation which preserves collinearity in a distribution of points. Another interesting property is that it also preserves the Pearson correlation coefficient R between data sets, when applied to any one of the sets. Geometrically, an affine transformation is a combination of a translation and a scaling multiplicative factor. The general affine transformation is in the form:

$$\begin{bmatrix} Y_1 \\ Y_2 \\ \vdots \\ Y_N \end{bmatrix} = A \times \begin{bmatrix} X_1 \\ X_2 \\ \vdots \\ X_N \end{bmatrix} + B, \quad (3.1)$$

Where the Y s are the transformed values of the X s, A and B are the transformation coefficients. In what follows, affine transformations will be applied to analytically

inferred data, by choosing A and B so as to minimise the root mean square difference with known data values.

3.2.4 Radial Basis Function (RBF) approach

RBF is a method used to interpolate a function in a multivariate space of independent variables. The RBF approach is explained in more detail in Section 2.3.2 and it is expressed mathematically with Eq. 2.8. In this problem, X in Eq. 2.8 is a two-tuple set of currents collected by the two probes, and Y represents the plasma parameter of interest, to be inferred. The selection of the centers follows the same approach used in Section 2.3.2. However, the interpolating function used to construct the model in all cases considered in this chapter is $G = |I - I_j|^{1.8}$ using six centers, because it gives optimal results for the three quantities for which inference models are constructed. This approach is used to construct inference models for V_f , n , and $n/\sqrt{T_{eV}}$ using the training data set in the solution library.

3.2.5 Combination of Orbital Motion Limited (OML) and Radial Basis Function

In this boosting ensemble approach, OML and RBF are now combined to obtain inferences with more accuracy. This is done by first using the OML formulas to infer a plasma parameter and then RBF, to model and correct for the error in the first inference. The final models for V_f and $n/\sqrt{T_{eV}}$ are given in Eqs. 2.14 and 2.15 respectively. In these expressions, RBF is used to model the discrepancy between the actual data and analytic estimates.

3.3 Construction of Inference Models with Synthetic Data

In this section, inference models are constructed and assessed using synthetic data from the solution library. For each satellite potential, the analytic fits mentioned

above are used to determine the current collected by each probe. Each node, or entry in the solution library consists of two fitted collected currents, followed by the corresponding density, temperature, and satellite floating potential. The two currents are the independent variables used to infer the density, the ratio $n/\sqrt{T_{eV}}$, and the satellite floating potentials as dependent variables. Training and validation data sets are constructed as explained in Section 3.2.1. The training sets consists of 140 randomly selected nodes among the full solution library, and the validation set consist of the remaining 60 nodes. For the floating potential and the ratio $n/\sqrt{T_{eV}}$, three approaches are used to construct the inference models. The first makes use of combination of OML and the affine transformation. In this approach, the model is first constructed using the OML approximation in Eq. 2.6 for the V_s and Eq. 2.7 for the $n/\sqrt{T_{eV}}$. The inferred V_s and $n/\sqrt{T_{eV}}$ are then transformed using affine transformation to minimise the uncertainties in the inferred values. The second consists only radial basis function (RBF), while the third approach makes use of a combination of OML estimates, and RBF using Eqs. 2.14 and 2.15. However, for the electron density n_e , for which there is no approximate analytic expression involving only two currents collected for two different voltages, only RBF is used. The results obtained are presented by directly comparing inferences made with currents from the synthetic data set, against plasma parameters assumed in the simulations.

3.3.1 Spacecraft potential

The RBF and OML-RBF models for the V_s are constructed using the maximum absolute error as the cost function. This is minimised to obtain models with optimal inference skills. Figure 3.2a. shows the correlation plot of the V_s obtained when using only the OML formula against the actual data values. There is excellent affinity between these values as indicated in the value of the Pearson correlation coefficient $R= 0.976$ even though other metric values are low. This excellent affinity suggests

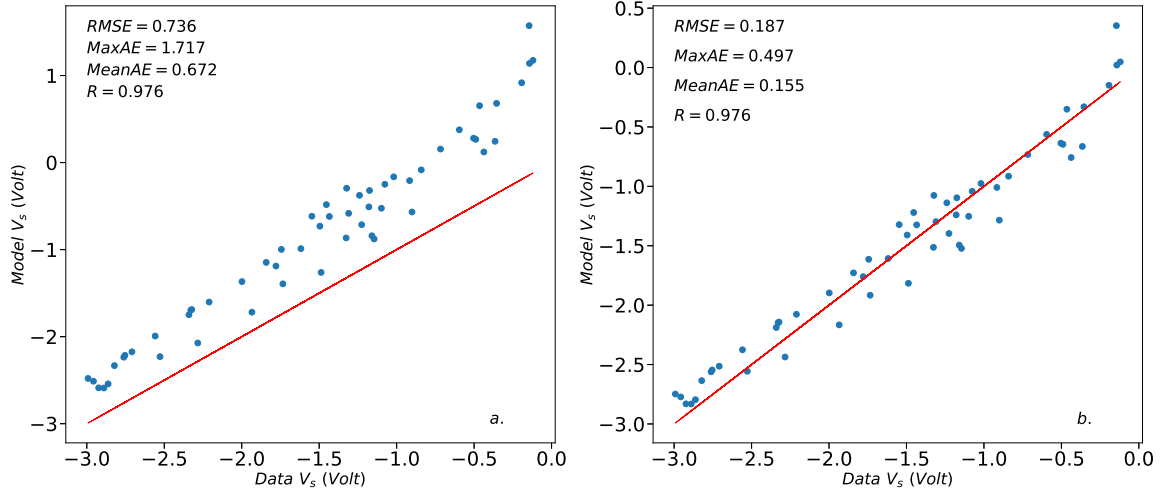


Figure 3.2: Comparison between spacecraft potentials inferred with (a) only the OML formula, and (b) a combination of OML and an affine transformation and known values in the synthetic validation set. The line corresponds to a perfect agreement between the two potentials. The maximum absolute error (MaxAE), the root mean square error (RMSE), the mean absolute error (MeanAE), and the Pearson correlation coefficient (R) are used as model skill metrics.

that an affine transformation can be applied to improve the inferences. Figure 3.2b. shows the correlation plot when an affine transformation is applied so as to minimise the RMS error between the two data sets. It shows a significant improvement in the accuracy of the model as the RMS error dropped from 0.736 to 0.187. Figure 3.3 shows the correlation plot between the RBF model inferences and actual data values from the validation set. The numerical values of the metrics in the plot indicate excellent qualitative and quantitative agreement between model inferences and known values from the validation set with reductions in the MaxAE, RMS error and MeanAE by factors ranging from ~ 3.5 to ~ 4.4 when compared to the OML inference in Fig. 3.2a. The results obtained for the third model when combining the OML and the RBF approach are shown in Fig. 3.4. The figure shows a similar trend as with the result obtained when using only RBF, although, the points are less scattered around the solid line than in Fig. 3.3. The improvement in the inferences resulting from the combined OML and RBF, compared to OML alone, is also clear from the numerical

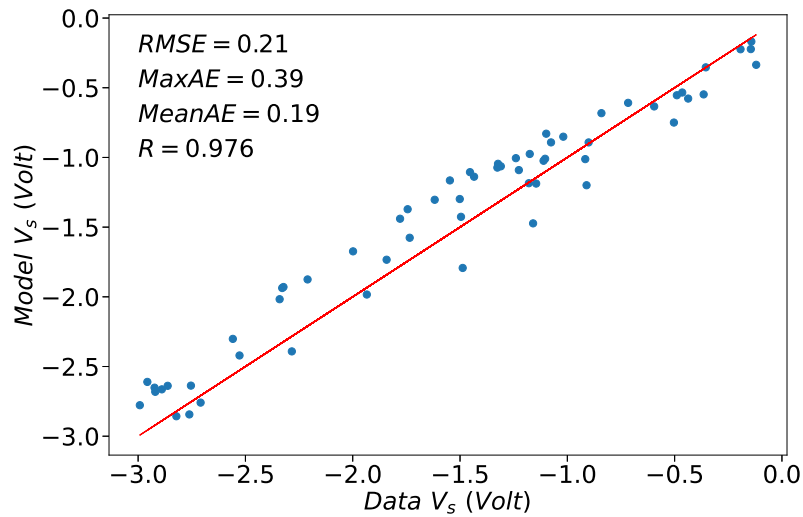


Figure 3.3: Comparison between spacecraft potentials inferred with RBF using six centers and known values in the synthetic validation set. The line corresponds to a perfect agreement between the two potentials. The maximum absolute error (MaxAE), the root mean square error (RMSE), the mean absolute error (MeanAE), and the Pearson correlation coefficient (R) are used as model skill metrics.

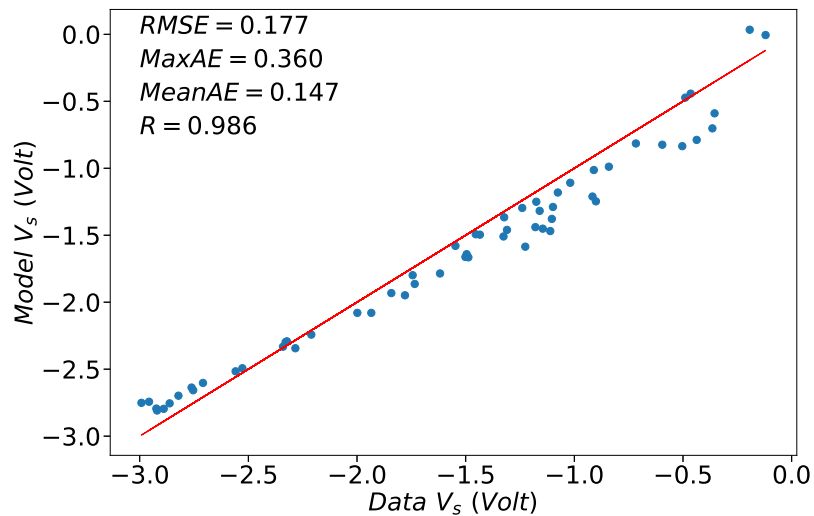


Figure 3.4: Comparison between spacecraft potentials inferred with a combination of analytic formula, and RBF with six centers, and known values from the validation set. The line corresponds to a perfect agreement between the two potentials

values of the metric coefficients, with reduction by 4.15, 4.77, and 4.57 for RMSE, MaxAE, and MeanAE respectively. In general, the RBF, the combined OML and RBF, and the combined OML and affine transformation all have similar inference skill, with the combined OML and RBF slightly better than the two other methods as summarised in table 3.3.

Table 3.3: Summary of discrepancies between inferred satellite potentials, with values in the synthetic data.

	RMSE	MaxAE	MeanAE	R
OML	0.736	1.717	0.672	0.976
OML-affine	0.187	0.497	0.155	0.976
RBF	0.210	0.390	0.190	0.976
OML-RBF	0.177	0.360	0.147	0.986

3.3.2 Plasma density

A model is also constructed for the electron density n_e , for which there is no approximate analytic expression involving only two currents collected for two different voltages. This is why in this case, RBF alone with six centres is considered. Here, the independent variables are two-tuples of currents collected by the probes. The comparison between model inferences and data in the validation set is shown in Fig.3.5. The three metrics used to assess the model skill are the MRE in Eq. 1.19, RMSrE in Eq. 1.21, and the Pearson correlation coefficient(R). The plot shows excellent correlation between the predicted densities and actual densities in the validation set, with a maximum relative error less than 13%.

3.3.3 Density divided by the square root of the temperature

An inference model is constructed for $n/\sqrt{T_{eV}}$. The choice of this dependent variable is motivated by Eq. 2.7, which is an exact consequence of the OML approximation,

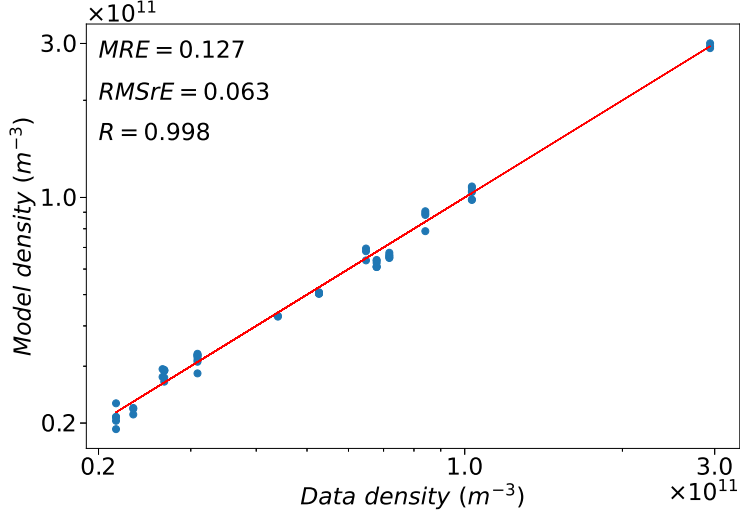


Figure 3.5: Comparison between electron densities obtained using RBF with six centers, and actual densities in the validation data set. The line corresponds to a perfect agreement between the two densities.

introduced in Section 2.3.1. While $n/\sqrt{T_{eV}}$ is not generally of particular interest to characterize the state of a plasma, an accurate inference of this ratio would be useful to determine one of the n or T_{eV} parameters if the other could be determined accurately by other means. In this case, three models are constructed using a combination of OML and an affine transformation, RBF alone using Eq. 2.8, and a combination of the RBF and the OML approximation using Eq. 2.15. Figure 3.6 shows the correlation plot when (a) only OML is used, and (b) when an affine transformation is applied to correct the first OML inferences. The figure shows the improvement in the inference when the affine transformation is combined with the OML, with the MRE decreasing from the initial 74% when only OML is used, to 22%. Correlation plots for inferences with RBF alone, and with combined RBF and OML are shown in Figs. 3.7 and 3.8.

In both cases, model inferences show an excellent qualitative agreement with data from the validation set. Quantitatively however, the calculated skill metrics, show an appreciable improvement in the inferences when RBF is combined with OML as summarised in table 3.4.

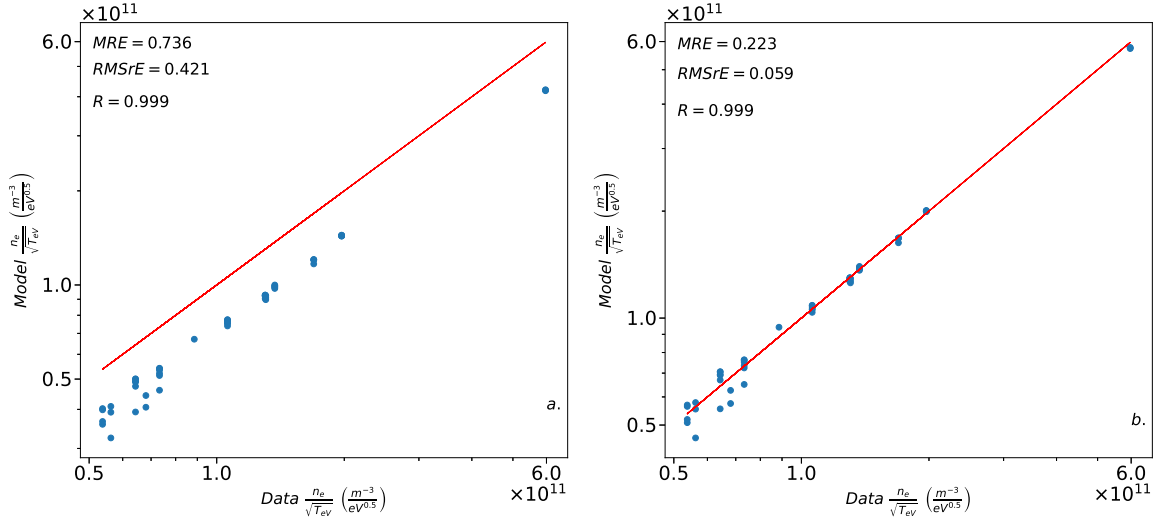


Figure 3.6: Comparison between $\frac{n}{\sqrt{T_{eV}}}$ inferred with (a) OML only, (b) a combination of OML and affine transformation, and actual data in the validation set. The line corresponds to a perfect agreement.

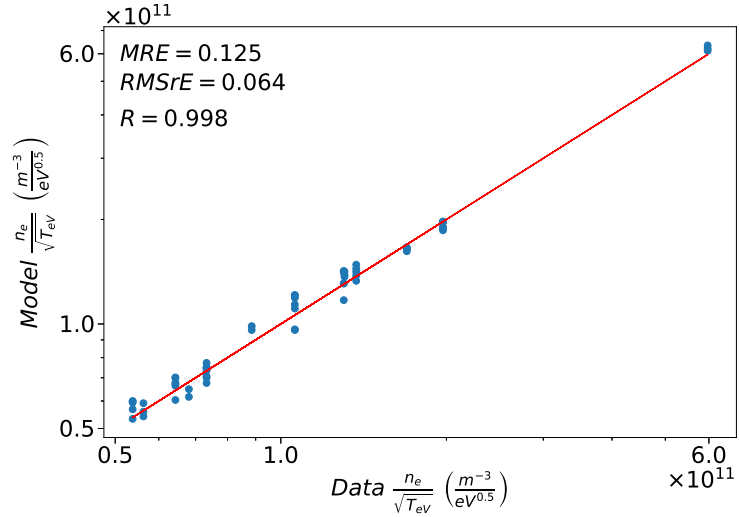


Figure 3.7: Comparison between $\frac{n}{\sqrt{T_{eV}}}$ inferred with RBF using six centers, and actual data in the validation set. The line corresponds to a perfect agreement.

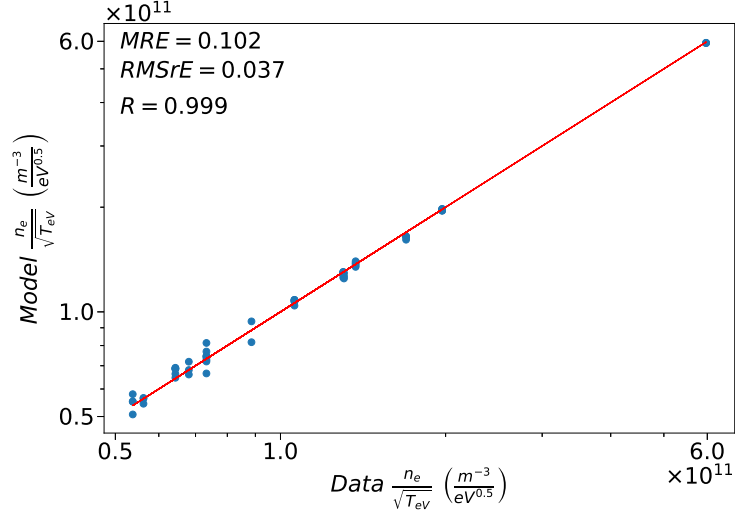


Figure 3.8: Comparison between $\frac{n}{\sqrt{T_{eV}}}$ inferred with combined OML and RBF using six centers, against data in the validation set. The line corresponds to a perfect agreement.

3.4 Application of models to in-situ measurements

The models constructed in Section 3.3 using synthetic data are now applied to experimental data obtained from the Swarm A satellite. Swarm A is one of the three satellites deployed by the European Space Agency (ESA) in 2013, with accurate monitoring of the Earth’s magnetic field as the primary objective. The satellite carries different types of instruments designed for specific purposes but this study’s focus is on the spherical Langmuir probes. The Swarm Langmuir probes are, most of the time, operated in a modulated-bias harmonic-amplitude-ratio detection mode, where the bias is not swept, but set to only three different values within a measurement cycle [184]. At each setting, there is a small sinusoidal modulation of the bias at typically about 100 Hz. This allows a relatively accurate estimations of the derivative of the I-V curve at these points. The probes are also operated in sweep voltage mode, once every 128 s for a duration of 1 s. In this mode, bias voltages are varied between the maximum range of -5 V and 5 V. Swarm probes have not been operated in fixed bias mode, which would correspond to the situation considered in the simulations, where

Table 3.4: Summary of errors between inferred $n/\sqrt{T_{eV}}$ and values in the synthetic data.

	RMSrE	MRE	R
OML	0.421	0.736	0.999
OML-affine	0.059	0.223	0.999
RBF	0.064	0.125	0.998
OML-RBF	0.037	0.102	0.999

currents are collected from probes at fixed 4 V and 5 V bias voltages. In order to apply the trained models to Swarm measured currents, one of the Swarm Langmuir probes (Probe 2) characteristics obtained in sweep voltage mode is considered, and currents collected with the 4 V and 5 V assumed in the simulations are selected. This is done by first analytically fitting measured characteristics in an interval of bias voltages, which includes 4 V and 5 V, and from there, interpolating the currents collected at these voltages. These currents are then used in the models, assuming that the interpolated currents approximate the currents which would be collected simultaneously by fixed bias probes at these voltages. Data collected during 3 days which are the *1st*, *2nd*, and *4th* of February 2014, when sweep voltages extended up to +5 V are used for the analysis. From this, a new data set, the Swarm-based set, is constructed consisting of measured currents with densities, floating potentials, and temperatures as reported in the L1b Langmuir probe data set. In order to avoid extrapolating beyond the range of parameters used to train the models, data with currents beyond those found from the simulations were not included in the Swarm-based data set. As a first consistency check, the overlap between the currents obtained in the simulations and those measured in space are shown in Fig. 3.9, in which the currents collected at 4 V is plotted as a function of currents collect at 5 V for both the synthetic data set (blue circles) and in-situ measurements (red squares). The figure shows that the

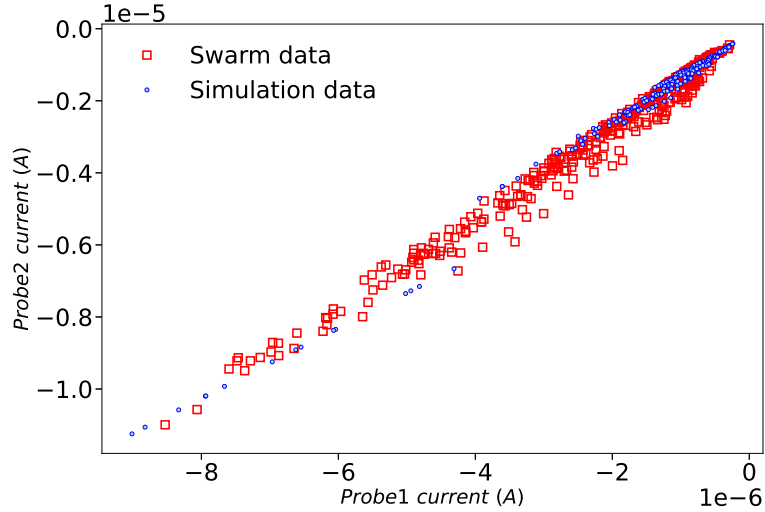


Figure 3.9: Current collected by the +4 V probe against the current collected by the +5 V probe, for both synthetic data and in-situ data.

two data sets have a similar range of values, with more points clustering at the higher current values. The two-tuples of currents from the Swarm data set are then used as input in the models, which were trained using simulation-generated synthetic data as described in Section 3.2. These models are then used to infer the same physical parameters as in Sections 3.3.1 to 3.3.3. Inferences are then compared with corresponding physical parameters reported on the Swarm data portal. It should be noted that these comparisons between the model inferences and the reported values on the Swarm portal are not meant to assess the accuracy of the models, but rather to check the consistency between the inferences and those reported on the Swarm A data portal. At this stage, in the absence of accurate, independently measured plasma parameters, with quantified uncertainties, it is unfortunately not possible to determine if, and if so, to what extent the inferences constitute an improvement in accuracy compared to those reported. The comparison is nonetheless of interest, as data reported on the Swarm data portal are deemed state of the art, with which improved inferences are expected to agree, at least qualitatively.

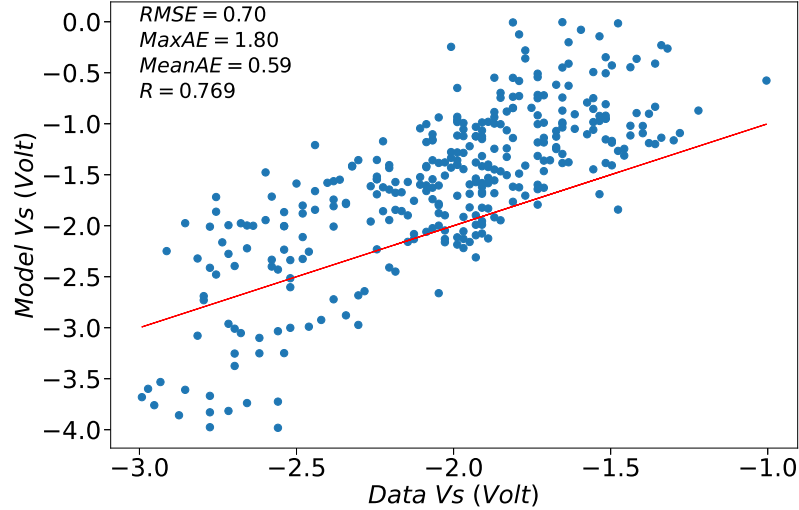


Figure 3.10: Correlation plot of RBF inferred satellite potential, and values reported on the Swarm data portal for 04/02/14, from 00:00 UTC to 23:59 UTC. The solid line corresponds to a perfect agreement.

3.4.1 Inference of in-situ floating potentials

The satellite potential is first inferred using a model constructed with RBF alone, followed by a combination of the OML and affine transformation, and then, with a combination of the OML approximation and RBF. Inferences are compared to the potentials reported on the Swarm data portal in Figs. 3.10, 3.11 and 3.12, with inferred values of V_s in ordinate, against reported values shown on the abscissa.

With RBF alone, the spread around the perfect correlation line is noticeably larger than with inferences using the combination OML-affine transformation and combination OML-RBF. Moreover, with RBF alone, several inferred values of the floating potential can be significantly lower than -3 V, which is the lower bound of satellite potentials used to train the model. It is noteworthy, as seen in Fig. 3.9, that these extrapolated inferred values are obtained with the currents in the same range as those used to train the model. In contrast, in Fig. 3.11 and 3.12, inferences made with the combination OML-affine transformation and combination OML-RBF model, using the same in-situ data set, are all consistently within the range of floating potentials

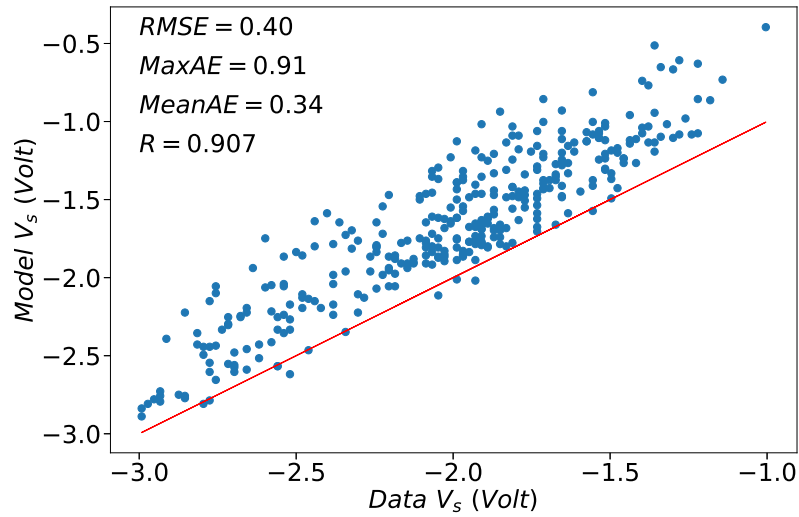


Figure 3.11: Correlation plot of the combined OML-affine transformation inferred satellite potentials, and values reported on the Swarm data portal for 04/02/14, from 00:00 UTC to 23:59 UTC. The solid line corresponds to perfect agreement.

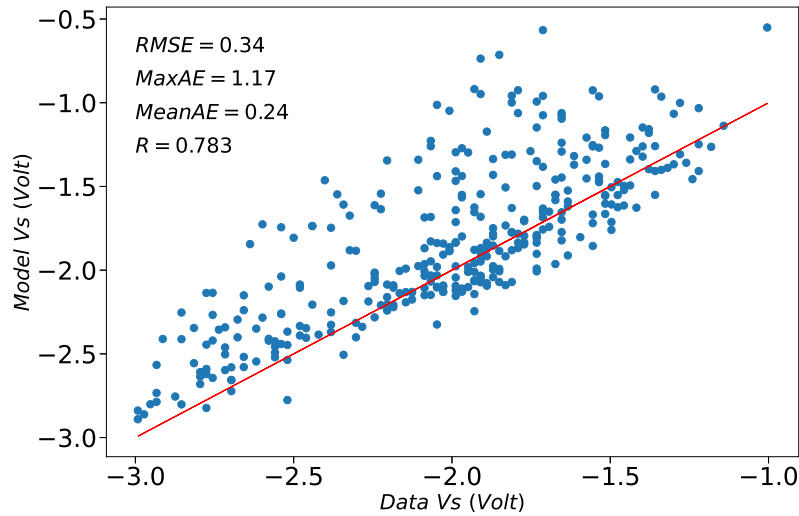


Figure 3.12: Correlation plot of the combined OML- RBF inferred satellite potential, and that reported on the Swarm data portal for 04/02/2014, from 00:00 UTC to 23:59 UTC. The solid line corresponds to perfect agreement.

considered in the synthetic data set. Also, most of the inferences from the combination OML-affine transformation model are above the perfect correlation as shown in Fig. 3.11. A comparison between the two figures shows that the Pearson correlation, and other skill metrics are higher (lower discrepancies) when RBF is combined with OML. This observation differs from what was found in Section 3.3.1 where the combined OML-RBF model performed better in all the metric assessment with the synthetic validation data set. A plot of the spacecraft potentials inferred using the OML-RBF model, OML-affine transformation model and the values reported on the Swarm portal as a function of time is shown in Fig. 3.13 for four consecutive intervals extending over a 12-hour period. The figure shows a general similarity between the three inferred floating potentials with occasional larger deviations occurring mostly at the larger ($\gtrsim 50^\circ$) latitudes, and fewer at low latitudes. The OML-RBF and OML-affine inferences show more similarity at the larger ($\gtrsim 50^\circ$) latitudes compared to the reported values. The agreement between the inferred satellite potentials using both models, and those reported on the Swarm data portal are found to be generally good at low and mid-southern latitudes. Note that the gaps between the points, filled with dashed lines in the plots, result from the removal of data outside the range of simulated currents in the synthetic data. The skill metrics calculated for each of the three days of in-situ data considered are summarized in Table 3.5.

In all three periods, OML-RBF inferences are closest to reported values, followed closely by OML-affine. This is interesting in view of the fact that both OML approximation, and the affine transformation are significantly simpler than RBF, which could make this technique a method of choice in practice.

3.4.2 Inference of in-situ densities

The model used for the density inference is the same as in Section 3.3.2. It is constructed with synthetic data, using RBF only, with six centers. No combination of RBF with OML is used here because there is no analytic approximation for the den-

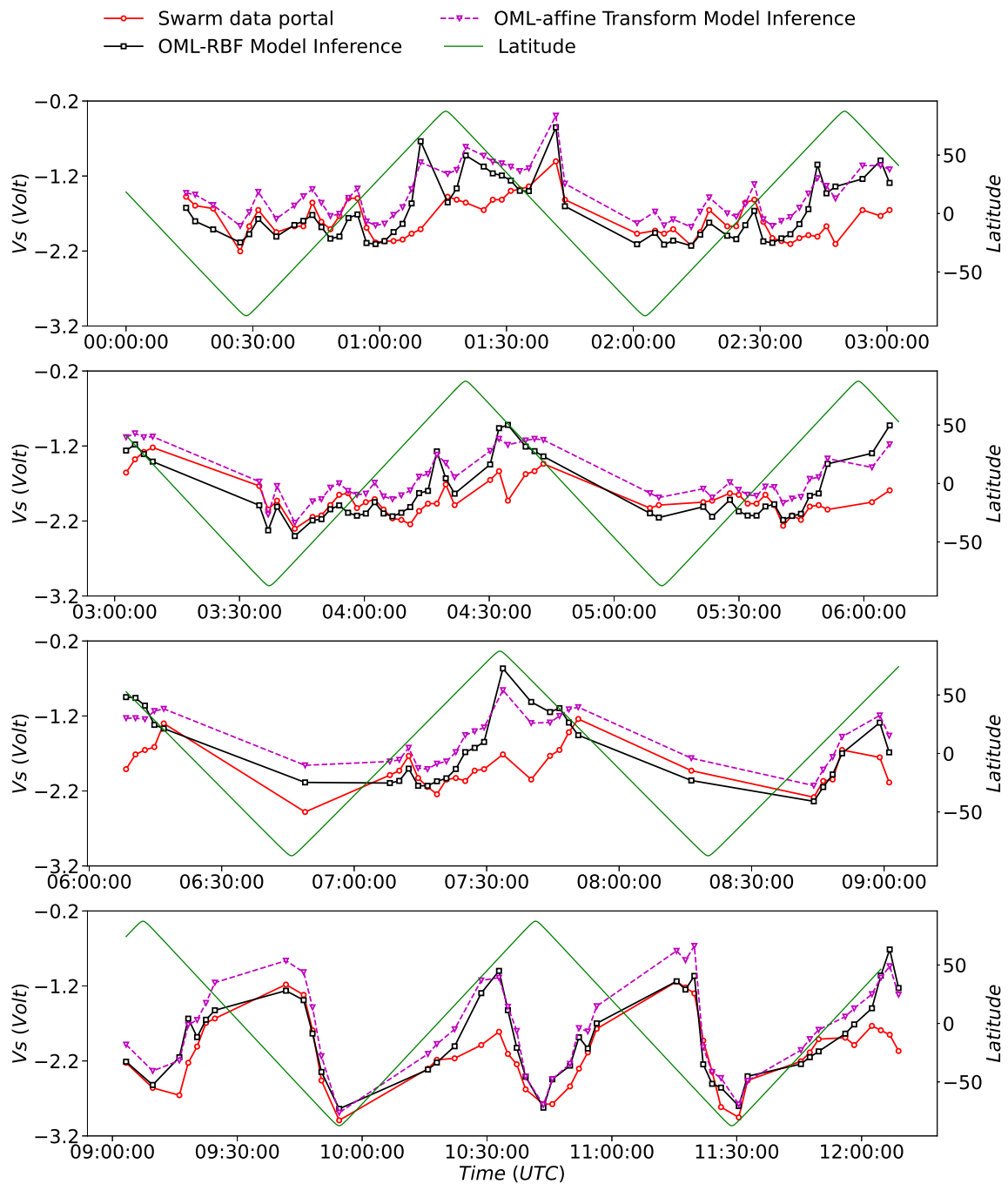


Figure 3.13: Plot of satellite potential using the OML-RBF model (black), OML-affine transformation model (purple), the satellite potential reported on the Swarm portal (red), and the latitude (green) against time for a twelve-hour period on 04/02/2014. The panels show four consecutive three-hour periods from 00:00 UTC to 12:00 UTC that day.

Table 3.5: Summary of discrepancies between inferred satellite potentials, with those reported on the Swarm data portal, over three days considered.

Day		RMSE	MeanAE	R
01/02/2014	RBF	0.61	0.44	0.719
	OML-RBF	0.34	0.26	0.850
	OML-affine	0.41	0.31	0.911
02/02/2014	RBF	0.54	0.37	0.433
	OML-RBF	0.37	0.25	0.773
	OML-affine	0.44	0.33	0.890
04/02/2014	RBF	0.70	0.59	0.769
	OML-RBF	0.34	0.24	0.783
	OML-affine	0.40	0.34	0.907

sity in terms of two currents measured with probes at two fixed bias voltages. The model is applied to Swarm experimental data and a correlation plot between inferred densities and densities reported on the Swarm data portal are shown in Fig. 3.14. The plot shows general similarity between inferences and reported values, but with significant scatter, and mostly lower values than reported, particularly for the lower densities. Although model inferences are smaller than the reported values with an RMSrE of 0.70 as summarized in Table 3.6, the RBF inferred densities plotted as a function of time of the day in Fig. 3.15 clearly follow a similar pattern as the ones reported on the Swarm data portal.

It is also noted that, as for the floating potential, the main discrepancies between RBF inferred density and Swarm portal densities, occur near the higher northern latitudes. In contrast, the agreement between the inferences is generally good in southern latitudes, as observed in Fig. 3.13 for the satellite potential V_s .

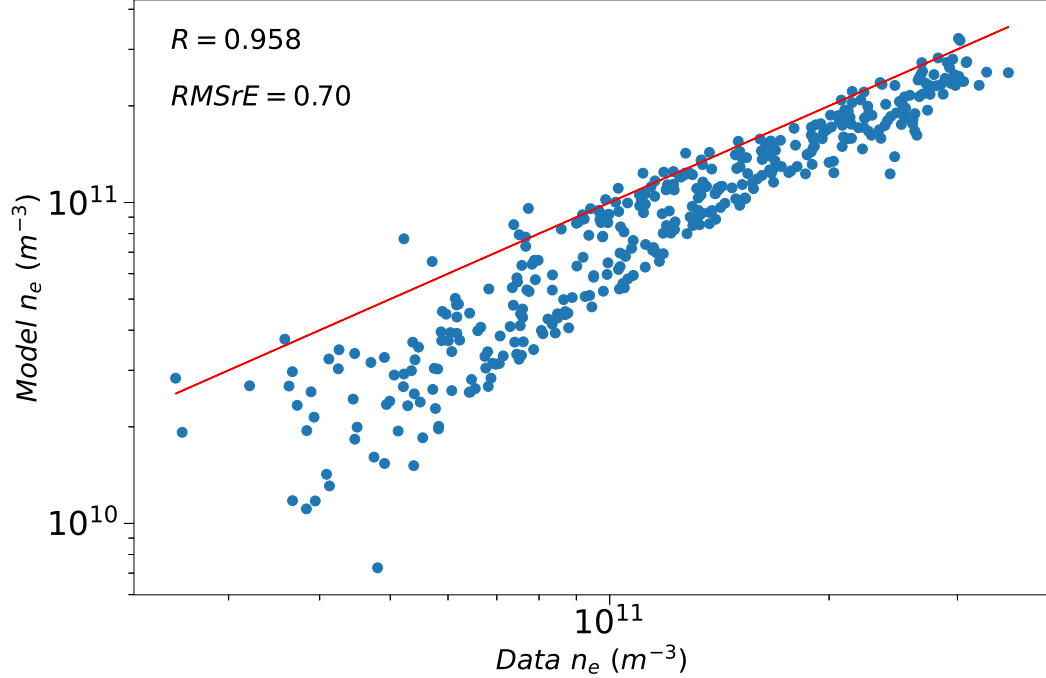


Figure 3.14: Correlation plot of density inference using the RBF model and reported density on the Swarm portal for 04/02/2014, from 00:00 UTC to 23:59 UTC. The solid line corresponds to perfect agreement.

Table 3.6: Summary of RBF density inference discrepancies with reported values from the Swarm data portal, computed over three days

Day		R	RMSrE
01/02/2014	RBF	0.978	1.02
02/02/2014	RBF	0.977	0.94
04/02/2014	RBF	0.958	0.70

3.4.3 Inference of in-situ $\frac{n}{\sqrt{T_{eV}}}$

As seen with Eq. 2.7, in the OML approximation the ratio between the electron density and the square root of the temperature can be expressed exactly in terms of two measured currents and corresponding bias voltages. Following the approach in 3.3.3, the three models constructed using synthetic data, to infer $n/\sqrt{T_{eV}}$ using measured currents, and to compare with values of that same ratio calculated with

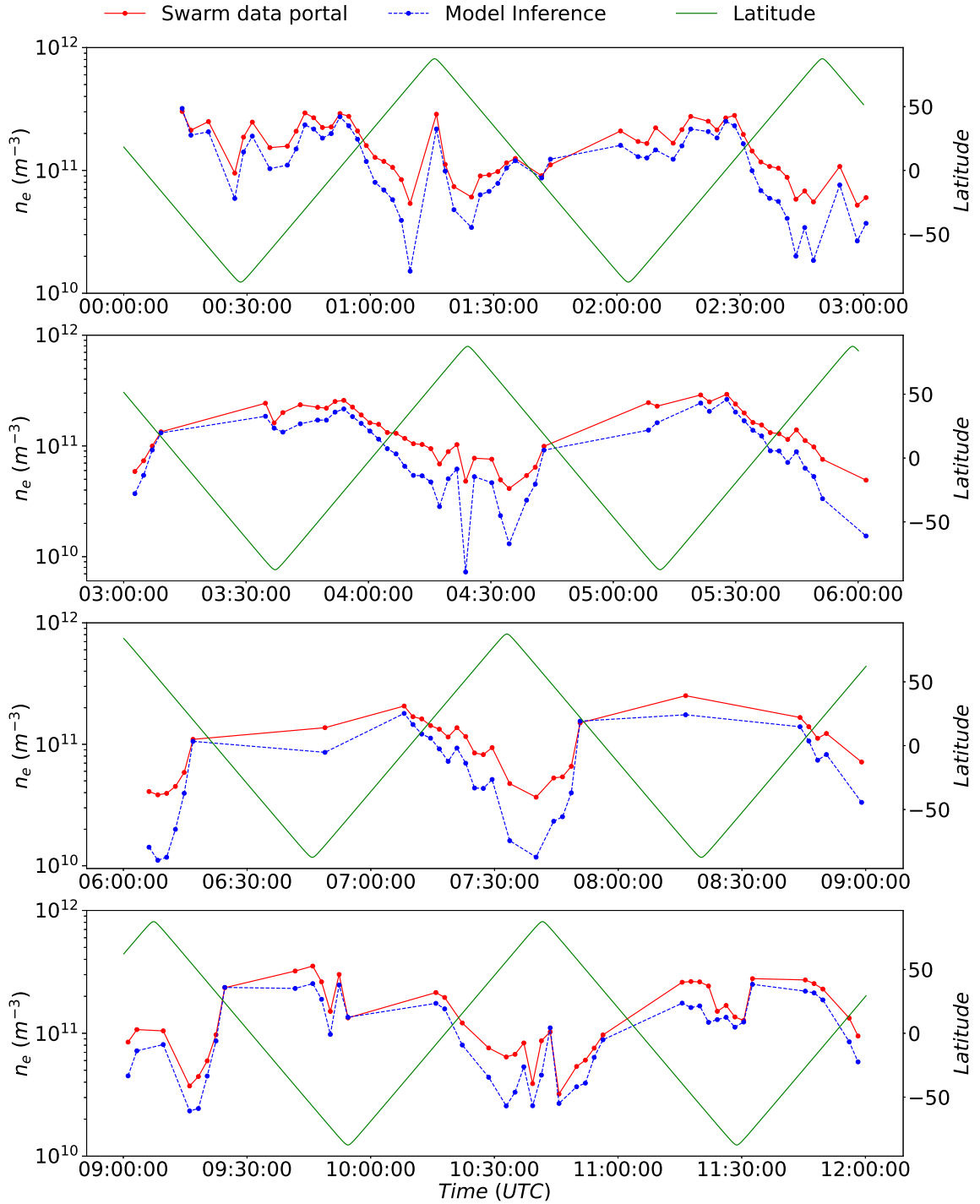


Figure 3.15: Plot of densities inferred using the RBF model and densities reported on the Swarm portal against time for a twelve-hour period on 04/02/2014. The panels show four consecutive three-hour periods from 00:00 UTC to 12:00 UTC that day.

reported values of the density and temperature on the data portal. The correlation plots in Figs. 3.16, 3.17, and 3.18, obtained respectively with RBF only, combined OML-affine transformation, and combined OML-RBF, show nearly identical results, both qualitatively and quantitatively as measured with the Peterson correlation and the RMSrE.

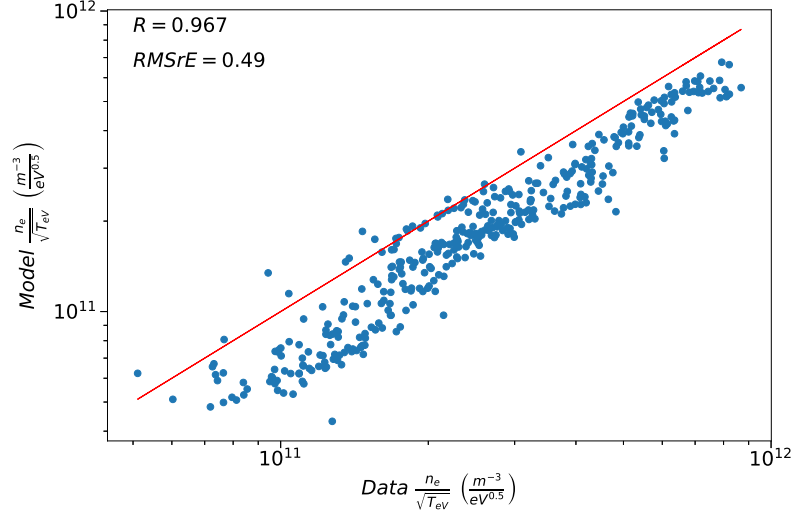


Figure 3.16: Correlation plot of RBF inferred $\frac{n_e}{\sqrt{T_{eV}}}$ and calculated values from densities and temperatures reported on the Swarm portal for 04/02/2014, from 00:00 UTC to 23:59 UTC. The solid line corresponds to perfect agreement.

The strong similarity is also visible in Fig. 3.19 showing the inferred and reported values $n/\sqrt{T_{eV}}$ for four consecutive intervals extending over a 12 hour period. In general, the three inferences overlap and they are smaller than the reported values on the Swarm portal. This observation differs from the similar comparison made with the synthetic validation set in Figs. 3.6, 3.7 and 3.8, where the combination of RBF and OML produced slightly more accurate inferences than the two other methods. A point worth noting in Figs. 3.14 to 3.19 is that, as for the density, the inferred values of $n/\sqrt{T_{eV}}$ are generally lower than those calculated from reported values of n and T_{eV} on the Swarm portal. This similarity with n is not surprising, considering that the ratio considered here depends more strongly on the density, than on the temperature and the fact that the ratio between the maximum to the minimum value

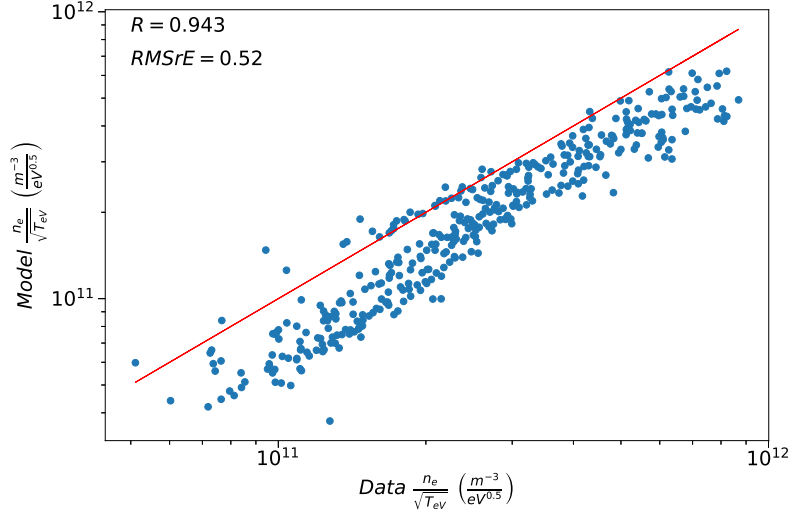


Figure 3.17: Correlation plot of the combined OML-affine transformation inferred $\frac{n}{\sqrt{T_{eV}}}$ and calculated values from densities and temperatures reported on the Swarm portal for 04/02/2014, from 00:00 UTC to 23:59 UTC. The solid line corresponds to perfect agreement.

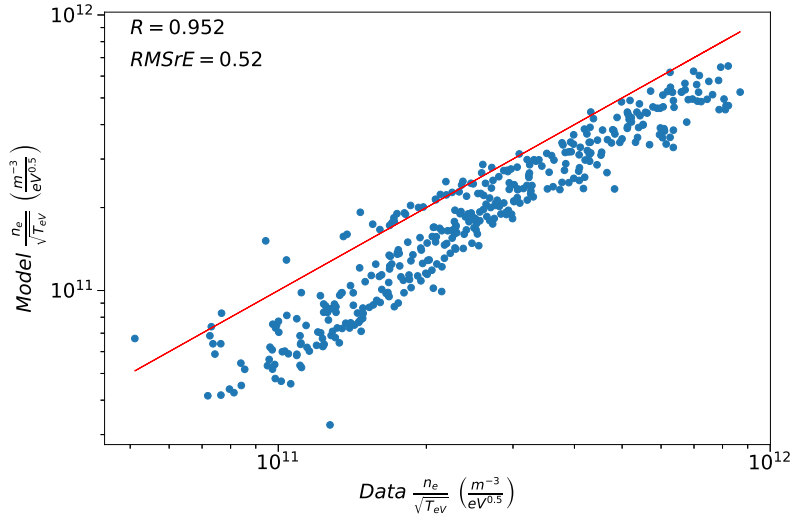


Figure 3.18: Correlation plot of combined OML-RBF inferred $\frac{n}{\sqrt{T_{eV}}}$ and calculated values from densities and temperatures reported on the Swarm portal for 04/02/2014, from 00:00 UTC to 23:59 UTC. The solid line corresponds to perfect agreement.

of the densities considered, is larger than that of the temperatures. Another point of interest, which contrasts with the comparisons made for V_s and to a lesser extent, for n , is that the magnitudes of the discrepancies between the two inferences shows

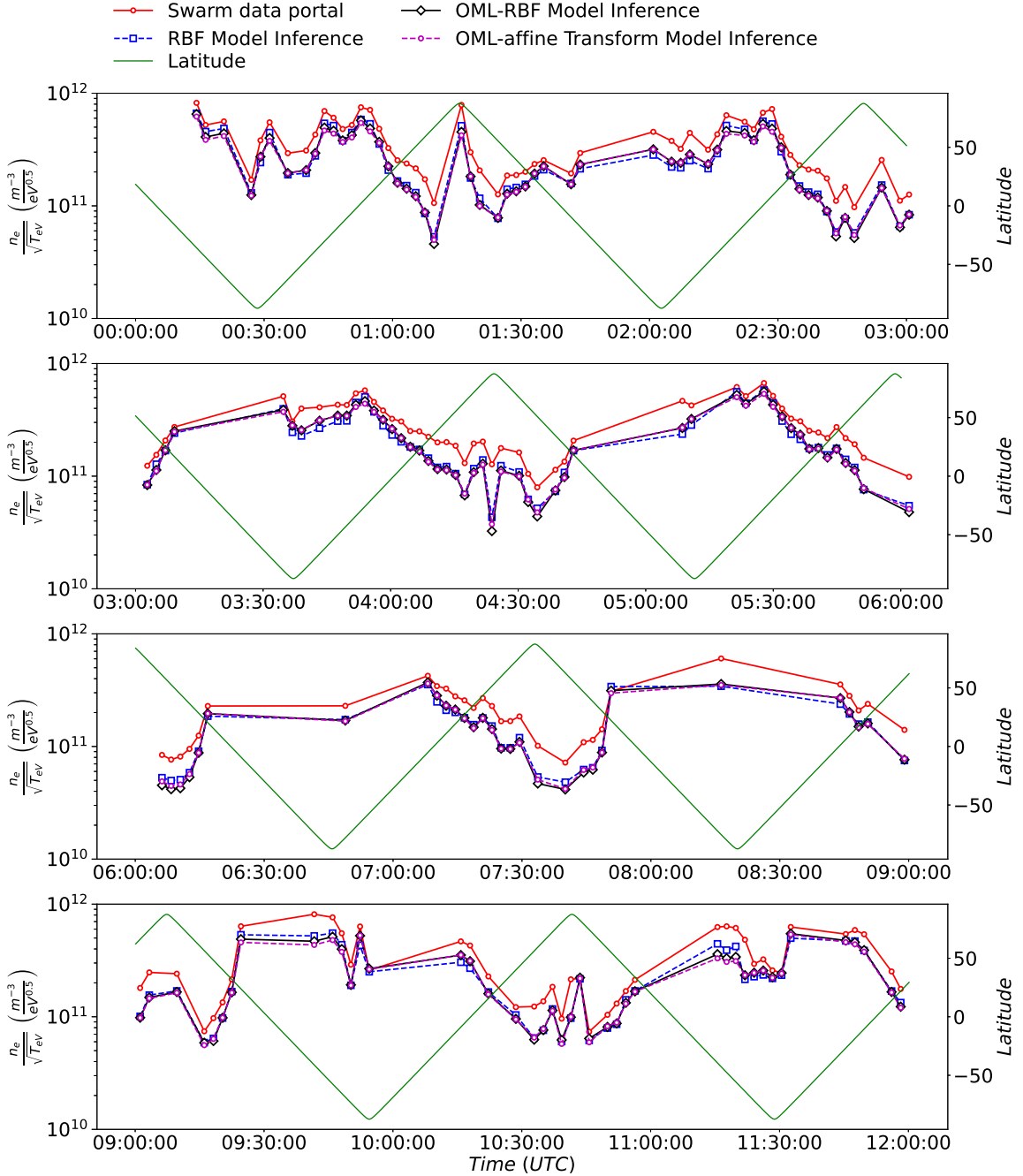


Figure 3.19: Comparison between inferred $\frac{n_e}{\sqrt{T_{eV}}}$ using RBF models (blue colour), OML-RBF model (black colour), OML-affine transformation model (purple colour) and calculated values from densities and temperatures reported on the Swarm portal as a function of time for a twelve-hour period on 04/02/2014. The panels show four consecutive three-hour periods from 00:00 UTC to 12:00 UTC that day.

less dependence on the latitude. In particular, there is significantly less difference in the discrepancies between the two inferences made at the higher and lower latitudes. Table 3.7 gives the skill metrics calculated for the three days of in-situ data considered.

Table 3.7: Summary of result discrepancies from the $\frac{n}{\sqrt{T_{eV}}}$ model.

Day		RMSrE	R
01/02/2014	RBF	0.68	0.975
	OML-RBF	0.78	0.978
	OML-affine	0.72	0.973
02/02/2014	RBF	0.59	0.974
	OML-RBF	0.66	0.975
	OML-affine	0.64	0.975
04/02/2014	RBF	0.49	0.967
	OML-RBF	0.52	0.952
	OML-affine	0.52	0.943

3.5 Training with in-situ measurements

In the previous sections the good qualitative agreement between simulation-regression inferences and those from in-situ measurements using state of the art techniques, are seen as encouraging. These comparisons, however, are not sufficient to determine if, or to what extent, the regression approach provides more accurate inferences, because that would require independent accurate and validated measurements, with known uncertainty margins. This task is unfortunately beyond the scope of this study, but nonetheless, the regression component of this approach can be assessed by training and validating models constructed exclusively with measured currents and plasma parameters reported on the Swarm data portal. This is to verify whether the regression algorithm is not biased to synthetic data, and show that a model trained

with accurate data, whether synthetic or experimental, would produce good quality inferences. To this end, 151 randomly selected entries from the Swarm data portal, consisting of collected current pairs by the gold-plated probe biased at 4 V, and 5 V, and reported satellite floating potentials, densities, and calculated densities divided by the square root of the temperature, were used to train models for each of these three parameters. A different set consisting of 201 entries was used for validation. In all cases, as in Section 3.2.1 with synthetic data, RBF training and regressions are made using six centers.

Floating potentials inferred from currents in the validation set are compared with reported values in Fig. 3.20. In this case, OML inferences are very different from potentials expected from either synthetic data or reported values from the data portal, for the combined OML-RBF or OML-affine method to be practical. This is why only inferences obtained with direct RBF are considered. Despite the larger RMS error

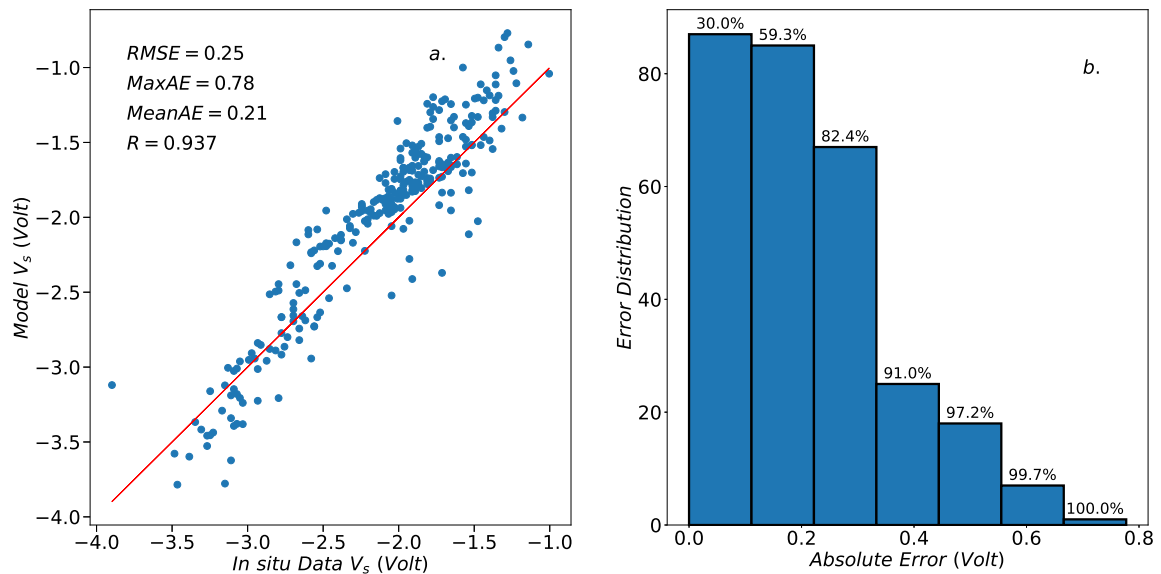


Figure 3.20: Correlation plot (a) of RBF inferred floating potentials with six centers and reported values on the Swarm portal, and (b) histogram of the distribution of the absolute errors in the model inferences.

of 0.25 V compared to 0.21 V found in Fig. 3.3 for the synthetic data, consistency with reported potentials from the validation set are seen to be significantly better

than in Fig. 3.12, with an RMS error of 0.34 V. The histogram in the figure shows that consistently with the RMS error of 0.25 V, approximately 68% of the inferences, corresponding to one sigma in a normal distribution, are in error by less that 0.2 V. Similarly, Fig. 3.21 shows a correlation plot of inferred values of the RBF-inferred electron densities, and validation densities from the data portal. Here again, while

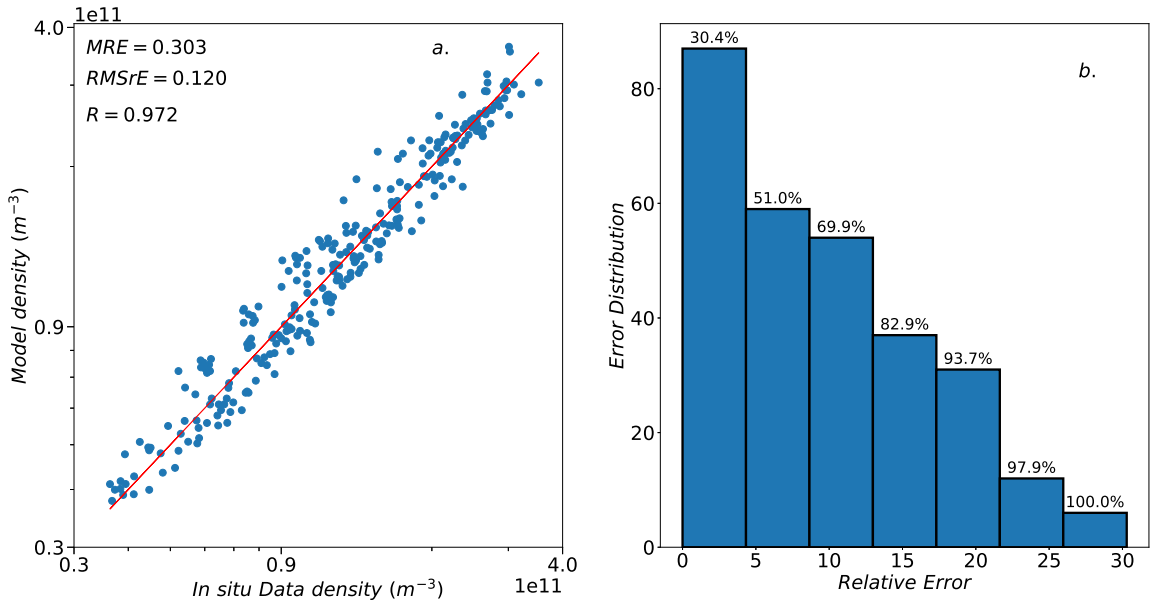


Figure 3.21: Correlation plot (a) of RBF inferred electron densities with six centers, and reported validation values from the Swarm portal, and (b) histogram of the distribution of the relative errors in the model inferences.

the inference skill, with a maximum absolute value of the relative error of 12% is larger than the 6.3% found in Fig. 3.5, inferences are significantly more consistent with reported densities than in Fig. 3.5, with a RMSrE of 70% when the RBF is trained with synthetic data. In this case, the histogram in panel b shows that 90% of the inferred values are in error by less that 20%. Lastly, Fig. 3.22 compares inferred values of $n/\sqrt{T_{eV}}$ with this same ratio from reported data in the validation set. As in the previous two comparisons, the quantitative agreement between inferred and reported values, with a RMSrE of 12% is comparable to what was found in Figs. 3.7 and 3.8, with RMSrE values of order 6%. These relative errors in turn are signif-

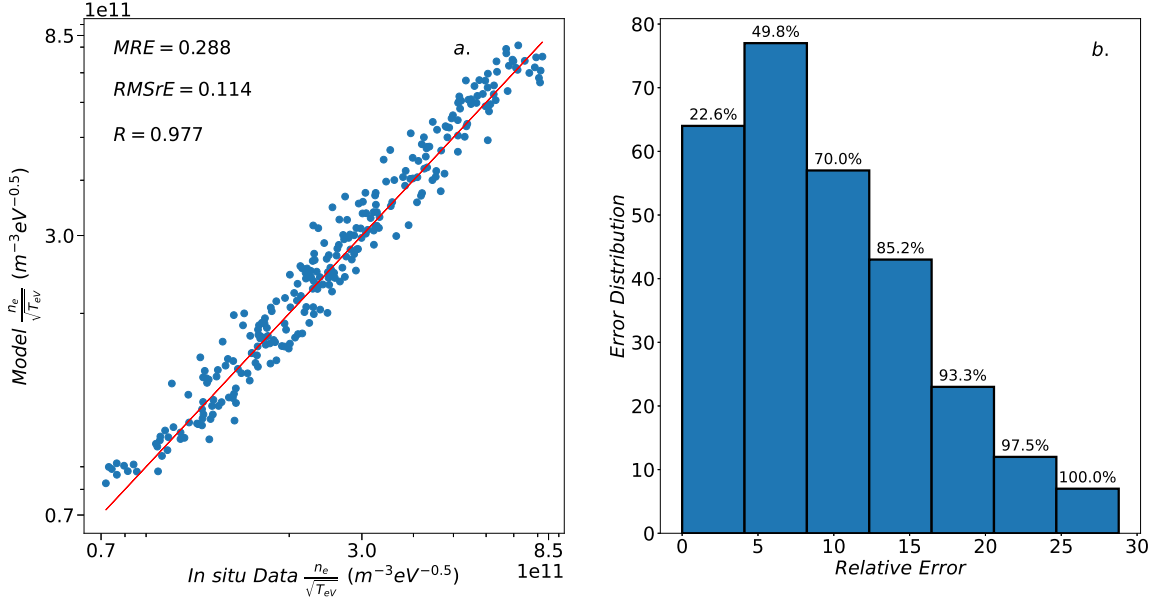


Figure 3.22: Correlation plot (a) of RBF inferred $\frac{n}{\sqrt{T_{eV}}}$ with six centers and calculated values from densities and temperatures reported values on the Swarm portal, and (b) histogram of the distribution of the relative errors in the model inferences.

icantly lower than in Figs. 3.16 and 3.18 with a RMSrE values of order 50%, and the histogram in part b shows that approximately 90% of the inferences have errors lower than 15%. The larger errors in the inferences here compared to inferences made with synthetic data are likely due to the fact that in-situ measured currents exhibit more variability than simulated currents, due to conditions not accounted for in the simulations, as well as differences in the temporal and spatial sampling.

In summary, models trained and validated with experimental data only, have comparable skills to those in Section 3.3 where training and validation is made with synthetic data. This finding confirms what was reported by Guthrie, et al. [185] in which a similar approach was applied to data collected in the Visions-2 rocket mission. This shows that the regression technique used is not biased to a particular data set, and that given training and validation sets, whether from simulations or accurate and validated measurements, good inferences of plasma parameters can be made with

regression techniques similar to the ones used in this chapter.

3.6 Summary and Conclusion

A new and promising approach is presented and applied to infer satellite and plasma parameters from currents collected by two spherical Langmuir probes at fixed bias voltages relative to a spacecraft. The method consists of constructing a synthetic data set, or solution library, from three-dimensional particle-in-cell (PIC) kinetic simulations. A subset of the solution library is used as a training set, from which a multivariate regression inference model is constructed, and assessed using the remaining subset for validation. This procedure, following machine learning approaches, enables a validation of the inference models, with quantifiable uncertainties. The PIC code PTetra used in the simulations reproduces probe characteristics calculated analytically in the OML approximation, under conditions when this model is valid [77, 144]. It was also benchmarked against independently developed codes [186, 187], and applied to in-situ rocket measurements [185]. In addition to reproducing analytic results, kinetic simulations can account for more physical processes, and more realistic geometries under which measurements are made, than what is possible analytically. The combination of kinetic simulations and regression techniques to directly infer space plasma parameters, or to improve the accuracy of approximate analytic inferences, is a promising option to go beyond analytic approximations, and improve space plasma metrology. Models have been constructed for the satellite potential V_s , the electron density n , and the ratio between the density and the square root of the temperature in eV, $n/\sqrt{T_{eV}}$. Each model was first constructed and assessed on the basis of the synthetic data set, in which all parameters to be inferred are known since they appear as input in the simulations. The root mean square (RMS) error was found to be less than 0.18 V for satellite potentials in the range $[-3, 0]$ V, when RBF is used in combination with the approximate analytic estimate in Eq. 2.3.1. For $n/\sqrt{T_{eV}}$ both direct RBF, combined OML-affine transformation, and combined OML-RBF have been used, and

found to yield comparable skills, but with the latter being slightly more accurate, with a RMS relative error lower than 4%. Only direct RBF regression was used to construct a model for density with a RMS relative error of 6.3% over the range of densities considered.

The same models, trained with synthetic data, were then applied to in-situ current measurements from the gold plated spherical probes on Swarm A. Since Swarm probes were never operated in fixed bias mode, currents collected by a single probe biased at 4 V and 5 V were used, when the probes were operated in sweep voltage mode. Using a single probe has the advantage that one does not need to account for the two different surface en-coatings that the Swarm probes have (gold plated vs titanium nitrid). Also, the different positions of both probes on the spacecraft can have a large effect and make a direct comparison of V_s between probes difficult. Using currents from a single probe, however, introduces uncertainty, as these two currents are not measured simultaneously, and therefore, plasma conditions can change along the satellite trajectory between the times at which the probe is at these two bias voltages. Considering the short delay (~ 80 ms) between $V_b = 4$ V and 5 V in sweep mode, the assumption of simultaneity is deemed acceptable. The electron density inferred with fixed bias probes as considered in this chapter, should be of interest in practice, as an independent means of inference in comparisons with measurements with other instruments. Also, on Swarm, the electron density in the background plasma can be inferred from Langmuir probes in normal sweep mode [188]. These two densities are generally not equal, however, and the method presented here, with quantified uncertainties, should prove relevant and useful in an effort to reconcile these density inferences. Inferences made with in-situ measured currents compared with parameters reported in the Swarm data portal show a general agreement qualitatively and quantitatively. Based on the assessments made with synthetic and in-situ data the best inferences for the satellite floating potential are obtained with a combination of

RBF and OML approximation. Unlike what was found with synthetic data, however, the inferences of $n/\sqrt{T_{eV}}$ with in-situ measurements made with direct RBF, combined OML-affine transformation, or with combined OML-RBF models were practically the same. Since no analytic approximation of the density can be made from only two currents collected by probes at two different bias voltages, only direct RBF inferences of the density were considered. In contrast to the relatively good agreement found between model inferences and synthetic data, the comparisons made here with inferred data reported in the Swarm data portal, show general qualitative consistency, but significant quantitative differences, with regression-inferred densities being lower than values reported on the data portal. This regression approach was also assessed against a possible bias, by training models using exclusively measured currents and plasma parameters from the Swarm data portal. Inferences made with these models were found to have skills comparable to those constructed and validated with synthetic data, thus showing that given accurate training data, the regression approach can be used to obtain accurate inferences. Based on these comparisons, it is estimated that inferences obtained with multivariate regressions can be made with uncertainties of order 0.2 to 0.25 V for the satellite potential, with relative uncertainties ranging from 0.06 to 0.30 for the density, and of order 0.1 for the ratio $n/\sqrt{T_{eV}}$. At this point it is not possible to ascertain to what extent these discrepancies between model inferred and reported results are caused by uncertainties in simulations from the selected regression techniques, or from uncertainties in inferred parameters reported on the Swarm data portal. Ideally, such an assessment would require more simulations with the creation of a larger solution library, possibly accounting for a more detailed satellite geometry, and more physical effects. It would also require validated accurate measurements made independently with other instruments, with quantified confidence intervals. In conclusion, the use of kinetic simulations, combined with adapted multivariate regression techniques, should be considered as a promising avenue to improve the accuracy of inferences in space and lab plasma, with quantified

confidence intervals, and it should elicit interest and contributions from both modelers and experimentalists.

Chapter 4

Segmented Spherical Langmuir Probes

This chapter is based on a manuscript titled “A new technique to infer plasma density and flow velocity, and satellite potential from ion currents collected by a segmented Langmuir probe” by Akinola Olowookere and Richard Marchand. At the time of this writing, the manuscript is accepted and in preparation for publication in the IEEE Transactions on Plasma Science. With this project, I consider the use of spherical segmented Langmuir probes as a means to measure ionospheric plasma transverse velocity using kinetic simulations and regression methods. The approach is later extended to determine the plasma density and satellite potential. The density model is applied to Proba-2 segmented Langmuir probe in-situ measurements, and model inferences are compared to reported densities from the Proba-2 data portal.

4.1 Introduction

Several studies are being made to better monitor and understand the many physical properties of space plasma using a variety of instruments. In particular, different flow meters have been used on satellites to determine direction of the plasma flow along satellite trajectories [189, 190]. For example, IAP was flown on DEMETER to measure the direction of ion bulk velocity, in addition to the energy distribution and plasma density [190, 191]. Similarly, ion drift velocities can be determined with the

thermal ion imager (TII) on Swarm [149]. In addition, VEIS on the WIND satellite and the flow meter on Dynamics Explorer B have been used to study plasma flow directions [192–194]. Mach probes have also been used to measure the plasma flow speed relative to the sound speed, or the Mach number. There are several types of Mach probes such as the parallel Mach probe which consist of two directional probes separated by an insulator [195]. Using the upstream and downstream ion saturation currents of the probes, the Mach number can be determined, from which the velocity is obtained using different theoretical approximations [195–198]. Other types of Mach probes include the rotating Mach probe, the Gundestrup probe, and the vico-Mach probe, and their detailed operation can be found in the literature [195, 196, 199]. Another multi-purpose Langmuir probe used to measure plasma velocities, is the spherical segmented Langmuir probe, first flown on DEMETER [200]. The probe is designed to leverage the angular anisotropy of the current collected by each of its six segments to determine the plasma bulk velocity [200]. This type of Langmuir probe was later implemented on the European Space Agency micro satellite, Proba-2. Each of the two spherical segmented Langmuir probes on Proba-2 has seven equi-potential segments, or spherical caps and a guard holding them together [66]. Numerical modeling of the spherical segmented Langmuir probe has also been done using particle-in-cell simulations to investigate the variations in the collected currents from each of the segments; the results obtained are similar to what is reported for DEMETER [201, 202].

In the following, kinetic simulations and regression techniques are applied to construct inference models for measurements made with a segmented probe. The goals are i) to characterize the response of each segment on the probe to different plasma velocities and environmental conditions using computer simulations, ii) to construct regression models to infer plasma densities, transverse flow velocities, and satellite potentials, and iii) to assess the skill of the inference models. Two geometries are considered, the first one is for a spherical probe with 20 segments at the centers

of the 20 triangles of a regular icosahedron. This idealized geometry is chosen for its symmetry, and it is used to make a first assessment of the regression method. The second geometry represents the actual Proba-2 spherical segmented probe. In both cases, the equipotential posts to which the probes are attached are included in the simulations. Synthetic data sets are constructed for both geometries, a subset of which is used to train models, which can then be assessed by applying them to make inferences with a distinct subset used as validation set. The models trained with synthetic data are then applied to actual in-situ current measurements obtained from the Proba-2 data portal, for the segmented probes. The model inferences are then compared with data available from the Proba-2 portal. In the remainder of this chapter, the approach used to create the two synthetic data sets is explained. The two machine learning techniques used to train the models are presented in Section 4.2, while the inference models constructed using the two synthetic data sets and the validation results are presented in Section 4.3. The trained models are applied to in-situ measurements in Section 4.4, and a summary of the findings is presented in Section 4.5.

4.2 Methodology

The first, idealised segmented Langmuir probe used in the simulations is constructed on a regular icosahedron with 20 triangular faces, 12 vertices, and 30 edges. The coordinates of the center of each triangular face are used as the centers of the 20 caps (segments) on the probe. The advantage in this idealised geometry is to leverage the five-fold symmetry of the structure and minimize the number of required simulations. Fig. 4.1 illustrates an icosahedron and the segmented probe used in the simulations, which consists of twenty 5-mm-radius segments on a 2-cm-radius conducting guard, and the 1.5-cm-long, 6-mm-radius cylindrical post holding them. The dimensions of the segments, guard and the cylindrical post for the idealised geometry is the same as that of the Proba-2 segmented Langmuir probes. In the simulations, the spherical

guard, the twenty segments, and the cylindrical post are assumed to be equipotential, and the currents collected by these independent components are calculated separately. It is assumed that the probe is held by a boom sufficiently far from other satellite components in the ram direction, so that the probe is not affected by any other component on the satellite. The segments on the probe are assembled into 4 groups of 5 segments at angles 37.38° , 79.19° , 100.81° , and 142.62° relative to the axis of the post, which is assumed to be oriented in the ram direction. The response of the probe to different plasma conditions is simulated with PTetra, a three-dimensional particle-in-cell (PIC) code, and the simulation domain is discretized with an adaptive unstructured tetrahedral mesh [203]. Electrons and ions are treated kinetically, and the fields and particle trajectories are calculated self-consistently at every time step [77, 144, 145, 201]. The plasma parameters considered in the simulations are obtained from the International Reference Ionosphere (IRI) model for conditions encountered by satellites in low Earth orbit (LEO) at latitudes in the range -65° to 65° , different longitudes, for altitudes ranging from 500 to 730 km, different seasons, and times of the day. Plasma densities considered vary from $9 \times 10^{10} \text{ m}^{-3}$ to $2 \times 10^{12} \text{ m}^{-3}$, electron temperatures from 0.0591 eV to 0.2464 eV, ion temperatures from 0.0591 eV to 0.2268 eV, and effective ion masses, from 5 amu to 13 amu. A summary of the parameters used in the simulation is presented in Table 4.1.

4.2.1 Construction of the synthetic data set

The data set used in this chapter is made from the simulation of an isolated spherical segmented Langmuir probe shown in Fig 4.1. The probe bias voltage is assumed to be swept or varied in time from -5 V to -1 V with respect to the background plasma. Plasmas with multiple ion species are considered in the simulations, as presented in Table 4.1. In the simulations, plasma is assumed to flow directly from the ram direction, and at an angle of 18° from the ram direction, with speeds ranging from 7000 to 8000 m/s. Two sets of data are created; the first one corresponding to a hypothetical

Table 4.1: Simulation parameters used in the construction of the solution library.

n	T_e	T_i	m_{eff}	n_{O^+}	n_{H^+}	n_{He^+}	n_{N^+}
10^{10} m^{-3}	eV	eV	amu	%	%	%	%
0.911	0.2268	0.2268	5.21	76.80	13.60	0.60	9.00
1.160	0.1632	0.1203	8.23	92.97	6.19	0.53	0.31
2.540	0.1717	0.1123	12.09	97.58	2.09	0.32	0.00
4.579	0.1354	0.1202	9.29	94.68	4.72	0.48	0.12
4.572	0.1692	0.1102	12.80	98.02	1.61	0.27	0.09
4.840	0.0591	0.0591	16.00	100.0	0.00	0.00	0.00
6.446	0.07218	0.07218	6.27	86.39	10.20	0.62	2.79
6.476	0.2464	0.1089	15.93	99.73	0.00	0.15	0.12
8.169	0.09805	0.09805	11.01	96.57	2.95	0.37	0.11
12.04	0.2144	0.09356	15.83	94.73	0.00	0.11	5.16
15.11	0.1791	0.1006	15.88	95.59	0.00	0.05	4.36
18.73	0.2207	0.09438	12.62	97.87	1.76	0.11	0.27
22.90	0.1515	0.1003	15.86	95.07	0.00	0.06	4.88
44.50	0.0894	0.0766	15.86	94.65	0.00	0.05	5.30
84.19	0.09467	0.09467	14.19	94.79	0.78	0.13	4.29
106.0	0.0935	0.0869	15.89	95.07	0.00	0.00	4.93
112.0	0.0983	0.0868	15.89	95.07	0.00	0.00	4.93

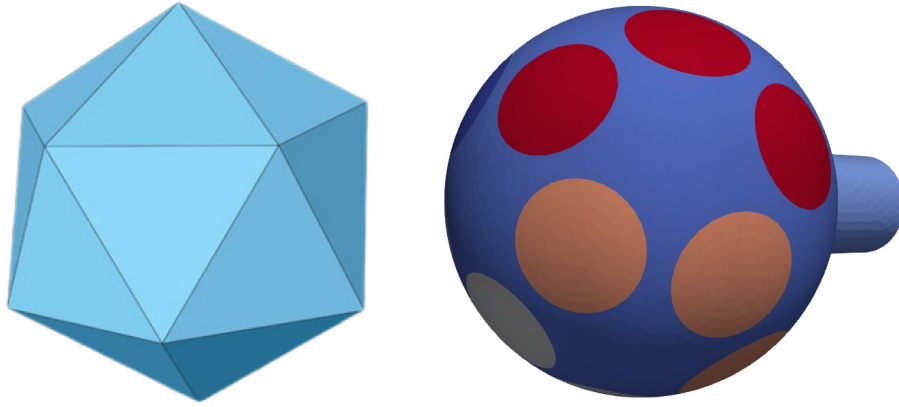


Figure 4.1: Illustration of the geometry of the segmented probe used in the simulation (right) and an icosahedron (left).

satellite at the same potential as the background plasma, and the second corresponding to satellite potentials varying from -6 to -3 V relative to the background plasma. All simulations are carried out to steady state, at which time, the currents collected by each segment, the guard, and the cylindrical post are computed. Test particle backtracking simulations are then used to calculate the particle distribution functions at selected points on the sphere by applying Liouville's theorem in a collisionless plasma [85]. The electric fields used in the calculation of particle trajectories are obtained from the PIC simulations in which they are calculated self-consistently. The particle fluxes and current densities are then determined numerically from moments of the distribution functions discretised on an adaptive octree velocity grid [83, 204, 205]. Particle distribution functions are calculated on the probe spherical surface along each of four meridians, 90° apart longitudinally. The selected points are located at different co-latitude angles θ relative to the ram direction in the range $0^\circ \leq \theta \leq 130^\circ$, with each meridian having different values of θ as listed in Table 4.2. The current densities are then fitted as a function of θ with a sum of cosine functions as

$$I(\theta) = \sum_{k=0}^N a_k \cos(k\theta), \quad (4.1)$$

for each set of plasma parameters in Table 4.1. In Eq. 4.1, a_k are fitting coefficients, and N is the number of fitting coefficients. The fitting coefficients are obtained from a straightforward least square fit to the computed current densities. In practice, the value $N = 6$ is found to provide excellent accuracy, with maximum relative errors not exceeding 1.2%. The fits are then used to calculate the currents collected by each segment on the probe for arbitrary plasma flow directions in the range $[0^\circ, 15^\circ]$ relative to the ram direction. Currents collected by segments are obtained by using the fit to calculate the current density at the centre of the triangles defining each segment. Note that with the unstructured tetrahedral mesh, segments are delimited by triangles corresponding to faces of tetrahedra adjacent to the segments. Owing to the symmetry of the probe, the angle θ in the fit is simply the angle between the direction of the incoming plasma flow and the radial position of the triangle centre in a given segment. The current collected by each segment is obtained by adding the current densities times the areas of the triangles in each segment. The performance of the fits is accessed by comparing currents calculated directly from PIC simulations, with corresponding currents calculated using the fits as described above. The accuracy of the calculated currents is found to be within 3% in all cases considered.

4.2.2 Machine Learning Approach

Depending on the nature of problem, there are different methods used in machine learning to train inference models. In this chapter, two approaches based on i) Radial Basis Functions, and ii) deep learning neural networks are used. These are briefly explained below.

Radial Basis Functions (RBF)

RBF is a relatively simple but efficient regression technique to construct inference models for complex relations between output and input variables. It has been widely

Table 4.2: List of angles θ relative to the ram direction of points considered in each meridian.

First Meridian	Second Meridian	Third Meridian	Fourth Meridian
0.0°	3.75°	7.5°	11.25°
15.0°	18.75°	22.5°	26.25°
30.0°	33.75°	37.5°	41.25°
45.0°	48.75°	52.5°	56.25°
60.0°	63.75°	67.5°	71.25°
75.0°	78.75°	82.5°	86.25°
90.0°	93.75°	97.5°	101.25°
105.0°	108.75°	112.5°	116.25°
120.0°	123.75°	127.5°	130.0°

used for interpolating scattered data in a multi-dimensional space [206–208]. The technique consists of inferring a dependent variable Y at position \bar{X} in an n -tuple space of independent variables, with a linear superposition of a function of the distance between \bar{X} and selected reference points or centers \bar{X}_i , as in Eq. 2.8. In this chapter, \bar{X} is a tuple consisting of currents collected by the segments on the probe, and Y represents the plasma parameter of interest to be inferred, which can also be a tuple or a scalar. There are different methods used to select a set of centers. One way is by carrying out an extensive search for the set of N_p centers which minimizes the cost function among all possible combinations of N_p centers chosen from \mathcal{N} nodes in the entire data set as explained in Section 2.3.2 in Chapter 2. The computation time of going through all the possible combinations can be prohibitively long if the model is trained using a large data set and the time increases rapidly with an increase in the number of N_p centers. The strategy used in this chapter in selecting N_p centers consists of successively and randomly selecting M small subsets of nodes from the full training set, each containing \mathcal{M} nodes (\mathcal{M} being the batch size). For the first batch,

all the possible combinations of N_p centers among the \mathcal{M} nodes are considered and the set of centers that minimizes the cost function, calculated on the full training set, is temporarily kept as optimal. These N_p nodes are then kept in the next batch, in which $\mathcal{M} - N_p$ nodes are randomly selected from the full \mathcal{N} training set. This random selection must of course be made so as not to duplicate the previously found optimal N_p nodes. These steps continue until the M number of batches have been considered, and the final set of centers that minimizes the cost function is selected for the final model. This approach is numerically much more efficient than the straightforward extensive search, while producing models with comparable accuracy.

Neural Networks (NN)

Neural Networks have become a useful tool in modern scientific research, in space physics, as well as in many areas of science, medicine, and other fields [95, 209–211]. In this chapter, a multi-layer perceptron (MLP) network is used. MLP is one of the commonly used network architectures in training neural network models [212]. The network is arranged in a layered feed-forward topology as shown in Fig. 4.2. Weighted sums of the input data from the input layer are passed through a nonlinear activation function which produces an output which is then passed to the next layer as the input data. This continues until the final output is produced in the output layer. For illustration, given nodes j in layer i with values z_{ij} , the nodes in the next layer $i + 1$ take in the output of each node in the previous layer, the value is assigned to $z_{i+1,k}$ as in

$$z_{i+1,k} = \sum_{j=1}^{n_i} w_{i,j,k} f(z_{i,j} + b_{i,j}), \quad (4.2)$$

where n_i is the number of nodes in layer i , $w_{i,j,k}$ are weights, and $b_{i,j}$ are bias terms. The weights and bias terms are optimized using a back-propagation learning scheme using algorithms like gradient descent, ADAgrad, RMSprop, or ADAM [213, 214]. Each node in the input layer is assigned a current from one of the segments, and all the models are trained with TensorFlow [215]. The bias terms in Eq. 4.2 are all set to

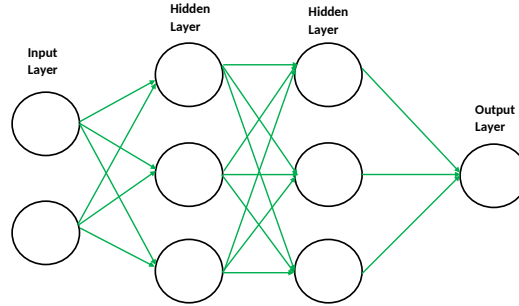


Figure 4.2: Illustration of a feedforward neural network.

zero when training the model because they are found to make no significant difference in the outcome, and the activation function used is the rectified linear unit (ReLU); $f(z) = ReLU(z) = \max\{0, z\}$, which performs a nonlinear combination of all the input data. Another key component in neural networks is the cost function described in Section 2.3.2, which measures the discrepancy between inference and known data.

4.3 Construction of inference models

Inference models are constructed using synthetic data sets generated for the idealised segmented probe and the Proba-2 probe. Only the 10 segments on the ram side are considered in the regression. The models' skills are then assessed in each case by comparing inferences to known values used as input in the simulations. Comparisons between inferences and data from the validation sets are presented below for the two geometries considered.

4.3.1 Idealised probe geometry

As a first step, the currents collected by the 10 segments located on the side of the probe facing the ram direction are calculated as described in Section 4.2.1. For simplicity, the satellite is initially assumed to be at the plasma potential so as to concentrate on the flow velocity, without having the extra complication coming from different floating potentials. A synthetic data set consisting of 24000 nodes is created,

each node consisting of a 10-tuple of currents for each of the 10 segments, followed by the physical parameters to be inferred; that is, the transverse velocity which ranges from -1000 m/s to 1000 m/s, and the densities as in Appendix A.1. The resulting synthetic data is randomly split into two disjoint subsets, one being used to train inference models, and the other for assessing the accuracy of the inferences. The training set consists of 14500 randomly selected nodes from the solution library, while the validation set consists of the remaining 9500 nodes. Using the two regression techniques explained in Section 4.2.2, models are trained to infer the electron density n_e , and the plasma transverse velocity. Each model is then assessed for accuracy by comparing its inferences with known values in the validation set.

Density model

Both the neural network and RBF models are used to infer the plasma density. The neural network consists of an input layer of 10 nodes for each of the 10 currents, 2 hidden layers of 8 and 5 nodes respectively, and a single output node for the density. The cost function used is the mean absolute relative error (MARE) given by

$$\text{MARE} = \frac{1}{n} \sum_{j=1}^n \left| \frac{Y_{dt} - Y_{inf}}{Y_{inf}} \right|, \quad (4.3)$$

where n is the number of entries in the training data set, Y_{dt} is the data value and Y_{inf} is the inferred value. The cost function is minimized with the Adam algorithm, which is an adaptive optimization algorithm implemented in Tensor Flow [216]. This algorithm was chosen among other minimization options because of its optimal performance in these problems. The correlation plot in Fig. 4.3a. shows a comparison between neural network inferences and data from the validation set. The model skill is assessed with the MRE, the RMSrE, and the Pearson correlation coefficient (R). Model inferences are in excellent qualitative and quantitative agreement with validation values, with a MRE not exceeding 11% and RMSrE of 3.1%. In the RBF model, 50 batches, each consisting of 90 randomly selected nodes from the training set are

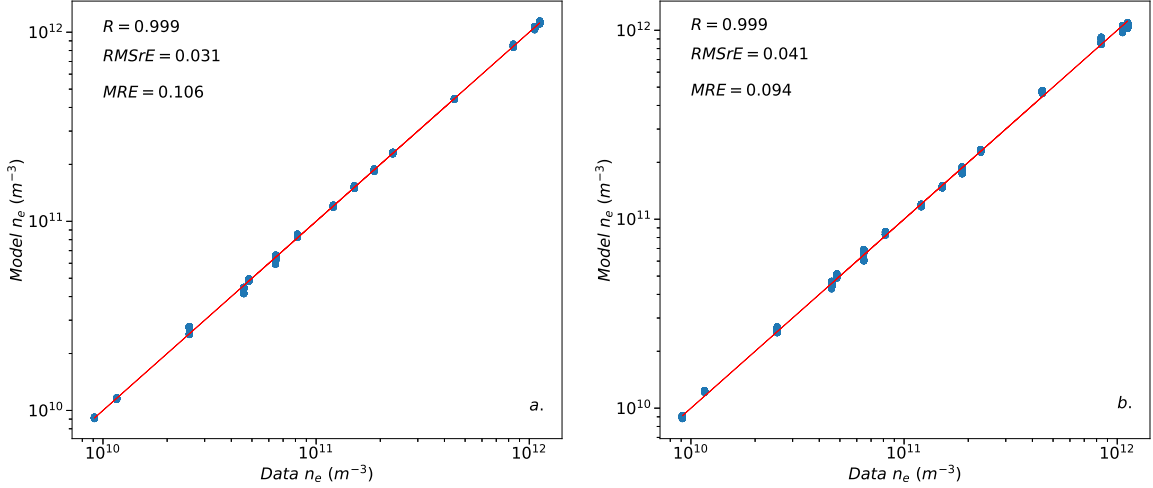


Figure 4.3: Comparison between inferred densities using (a) neural network, (b) RBF with six centers, and actual densities in the idealised probe validation data set. The straight line corresponds to a perfect agreement between the two densities.

used. Six (6) center points are used in the model, as this number is found to provide a good balance between training and validation, while avoiding overfitting. The cost function used to construct the RBF model is the MRE given in Eq. 1.19. Several interpolating functions were tested, but the best one that minimised the maximum relative error for the density model is $G = |I - I_j|^{1.8}$. Figure 4.3b shows a correlation plot of the inferred density as a function of the actual densities from the validation set. The skill of the RBF model is assessed using the same metrics as for the NN model and it shows a comparable inference accuracy between the two models with the RBF models having lower MRE in contrast to the RMSrE which is higher in RBF than the neural network model. The MRE is minimised as the cost function when training the RBF model, and this accounts for its lower value in the RBF model compared to the NN model. The correlation plots for both methods also show that model predictions closely follow the ideal correlation line, with a strong affinity as measured with the Pearson correlation coefficients which are close to unity in both cases.

Transverse velocity inferences

Here, only the neural network model is applied to infer transverse velocities, because in this case, RBF was found to produce lower quality results. The neural network used has 5 layers, comprised of the input layer with 10 nodes, 3 hidden layers with 8, 6, and 4 nodes respectively, and an output layer with 2 nodes for the two components of the transverse velocities. The cost function used is the mean square error defined as

$$\text{MSE} = \frac{1}{n} \sum_{j=1}^n (|Y_{dt} - Y_{inf}|)^2. \quad (4.4)$$

Figure 4.4 shows a two dimensional scatter plot of the components of the transverse velocities, with the colour bar showing the absolute errors in the model inferences. The plot is dominated by blue points, with very few red and light red points which indicates that most of the errors in the model inferences fall below 100 m/s. The maximum absolute error in the inferences is 193.54 m/s but almost 98% of the values inferred have an absolute error less than 100 m/s as seen in the histogram in Fig. 4.5, showing the distribution of errors. The mean absolute error is 28.93 m/s and the root mean square error is 45.41 m/s, which corresponds to 2.3% relative to the range of speeds, [-1000 m/s, 1000 m/s] considered in the simulation. The values of these errors show a good quantitative agreement between model inferences and the known transverse velocities used as input in the simulation. The error values are consistent with the range of velocity accuracy estimate for Swarm TII of 100 - 200 m/s [149].

4.3.2 Proba-2 probe geometry

The synthetic data used in this part are generated for the segmented Langmuir probe A (SLPA) geometry, as one of the Proba-2 dual segmented Langmuir probes (DSLPA). DSLPA is part of the scientific payload of the European Space Agency (ESA) micro satellite Proba-2, which was launched November 2, 2009 [217]. It consists of two identical segmented Langmuir probes, SLPA and SLPB, with each having eight

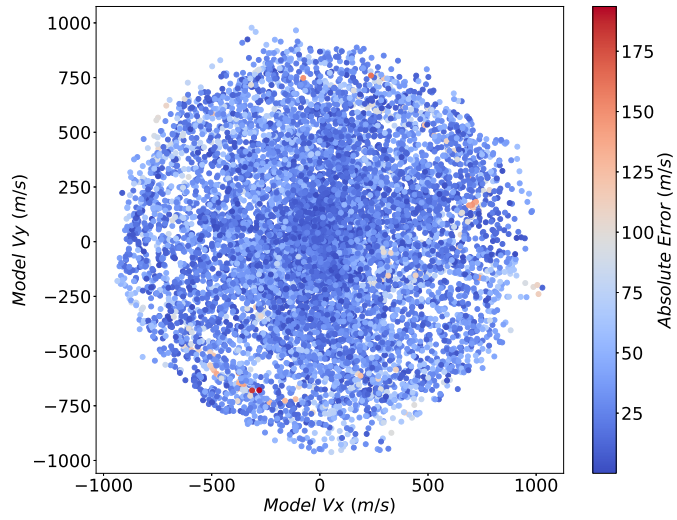


Figure 4.4: Inferred transverse velocities in the range of -1000 m/s to 1000 m/s using the neural network model for the idealised probe. The colour scale shows the absolute errors in the velocity model inference.

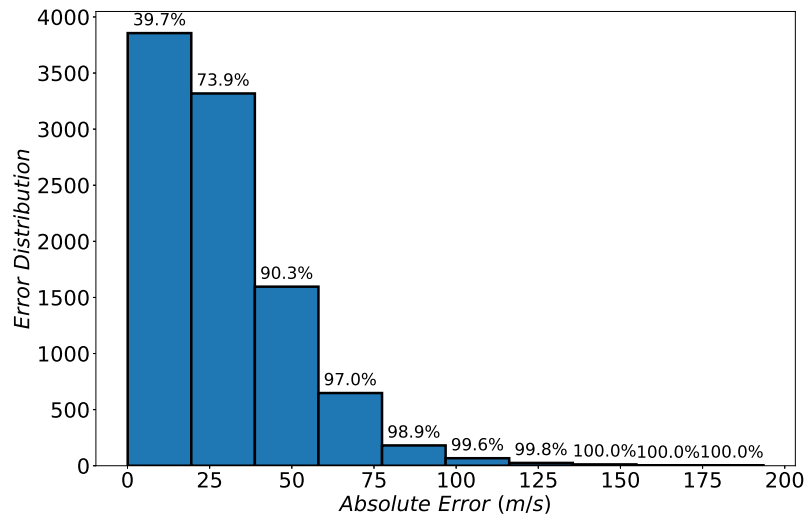


Figure 4.5: Histogram showing the distribution of the absolute error in the velocity inference model for the idealised probe.

equipotential independent collectors electrically insulated from each other. The collectors consist of spherical guard electrode supporting seven circular caps, or segments positioned at different locations. In the Proba-2 data portal, the ram velocity of the satellite is stated to be in the $-Y$ direction in the spacecraft body reference frame (BOF), and thus the plasma flow velocity in the spacecraft frame is assumed to be in the $+Y$ direction. The segments on the SLPA are positioned relative to the segments frame of reference (SEG), which is different from the spacecraft BOF. The BOF can be transformed to the SEG by first performing a counterclockwise rotation around the BOF x-axis by 40° , followed by another counterclockwise rotation of 60° around the transformed z-axis. This transformation is necessary because the fit in Eq. 4.1 is done relative to a system in which the z axis coincides with the cylindrical post axis. After the transformation, the trigonometric fit is used to determine the current density at the center of the triangles defining each of the seven segments on the probe, which makes it possible to integrate, and determine the current collected by each segment as described in Section 4.2.1. The currents are calculated by assuming that the probe is biased at fixed voltages relative to the satellite. The advantage of considering a fixed bias probe is that measurements can be made with a higher temporal, and owing to the large satellite speed, higher spatial resolution. The satellite potentials assumed in the synthetic data set range from -6 V to -3 V, which falls within the range of potentials reported on the Proba-2 SLPA portal, and different transverse speeds in the range $[-1000$ m/s, 1000 m/s] are also considered. A total of 8500 nodes are generated in the solution library; each entry consisting of the currents calculated for each segment, followed by the densities, the transverse velocities, and the satellite potentials. Here again, the data set is randomly divided into a set consisting of 5950 nodes used to train the models, and a distinct set containing the remaining 2550 nodes used for validation. The models are trained using currents for all segments excluding only segment 6. The choice of the six segments among the seven on the sphere is dictated by the orientation of the probe on Proba-2 (Fig. 4.6) and the limited interval in angle

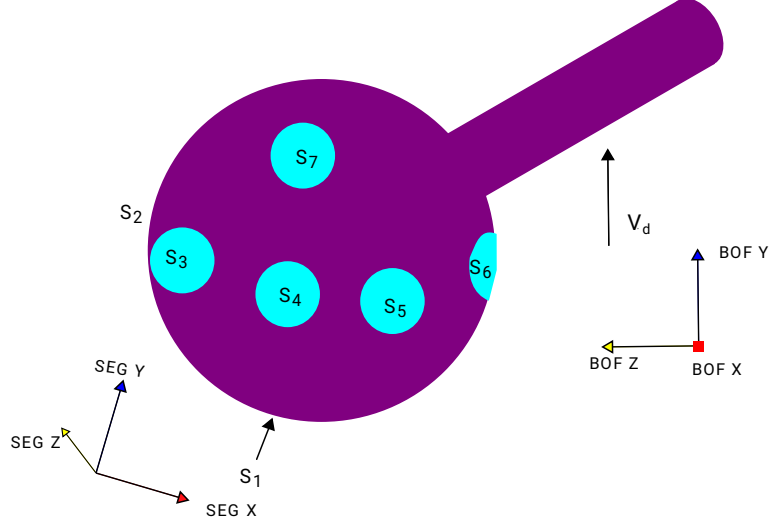


Figure 4.6: Illustration of the position of the segments relative to the direction of plasma flow.

($0^\circ \leq \theta \leq 130^\circ$) for the fitted current densities, relative to the ram direction. With currents from the probe, the independent variables then consist of twelve-tuples; six from a probe biased at 1 V and six for a probe biased at 2 V.

Density model assessment with synthetic data

The density inference models are constructed using a neural network and RBF. The neural network consists of 5 layers, which comprise the input layer with 12 nodes for the currents collected by the selected segments on the two probes (6 segments on each probe), at the two bias voltages, three hidden layers with 10, 7, 3 nodes in layers 2, 3, and 4 respectively, and an output layer with a single node. The model is trained using the mean absolute relative error given in Eq. 4.3 as a cost function. This is minimised to achieve an optimal model, using the same activation function as in Section 4.3.1. In the RBF model, 6 centers are used, the interpolating function chosen is again $G = |I - I_j|^{1.8}$, and the model is constructed by minimizing the maximum relative error. Figure 4.7 shows the correlation plots obtained when comparing model inferences when the trained models are applied to the validation set. Both techniques show excellent agreement with known data, with the neural

network slightly outperforming RBF with a maximum relative error (MRE) of 7.1% and root mean square relative error (RMSrE) of 2.1% compared to MRE of 9.6% and RMSrE of 3.4% for RBF. The points on the plot for both methods closely follow the perfect correlation line, but the vertical spread in the RBF model is slightly larger than that obtained with the neural network. The Pearson correlation coefficients R indicate the two models show an excellent affinity with known density values from the validation set.

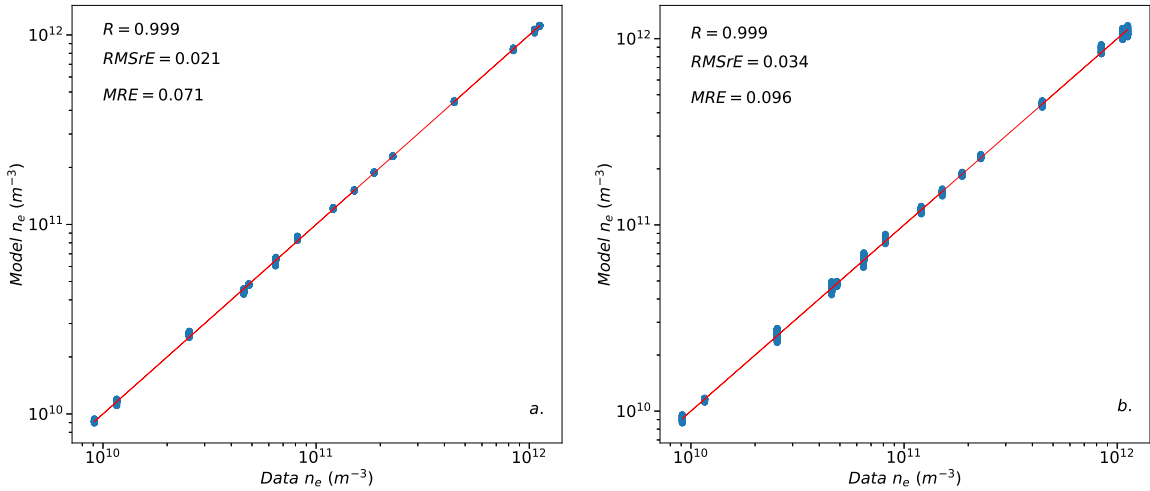


Figure 4.7: Inferred densities against validation data set densities for the Proba-2 synthetic data. Neural network inferences are shown on the left, and RBF inferred densities using 6 centers, on the right. The line corresponds to a perfect agreement between the two densities.

Satellite potential model assessment with synthetic data

Here, only results obtained with a neural network to infer the satellite potential are considered, because its inference skills are significantly better than those found with RBF. The neural network model has a similar structure to the one used in training the density model presented in Section 4.3.2. In this case, however, instead of using the MARE given in Eq. 4.3 as the cost function, the MSE in Eq. 4.4 is used, with which the best inferences are achieved. The skill of the trained model is assessed using different metrics when applied to the validation data set. The Pearson correlation

coefficient between the inferred satellite potential and the actual satellite potential is 0.995, which indicates a good affinity. A correlation plot between these values is shown in Fig. 4.8, with the calculated values of the MaxAE, the RMSE and the MeanAE. From the plot, a slight extrapolation in the model inferences is noticed, as a small fraction of the points fall outside the range in the data used to train the model. Quantitatively, the overall performance of the model is excellent, with a MeanAE of 0.063 V which corresponds to 2.1% discrepancy relative to the range of satellite potential in the data set.

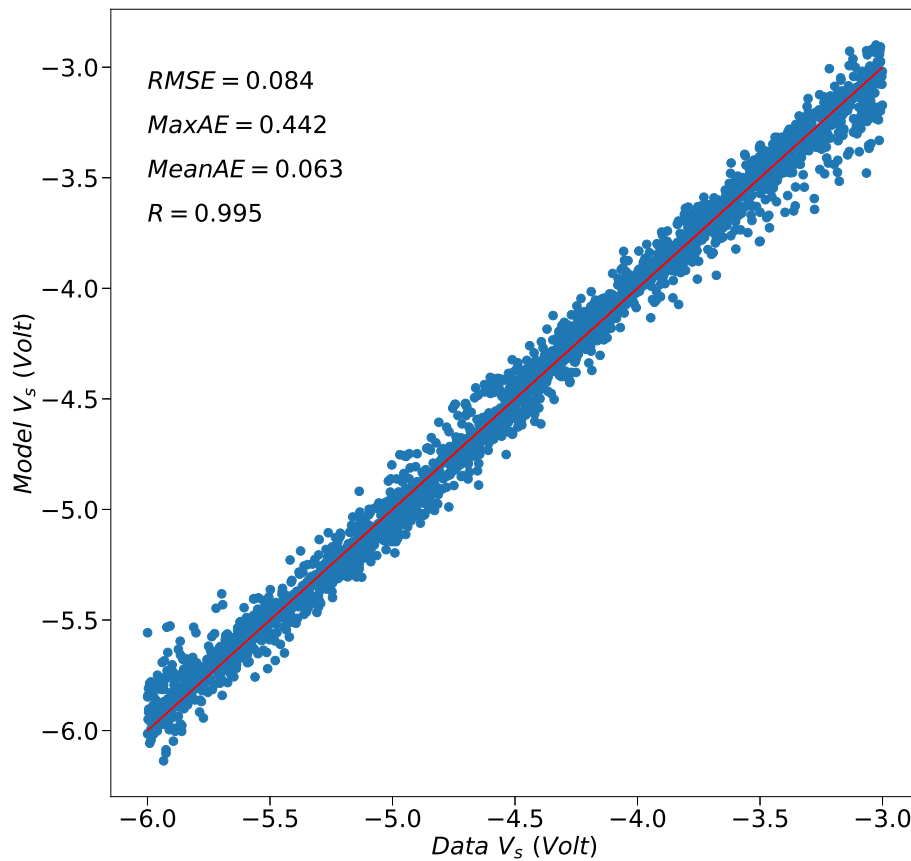


Figure 4.8: Comparison between satellite potentials inferred using the neural network model, and actual potentials in the synthetic data set constructed with the Proba-2 geometry. The line corresponds to a perfect agreement between the two potentials.

Transverse velocity model assessment with synthetic data

Here also, only the neural network approach is used to construct a model for the transverse velocity, because it produces appreciably better model inferences than the RBF. In this case, the network has 5 layers, with the input layer having 12 nodes and the three hidden layers consisting of 15, 9, and 6 nodes respectively, while the output layer consists of 2 nodes, for the two components of the transverse velocity. The model is obtained by minimising the mean square error defined in Eq. 4.4. Fig. 4.9 is a scatter plot of the components of the transverse velocities, with the colour bar showing the absolute errors in the model inferences. In the figure, most points are blue, indicating that the majority of the absolute errors in the inferences fall below the 100 m/s mark. This observation is confirmed with the histogram in Fig. 4.10, showing the distribution of inference errors when applying the model to the validation set. The histogram shows that nearly 99% of the inferences are made with absolute errors not exceeding 100 m/s. The skill of the model is further quantified with the mean absolute error and the root mean square error, with values 22.54 m/s and 39.53 m/s corresponding respectively to errors of 1.12% and 1.98% relative to the range [-1000 m/s, 1000 m/s] of transverse velocities in the data set. These metric scores indicate an excellent model inference skill.

4.4 Application to Proba-2 in-situ measurements

In this section, the density model constructed in Section 4.3.2 are applied to the Proba-2 segmented Langmuir probe A (SLPA) measurements reported on the Proba-2 portal [218]. The currents used are obtained from the measured IV characteristics when the probe is operated in sweep mode between -5 V and 5 V. In addition to the probe's IV characteristics, the portal also reports densities and satellite potentials inferred from each segment separately, as well as from the spherical guard. One point worth noting, is that densities and satellite potentials reported for these probe com-

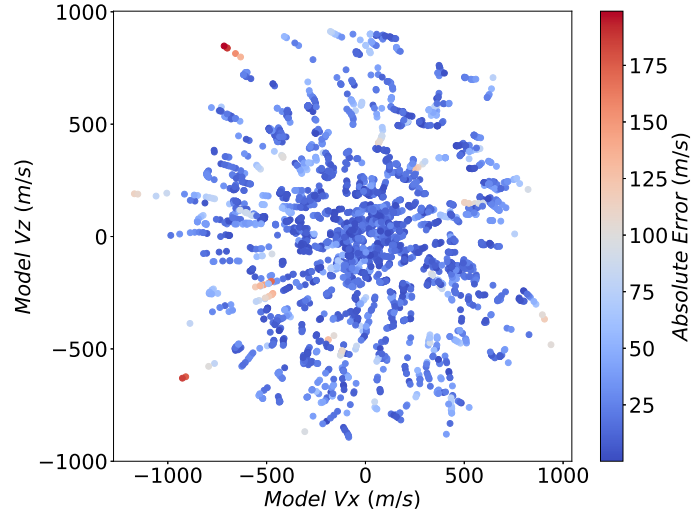


Figure 4.9: Inferred transverse velocities in the range of -1000 m/s to 1000 m/s using the neural network model, and actual velocities in the synthetic data set constructed with the Proba-2 geometry. The colour scale shows the absolute errors in the velocity model inference.

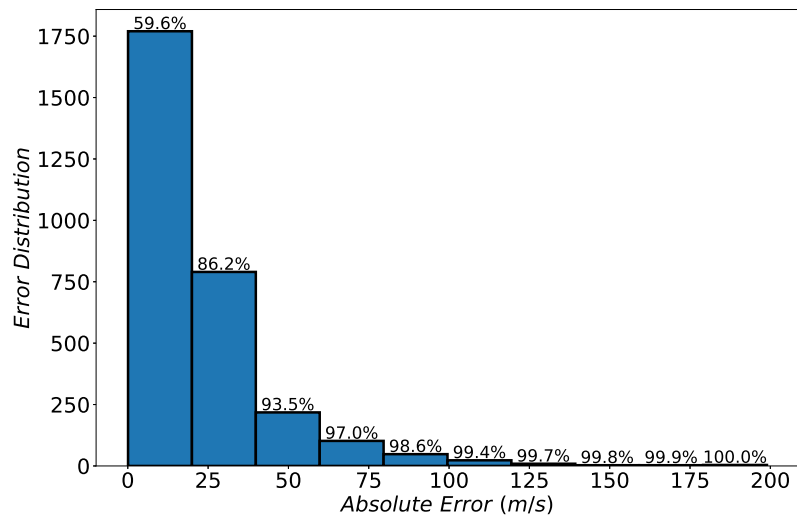


Figure 4.10: Histogram of the distribution of the absolute errors in the velocity inference model when applied to the synthetic data set constructed with the Proba-2 geometry.

ponents are generally all different from one another, and to the author's knowledge, the method used to infer these reported values is not documented. Here, the same models presented in Section 4.3.2 are used. These models are trained using synthetic

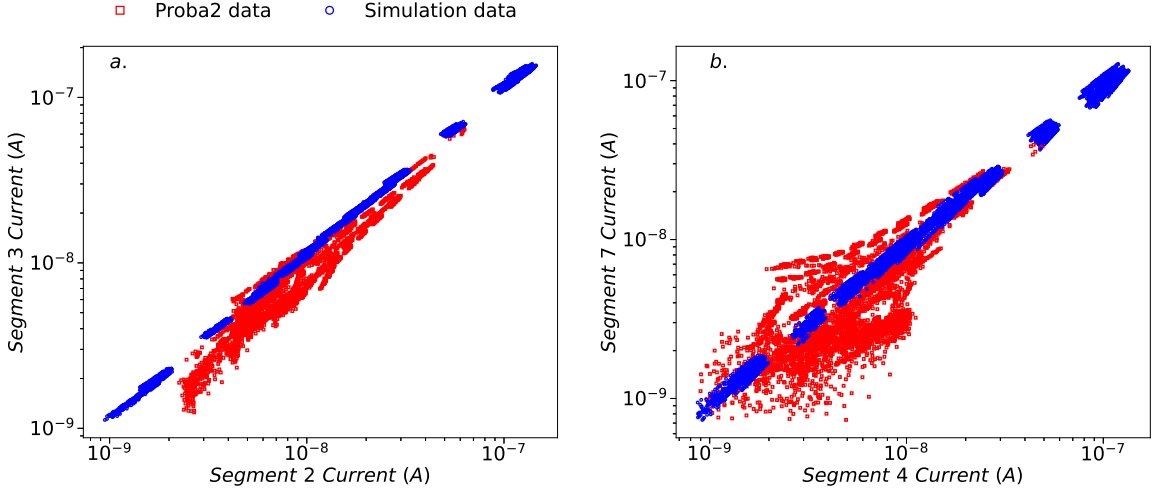


Figure 4.11: Correlation plots for currents collected between pairs of currents collected by segments 2 and 3, and segments 4 and 7. The blue circles are taken from the synthetic data set, while the red squares are from Proba-2 measurements.

data generated assuming probe biased at fixed voltages of 1 V and 2 V. The assumption of fixed bias probes is of course different from the sweep mode actually used with these probes. The measured currents needed in the model are nonetheless obtained by fitting each segment characteristic in the range -1.5 to 2.5 V, and using these fits to interpolate the current collected at 1, and 2 V bias voltages. As a first test, and in order to assess whether the currents found in the simulations are of relevance to measured currents, Fig. 4.11 shows samples of correlation plots between simulated and measured currents collected by segments 2 and 3 (panel a) and segments 4 and 7 (panel b). The red squares are from Proba-2 SLPA measurements and the blue circles are from simulations. This comparison is also useful in order to eliminate cases corresponding to currents outside the range of currents considered in the synthetic data set. The figure shows an overlap between the range of the in-situ currents and the synthetic data currents, with the synthetic data having a wider range of currents.

The neural network model is then applied to infer the plasma density using measured currents as the input. The neural network model is used here rather than RBF,

because it proved to be more accurate based on the validations made with synthetic data. The average values for each set of densities reported for the six segments used in the model and their respective standard deviations are calculated. Using these two values, a confidence interval delimited by an upper and lower boundary for each density is determined by adding and subtracting the standard deviations to the average. A comparison between the densities inferred using the model with the reported guard densities on Proba-2 portal, and the calculated upper and lower boundary densities is shown in Fig. 4.12. The comparison shows general qualitative agreement between the inferred densities, and those reported in the Proba-2 portal, albeit with reported densities being larger than neural network inferred densities by more than 100%. The inferred densities are more consistent with reported guard densities, than with those calculated from the segments, and both are generally below the confidence interval estimated from densities reported for the segments. The gaps or jumps in the horizontal axis scale in the plots are due to the removal of data outside the range of simulated currents used to construct the model. Correlation plots between the inferred densities and in-situ reported densities are shown in Fig. 4.13, for each of the segments and the guard when using the neural network model, with their respective RMSrE and MRE skill metrics. In general, the inferences from the neural network model are closer to in-situ measurements than those obtained with RBF model, as apparent with the similarity metrics listed in Table 4.3.

Lastly, the satellite potential model and the transverse velocity model were also applied to the in-situ measurement, but the inferences in these cases are far beyond the range of satellite potentials and velocities considered in training the models which indicate that these models in their present form, are not applicable. A probable cause for this shortcoming is the proximity of the probes to the solar panels on Proba-2, which is not accounted for in the simulations.

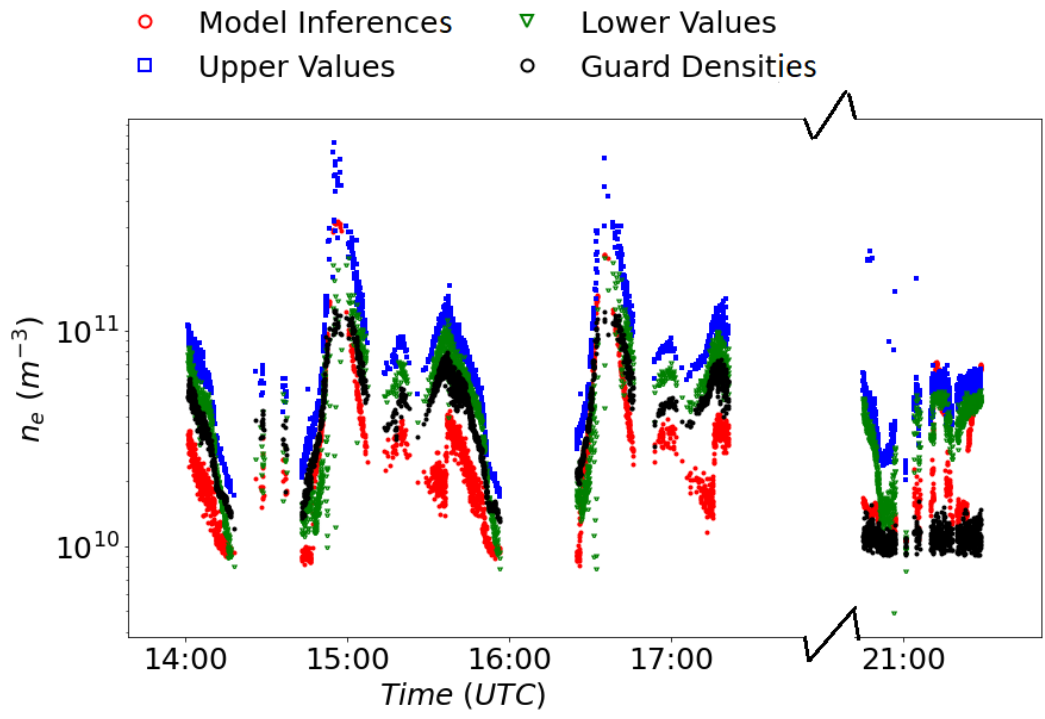


Figure 4.12: Comparison between densities inferred using the neural network model (red circles), with those reported for the guard (black circles), the upper (blue squares), and lower (green inverted triangles) density boundaries of the confidence interval. The confidence interval is calculated from the averages and standard deviations of densities reported on the Proba-2 portal for the six segments considered. The gaps in the comparison correspond to currents outside the range over which the models were trained.

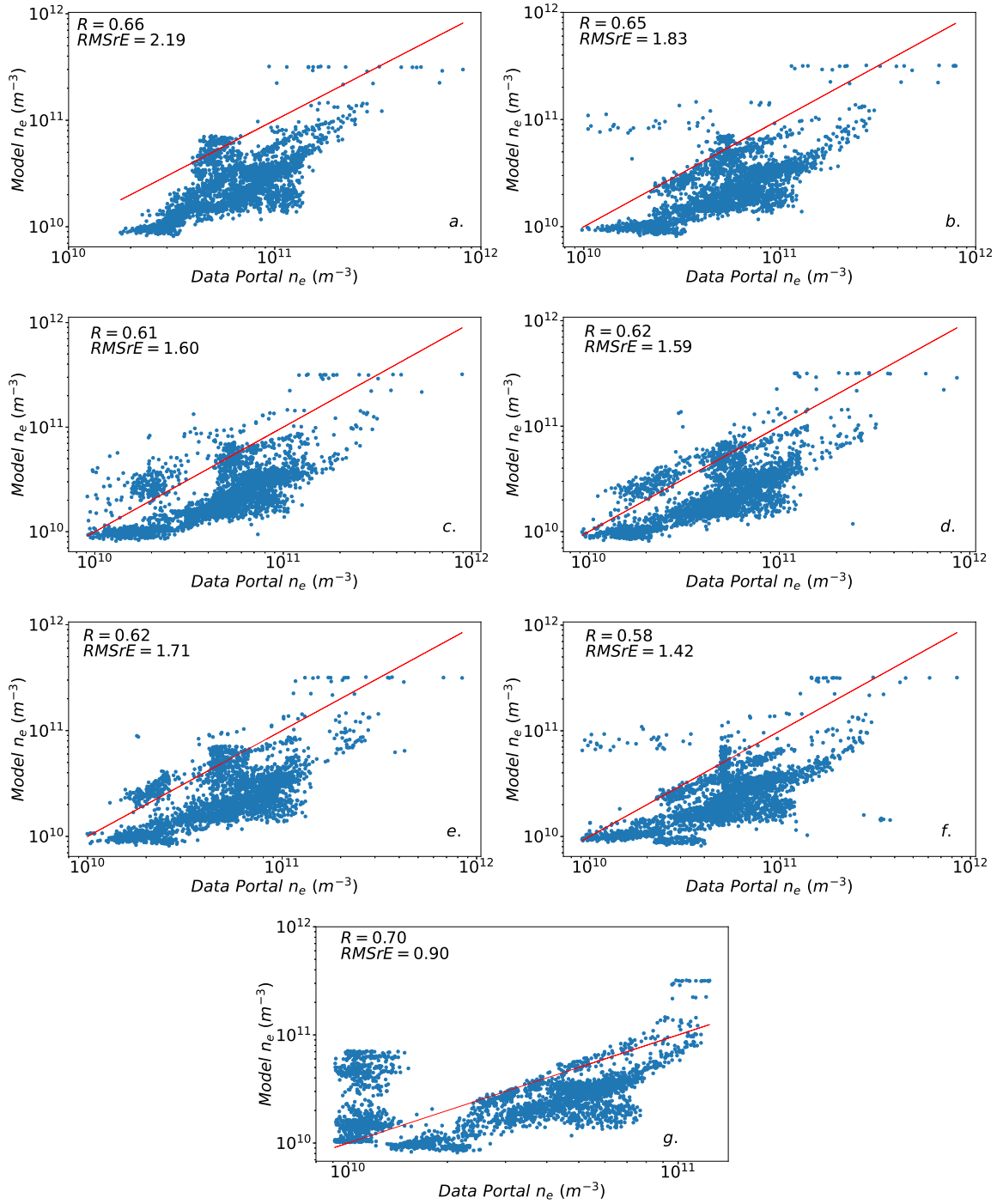


Figure 4.13: Correlation plot of density inferences using the neural network model and reported density on the Proba-2 portal for SLPA (a) segment 1, (b) segment 2, (c) segment 3, (d) segment 4, (e) segment 5, (f) segment 7, and (g) the guard. The solid line corresponds to a perfect agreement.

Table 4.3: Summary of the metrics of similarity between neural network and RBF inferences, and reported inferences of the densities for the six segments considered.

Segment	Method	RMSrE	MRE	R	offset
1	RBF	3.21	10.26	0.64	2.65
	NN	2.19	8.22	0.66	1.87
2	RBF	2.61	9.57	0.64	2.14
	NN	1.83	8.36	0.65	1.51
3	RBF	2.29	8.91	0.59	1.86
	NN	1.60	6.77	0.61	1.31
4	RBF	2.28	15.03	0.61	1.81
	NN	1.59	19.52	0.62	1.26
5	RBF	2.50	9.62	0.60	1.97
	NN	1.71	7.53	0.62	1.37
7	RBF	2.79	32.89	0.56	2.00
	NN	2.04	25.51	0.58	1.42

4.5 Summary and Conclusions

Results are presented for the interpretation of measurements made by a spherical segmented Langmuir probe using two multivariate regression techniques. As a first step, the approach is assessed by considering an idealised probe consisting of twenty equipotential segments that are insulated from one another, from which ten segments are used in the analysis. The segments are centered at different points on the spherical guard in such a way that they are symmetrically oriented relative to the direction of incoming plasma flow. Three-dimensional kinetic PIC and test particle simulations are made to calculate currents collected by each segment at a fixed satellite potential for different plasma parameters relevant to space environment near satellites in LEO at mid latitudes. These currents and the corresponding plasma conditions are used to construct a first synthetic data set to train inference models, and assess their skills. In the simulations, only the spherical guard of the probe, its equipotential segments and post are considered, which should be valid provided that the probe be on the ram side, sufficiently far from other satellite components. The geomagnetic field is also neglected, since the probe is biased so as to collect ion current, and the fact that for the conditions considered, ion gyroradii in the ionosphere are of the order 1 m for H^+ , and 5 m for O^+ , which are much larger than the probe radius. This should again be valid provided that the probe be held sufficiently far from the satellite, and well separated from other satellite components. Synthetic data are then used to construct inference models for the plasma density, the satellite potential, and plasma transverse flow velocity. The density model is constructed using RBF and neural network, and both have comparable excellent inference skills. The two models yield densities with a MRE of 9.4% and 10.6% for RBF and neural network respectively, when applied to the validation set obtained from simulations. A transverse velocity model is also trained using neural network and it shows a good inference skill when assessed quantitatively using the synthetic validation data set. The RMSE in the model inference

is estimated to be 45.4 m/s, which is about 2.3% relative to the [-1000, 1000] m/s velocity range, in arbitrary directions, considered in the data set.

A second synthetic data set is constructed using the Proba-2 probe geometry. The currents collected by the segments are calculated using a similar approach to that for the idealised probe, with the main difference being that variable effective satellite potentials relative to which the probes are biased, are assumed in the interval -6 to -3 V. The choice of the range of satellite potentials is based on the reported probe characteristics on the Proba-2 SLPA data portal. As with the first synthetic data, RBF and neural network models are trained to infer the plasma density. The two models have a MRE of 9.6% and 7.1% for RBF and neural network respectively. In this case again, the neural network inferences are more accurate than RBF when inferences are made with the synthetic validation set. Comparing the results to the ones obtained with the idealised probe synthetic data set where only a single potential is assumed for the satellite, it is found that the model accuracy when using RBF is comparable, but in the case of the neural network, the results obtained when varying the floating potential are slightly better than when it is fixed. The overall performance of the models are nonetheless good whether the satellite potential is varied or fixed. The neural network model is also trained to infer the satellite potential using the synthetic data. The model performance on the validation set is good, with a mean absolute error of 0.063 V, which corresponds to an uncertainty around 2% relative to the range of satellite potential considered in constructing the model. The final model is constructed using neural network model to infer the transverse velocity, and the model has an excellent inference skill when applied to the synthetic validation data set with a root mean square error of 39.5 m/s. The density models trained with Proba-2 geometry synthetic data are then applied to Proba-2 SLPA in-situ measurement using the currents reported in the portal as the input values, and the models' inferences are compared to the reported values on Proba-2 portal. Systematic discrepancies are

found in the inferred densities, with the reported data in the portal having higher values than the model inferences.

To conclude, kinetic simulations combined with multivariate regressions and machine learning techniques appear as a new promising avenue to better infer plasma parameters from currents collected with segmented Langmuir probes for which no analytic expressions are available. The simulations used here can reproduce known analytic results under conditions assumed in theories from which they were derived. They can also account for conditions and physical processes and geometries which are too complex to be tractable analytically. The assessment of the two methods considered, using synthetic data, shows good inference skills for all the parameters considered, and the application of the density model to actual in-situ measurements are found to be in good qualitative agreement with reported inferences for the segmented Langmuir probes on the Proba-2 data portal. Quantitatively however, systematic differences are found, with regression inferred densities being lower than values reported on the data portal, generally by more than a factor two. Owing to unknown confidence intervals in physical parameters reported on the Proba-2 data portal, and without knowing how these inferences were made, it is not possible to conclude whether the technique presented here leads to an improvement in inference accuracy, and if so, to what extent. In order to make such an assessment, more detailed simulations and comparisons with cross validated measurements made in different plasma conditions and geometries, using independent instruments and quantified uncertainties will be needed.

Chapter 5

Conclusion

In this thesis, a new approach to infer plasma parameters and satellite potentials from fixed bias probes is presented. The choice of fixed bias probes over the commonly used sweep mode is based on the higher temporal and spatial resolutions of their measurements. The study follows a multidisciplinary approach to the problem of plasma and satellite parameters inference, by applying kinetic simulations, state of the art data analysis procedures, and machine learning techniques. The research was motivated primarily by three objectives. The first is to construct and assess inference models which can account for more realistic geometries, and physical conditions under which measurements are made. The second is to provide inference techniques with quantified uncertainty margins. The third objective is to construct inference models with the potential of being improved incrementally, by accounting for more details in the geometry, or physical processes in the simulations as needed. While questions remain, and additional work is needed to further refine the approaches presented in the thesis, each of these objectives has been in good part realised. The use of three-dimensional kinetic simulations, in domains discretised with adaptive unstructured tetrahedral meshes, makes it possible to account for the actual geometries of the probe and nearby satellite components. Such codes are also capable of including progressively more physical effects, while being able to reproduce analytic results under conditions in which they are valid. In the simulations, different plasma

parameters; i.e., plasma densities, temperature, and multiple ion masses obtained from IRI model are used. The currents collected by the probes are calculated from simulations, and they are then used to build a solution library or synthetic data set, from which inference models are constructed and validated.

In the first project, kinetic simulations of an isolated small spherical Langmuir probe, attached to a post in plasma were made. For simplicity, the presence of satellite components was neglected in the simulation, and both the probe and the post were assumed to be biased at a fixed potential relative to the satellite. The calculated currents collected by the probe are used as the independent variables in the models constructed to infer the satellite floating potential and the ratio of density and the square root of temperature. Three methods are used to construct models. The first makes use of analytic formulas derived from the electron current collected by a spherical probe in an OML approximation to make estimates of both the floating potential and the ratio density divided by the square root of the temperature. The analytic estimates for the floating potentials over-predicted the actual floating potentials while the ratio $n_e/\sqrt{T_{eV}}$ estimates are smaller than the actual simulated data values. These discrepancies in the analytic estimates are in part due to the fact that the analytic formula used is obtained from OML approximation for electron currents collected by a spherical probe by neglecting contribution from the ions. While this might contribute in part to the overestimate, most of the overestimate of the floating potential likely comes from the neglect of T_{eV} in equation 2.5. For $n_e/\sqrt{T_{eV}}$, the analytic estimate based on equation 2.7 is underestimated because the probe surface area (the effective r^2) is overestimated in the analytic expression as it does not account for the area of the stub (the bottom portion of the post) with which the probe spherical surface is in contact. The second method uses radial basis function (RBF) regression in a multi-multivariate space, while the third approach involves the use of the boosting ensemble learning approach. In the latter approach, analytic formulas and the RBF are combined to train models for the floating potential and the ratio

$n_e/\sqrt{T_{eV}}$. The first inferences are made with the analytic formulas followed by RBF to correct errors made in the initial analytic estimate. The advantage of using the boosting ensemble is that it reduces the variance and increases the skill of the models, resulting in models with excellent skills. The performances of the three approaches used to train the models are assessed, and it is found that the boosting ensemble method gives the best inference for both the satellite floating potential and the ratio of density to the square root of temperature when they are applied to the validation data set.

The second part of this thesis goes beyond the ideal conditions considered in the first part, by accounting for more physical processes such as the plasma sheath around the spacecraft. Simulations are made using a geometry consisting of an approximate truncated Swarm satellite, the two Langmuir probes at fixed potentials of 4 V and 5 V with respect to the satellite, and different satellite potentials in the range [-3, 0] V, under different plasma conditions relevant to those found along the Swarm orbit. The calculated currents for the two probes are used as the independent variables in the models, while the plasma and satellite parameters used in the simulations are the dependent variables for which inference models are trained and validated. Models are constructed for the satellite potentials and the ratio $n_e/\sqrt{T_{eV}}$ using three approaches including the use of affine transformation to transform the analytic estimates, the combination of RBF and analytic formulas by applying the boosting ensemble learning method, and only RBF. The analytic estimates for both the satellite potentials, and the ratio $n_e/\sqrt{T_{eV}}$ follow similar patterns to the observations in the first project when they are compared with known values from the validation set. These estimates have excellent affinities with the actual simulated data values as evidenced by the high Pearson correlation coefficients of 0.98 and 0.99 for the satellite potentials, and the ratio $n_e/\sqrt{T_{eV}}$ respectively. These strong affinities motivated the use of affine transformations which improve the accuracy of the models drastically. The boosting ensemble models and RBF models for both the satellite potential, and the ratio

$n_e/\sqrt{T_{eV}}$ have excellent inference skills, and their uncertainty margins are quantified. Overall, all the models from the three methods yield comparable skills, but the combined RBF-OML is slightly more accurate. For the density, only one model is trained using RBF, and the model has an excellent inference skill. The trained models are then applied to in-situ measurements obtained from the Swarm data portal for Swarm A. The reported currents for the gold plated probe are used as the independent variables in the models, to infer the plasma and satellite parameters of interest. The models' inferences show qualitative agreement with the reported values on the Swarm portal, even though systematic offsets are noticed between the model inferences and the values reported on the Swarm portal. Due to the absence of uncertainty margins in the in-situ measurements, it is impossible to conclude if the models' inferences are more accurate than the reported values, and if so, to what extent.

The final project of this thesis focuses on the inference of segmented spherical Langmuir probe measurements using kinetic simulations and machine learning approaches. Compared to other types of Langmuir probes, segmented probes are arguably the least often used, to diagnose the state of plasma. Their size and the fact that they consist of several equipotential caps or “segments”, from which individual currents are collected, introduce considerable complexities in the construction of inference techniques for their characteristics. In this project, the focus is on the use of new techniques to infer plasma densities, flow velocities, and satellite potentials, from currents collected by two segmented probes biased to two different fixed potentials relative to the spacecraft. As in the other two projects, the currents collected by each of the equipotential segments are calculated using a three-dimensional kinetic self-consistent particle-in-cell (PIC) and test particle simulations. Computed currents and corresponding known plasma and satellite parameters used as input in the simulations are then used to create a solution library with which regression-based inference models are constructed, following standard machine learning techniques. Two solution libraries are created, corresponding to i) an idealised probe geometry with 20 segments, of which only 10

were considered in the regressions, and ii) to the Proba-2 probe geometry. Models constructed with the training subsets of the two solution libraries are found to have excellent skill, when applied to their respective validation sets. Models constructed for the segmented probes on Proba-2 are then applied to in-situ measurements made with segmented Langmuir probes mounted on the Proba-2 satellite. The inferred densities are compared with the densities reported on the Proba-2 data portal. The advantage of this approach is that it readily produces uncertainty margins that are specifically related to the inference technique used. Finally, while this thesis has focused on inference models for spherical probes with different, but fixed potentials relative to a satellite, the methodology is by no means limited to this mode of operation, as it could readily be applied to probes operated in full sweep mode and any probe geometries. An important outcome and contribution of this thesis is that the use of machine learning techniques combined with kinetic simulations is shown to be a promising and useful tool to improve inferences of satellite and plasma parameters in space plasma, while providing confidence intervals. The methodology is also capable of implementing incremental adjustments and improvements in models, to account for specific conditions; something that is generally not possible or too difficult in practice, with models based on analytic approximations.

Future Work

The results presented in this study combine the use of data analysis procedures, kinetic simulations, and machine learning techniques to improve the inferences of plasma and satellite parameters from probe measurements. The data analysis aspect of the work involves wrangling¹ experimental data sets by cleaning, transforming, and storing the data in a useable format for testing the applicability of the models. These steps were carried out for all data sets involving reported in-situ measurements

¹Data wrangling is the process of cleaning, transforming and unifying messy and complex data sets for easy access and analysis.

considered in this thesis. One of the future plans is to improve on the data analysis procedures by implementing a robust automated approach by developing an algorithm that can be adapted to any satellite mission data sets. This algorithm would be in the form of a pipeline in which experimental data are extracted from the source where they are stored, transformed into clean and structured data, and then loaded into a database for accessibility and direct use for analysis without the need for further data wrangling. The supervised machine learning approaches used in this thesis requires labeled data sets making it impossible to use in-situ measurements to train the models. This is because in-situ or experimental data are not labeled since the plasma parameters and satellite parameters are unknown, therefore, the data sets used to construct the models are generated from the kinetic simulations in which plasma and satellite parameters are known as they are specified as input in the simulations. In the simulations, some physical processes and plasma conditions affecting probe measurements in space were neglected. Some examples are the presence of a magnetic field in the background plasma and the presence of suprathermal electrons. These assumptions should be addressed in future work while considering a broader range of plasma parameters by leveraging on one of the objectives of this work, which involves the implementation of incremental improvements to the models. However, the future work is not only limited to these, as it goes beyond accounting only for the physical processes, plasma conditions or the development of automated data analysis approaches. The final goal is to construct and deploy more accurate and scalable models to infer plasma and satellite parameters with estimates of the uncertainty margins or confidence intervals for specific space missions. Collaboration between experimentalists and modelers will be required to achieve all these future goals. These joint efforts will involve careful selection of plasma and satellite parameters of interest that will be used in the kinetic simulations, the determination of the types of probes and satellite geometries to consider, and access to in-situ data sets, in order to design and test the algorithm for data analyses. Aside from all these, there is a need for

other means of validating the accuracy of the models' inferences using independent instruments which will necessitate collaborations with instrument scientists. Finally, the scope of this study should be broadened to include the inference of other plasma state variables such as the electron and ion temperatures, ion mass distributions, and possible non-Maxwellian particle distribution functions. These are ambitious goals, but ones which can be pursued, and be successful by following and extending the approaches presented in this thesis.

Bibliography

- [1] A. K. Singh, A. Bhargawa, D. Siingh, and R. P. Singh, “Physics of Space Weather Phenomena: A Review,” *Geosciences*, vol. 11, no. 7, p. 286, 2021.
- [2] D. Baker, “What is space weather?” *Advances in Space Research*, vol. 22, no. 1, pp. 7–16, 1998.
- [3] N. Crosby and M. Rycroft, “ESF network on space weather and the earth’s weather, SPECIAL,” *Physics and Chemistry of the Earth, Part C: Solar, Terrestrial & Planetary Science*, vol. 26, no. 8, pp. 605–607, 2001.
- [4] A. K. Singh and R. Singh, “Space-weather-causes, consequences and predictions,” in *Indian Journal Of Physics and Proceedings of the Indian Association for the Cultivation of Science B*, Indian Association for the Cultivation of Science; 1999, vol. 77, 2003, pp. 611–616.
- [5] A. Singh, D. Siingh, and R. Singh, “Space weather: Physics, effects and predictability,” *Surveys in Geophysics*, vol. 31, no. 6, pp. 581–638, 2010.
- [6] H. Austin and N. Savani, “Skills for forecasting space weather,” *Weather*, vol. 73, no. 11, pp. 362–366, 2018.
- [7] G. Lapenta, “Space weather: Variability in the Sun-Earth connection,” in *The Dynamical Ionosphere*, Elsevier, 2020, pp. 61–85.
- [8] E. Loomis, “The great auroral exhibition of Aug. 28th to Sept. 4th, 1859,” *American Journal of Science*, vol. 2, no. 90, pp. 339–361, 1860.
- [9] M. Shea and D. Smart, “Compendium of the eight articles on the “Carrington Event” attributed to or written by Elias Loomis in the American Journal of Science, 1859–1861,” *Advances in Space Research*, vol. 38, no. 2, pp. 313–385, 2006.
- [10] K Lewandowski, “Massive electricity and communications blackouts on Earth as effect of change the Sun activity,” *Journal of Polish Safety and Reliability Association*, vol. 6, 2015.
- [11] J. G. Kappenman, L. J. Zanetti, and W. A. Radasky, “Geomagnetic storms can threaten electric power grid,” *Earth in Space*, vol. 9, no. 7, pp. 9–11, 1997.
- [12] J Elovaara, “Geomagnetically induced currents in the Nordic power system and their effects on equipment, control, protection and operation,” in *CIGRE General Session 1992,(CIGRE= Inter-national Conference on Large High Voltage Electric Systems), Paris, France, August 31-September 5, 1992*, 1992.

- [13] W. Radasky, “Overview of the impact of intense geomagnetic storms on the US high voltage power grid,” in *2011 IEEE International Symposium on Electromagnetic Compatibility*, IEEE, 2011, pp. 300–305.
- [14] R. Horne, S. Glauert, N. Meredith, D Boscher, V Maget, D Heynderickx, and D Pitchford, “Space weather impacts on satellites and forecasting the Earth’s electron radiation belts with SPACECAST,” *Space Weather*, vol. 11, no. 4, pp. 169–186, 2013.
- [15] N Balan, Y Ebihara, R Skoug, K Shiokawa, I. Batista, S Tulasi Ram, Y Omura, T Nakamura, and M.-C. Fok, “A scheme for forecasting severe space weather,” *Journal of Geophysical Research: Space Physics*, vol. 122, no. 3, pp. 2824–2835, 2017.
- [16] S. A. Murray, “The importance of ensemble techniques for operational space weather forecasting,” *Space Weather*, vol. 16, no. 7, pp. 777–783, 2018.
- [17] E. Camporeale, S. Wing, and J. Johnson, *Machine learning techniques for space weather*. Elsevier, 2018.
- [18] S. E. Milan, “Both solar wind-magnetosphere coupling and ring current intensity control of the size of the auroral oval,” *Geophysical Research Letters*, vol. 36, no. 18, 2009.
- [19] R Walker, T Terasawa, S. Christon, V Angelopoulos, M Hoshino, W Lennartsson, K Maezawa, D. Sibeck, R. Treumann, D. Williams, *et al.*, “Source and loss processes in the magnetotail,” *Space Science Reviews*, vol. 88, no. 1, pp. 285–353, 1999.
- [20] J. E. Borovsky and J. A. Valdivia, “The Earth’s magnetosphere: A systems science overview and assessment,” *Surveys in Geophysics*, vol. 39, no. 5, pp. 817–859, 2018.
- [21] M. B. McElroy, “Ionosphere and Magnetosphere,” *ENCYCLOPÆDIA BRITANNICA*. [Online]. Available: <https://www.britannica.com/science/ionosphere-and-magnetosphere>, 2012.
- [22] T. Hagfors and K. Schlegel, “Earth’s ionosphere,” in *The Century of Space Science*, Springer, 2001, pp. 1559–1584.
- [23] M Atiq, “Historical Review of Ionosphere in Perspective of Sources of Ionization and Radio Waves Propagation,” *Research & Reviews: Journal of Space Science & Technology*, vol. 7, no. 2, pp. 28–39, 2018.
- [24] H. M. Macdonald, “The bending of electric waves round a conducting obstacle,” *Proceedings of the Royal Society of London*, vol. 71, no. 467-476, pp. 251–258, 1903.
- [25] R. J. Strutt, “On the bending of waves round a spherical obstacle,” *Proceedings of the Royal Society of London*, vol. 72, no. 477-486, pp. 40–41, 1904.
- [26] R. D. Hunsucker and J. K. Hargreaves, *The high-latitude ionosphere and its effects on radio propagation*. Cambridge University Press, 2007.

- [27] N. Cheng, S. Song, and W. Li, “Multi-scale ionospheric anomalies monitoring and spatio-temporal analysis during intense storm,” *Atmosphere*, vol. 12, no. 2, p. 215, 2021.
- [28] P. Zbinden, M. Hidalgo, P Eberhahdt, and J Geiss, “Mass spectrometer measurements of the positive ion composition in the D-and E-regions of the ionosphere,” *Planetary and Space Science*, vol. 23, no. 12, pp. 1621–1642, 1975.
- [29] J. H. Hoffman, “Studies of the composition of the ionosphere with a magnetic deflection mass spectrometer,” *International Journal of Mass Spectrometry and Ion Physics*, vol. 4, no. 4, pp. 315–322, 1970.
- [30] R. S. Narcisi, “Mass spectrometer measurements in the ionosphere,” in *Physics and Chemistry of Upper Atmosphere*, Springer, 1973, pp. 171–183.
- [31] L. Goembel and J. P. Doering, “Instrument for measuring spacecraft potential,” *Journal of Spacecraft and Rockets*, vol. 35, no. 1, pp. 66–72, 1998.
- [32] D. P. Peletier, “The Atmosphere Explorer Photoelectron Spectrometer,” *IEEE Transactions on Nuclear Science*, vol. 22, pp. 560–564, 1975.
- [33] L. Goembel, “Measuring spacecraft potential with an electron spectrometer,” in *6th Spacecraft Charging Technology Conference*, 2000.
- [34] L. Goembel, “A Novel Spacecraft Charge Monitor for LEO,” in *8th Spacecraft Charging Technology Conference*, 2003.
- [35] R. Zaplotnik, G. Primc, A. Vesel, *et al.*, “Optical Emission Spectroscopy as a Diagnostic Tool for Characterization of Atmospheric Plasma Jets,” *Applied Sciences*, vol. 11, no. 5, p. 2275, 2021.
- [36] U. Fantz, “Basics of plasma spectroscopy,” *Plasma Sources Science and Technology*, vol. 15, no. 4, S137, 2006.
- [37] Z. Ren, M. Guo, Y. Cheng, Y. Wang, W. Sun, H. Zhang, M. Dong, and G. Li, “A review of the development and application of space miniature mass spectrometers,” *Vacuum*, vol. 155, pp. 108–117, 2018.
- [38] P. R. Mahaffy, M. Benna, T. King, D. N. Harpold, R. Arvey, M. Barciniak, M. Bendt, D. Carrigan, T. Errigo, V. Holmes, *et al.*, “The neutral gas and ion mass spectrometer on the Mars atmosphere and volatile evolution mission,” *Space Science Reviews*, vol. 195, no. 1, pp. 49–73, 2015.
- [39] B. M. Jakosky, R. P. Lin, J. M. Grebowsky, J. G. Luhmann, D. Mitchell, G Beutelschies, T Priser, M Acuna, L Andersson, D Baird, *et al.*, “The Mars atmosphere and volatile evolution (MAVEN) mission,” *Space Science Reviews*, vol. 195, no. 1, pp. 3–48, 2015.
- [40] O. I. Korablev, J.-L. Bertaux, E. Dimarellis, A. Grigoriev, Y. Kalinnikov, A. Stepanov, and S Guibert, “AOTF-based spectrometer for Mars atmosphere sounding,” in *Infrared Spaceborne Remote Sensing X*, International Society for Optics and Photonics, vol. 4818, 2002, pp. 261–271.

- [41] O. Korablev, J.-L. Bertaux, A. Fedorova, D Fonteyn, A Stepanov, Y. Kalinikov, A Kiselev, A Grigoriev, V Jegoulev, S. Perrier, *et al.*, “SPICAM IR acousto-optic spectrometer experiment on Mars Express,” *Journal of Geophysical Research: Planets*, vol. 111, no. E9, 2006.
- [42] O. Korablev, A. Fedorova, J.-L. Bertaux, A. Stepanov, A Kiselev, Y. K. Kalinikov, A. Y. Titov, F. Montmessin, J.-P. Dubois, E. Villard, *et al.*, “SPICAV IR acousto-optic spectrometer experiment on Venus Express,” *Planetary and Space Science*, vol. 65, no. 1, pp. 38–57, 2012.
- [43] M. Yao, G. Chen, Z. Zhao, Y. Wang, and B. Bai, “A novel low-power multifunctional ionospheric sounding system,” *IEEE Transactions on Instrumentation and Measurement*, vol. 61, no. 5, pp. 1252–1259, 2011.
- [44] L. McNamara, D. Cooke, C. Valladares, and B. Reinisch, “Comparison of CHAMP and Digisonde plasma frequencies at Jicamarca, Peru,” *Radio Science*, vol. 42, no. 02, pp. 1–14, 2007.
- [45] J. Semeter, “High-resolution approaches to ionospheric exploration,” in *The Dynamical Ionosphere*, Elsevier, 2020, pp. 223–241.
- [46] W. E. Gordon, “Incoherent scattering of radio waves by free electrons with applications to space exploration by radar,” *Proceedings of the IRE*, vol. 46, no. 11, pp. 1824–1829, 1958.
- [47] T Hagfors, W. Birkmayer, and M Sulzer, “A new method for accurate ionospheric electron density measurements by incoherent scatter radar,” *Journal of Geophysical Research: Space Physics*, vol. 89, no. A8, pp. 6841–6845, 1984.
- [48] R. Tsunoda, M. Baron, J Owen, and D. Towle, “Altair: An incoherent scatter radar for equatorial spread F studies,” *Radio Science*, vol. 14, no. 6, pp. 1111–1119, 1979.
- [49] J. Salah and J. Holt, “Midlatitude thermospheric winds from incoherent scatter radar and theory,” *Radio Science*, vol. 9, no. 2, pp. 301–313, 1974.
- [50] J. Lei, L. Liu, W. Wan, and S.-R. Zhang, “Variations of electron density based on long-term incoherent scatter radar and ionosonde measurements over Millstone Hill,” *Radio Science*, vol. 40, no. 2, 2005.
- [51] I. Häggström, A. Belehaki, M. Hapgood, and J. Watermann, “3.8. Incoherent and coherent scatter radars,” in *The ESPAS e-infrastructure*: EDP Sciences, 2021, pp. 117–126.
- [52] R. A. Marshall and C. M. Cully, “Atmospheric effects and signatures of high-energy electron precipitation,” in *The dynamic loss of Earth’s radiation belts*, Elsevier, 2020, pp. 199–255.
- [53] G Ioannidis and D. Farley, “LETTERS, incoherent scatter observations at Arecibo using compressed pulses,” *Radio Science*, vol. 7, no. 7, pp. 763–766, 1972.
- [54] D. Farley, “Early incoherent scatter observations at Jicamarca,” *Journal of Atmospheric and Terrestrial Physics*, vol. 53, no. 8, pp. 665–675, 1991.

- [55] W. Liu, J. Burchill, L. Cogger, E. Donovan, G. James, D. Kendall, D. Knudsen, J. Lu, I. Mann, R. Michaud, *et al.*, “Multiscale Geospace Physics in Canada,” in *Multiscale Coupling of Sun-Earth Processes*, Elsevier, 2005, pp. 487–508.
- [56] Z. Ding, J. Wu, Z. Xu, B. Xu, and L. Dai, “The Qujing incoherent scatter radar: system description and preliminary measurements,” *Earth, Planets and Space*, vol. 70, no. 1, pp. 1–13, 2018.
- [57] R. G. Gillies, A van Eyken, E. Spanswick, M Nicolls, J Kelly, M Greffen, D Knudsen, M Connors, M. Schutzer, T Valentic, *et al.*, “First observations from the RISR-C incoherent scatter radar,” *Radio Science*, vol. 51, no. 10, pp. 1645–1659, 2016.
- [58] H. Singer, L. Matheson, R. Grubb, A. Newman, and D. Bouwer, “Monitoring space weather with the GOES magnetometers,” in *GOES-8 and Beyond*, International Society for Optics and Photonics, vol. 2812, 1996, pp. 299–308.
- [59] B. Fraser, R. Grew, S. Morley, J. Green, H. Singer, T. Loto’aniu, and M. Thomsen, “Storm time observations of electromagnetic ion cyclotron waves at geosynchronous orbit: GOES results,” *Journal of Geophysical Research: Space Physics*, vol. 115, no. A5, 2010.
- [60] J.-M. Leger, F. Bertrand, T. Jager, M. Le Prado, I. Fratter, and J.-C. Lalaurie, “Swarm absolute scalar and vector magnetometer based on helium 4 optical pumping,” *Procedia Chemistry*, vol. 1, no. 1, pp. 634–637, 2009.
- [61] D. Anderson, A. Anghel, J. Chau, and O. Veliz, “Daytime vertical $E \times B$ drift velocities inferred from ground-based magnetometer observations at low latitudes,” *Space Weather*, vol. 2, no. 11, 2004.
- [62] R. Zhang, L. Liu, H. Le, and Y. Chen, “Equatorial ionospheric electrodynamics over Jicamarca during the 6–11 September 2017 space weather event,” *Journal of Geophysical Research: Space Physics*, vol. 124, no. 2, pp. 1292–1306, 2019.
- [63] M. Abdu, E. De Paula, I. Batista, B. Reinisch, M. Matsuoka, P. Camargo, O. Veliz, C. Denardini, J. Sobral, E. Kherani, *et al.*, “Abnormal evening vertical plasma drift and effects on ESF and EIA over Brazil-South Atlantic sector during the 30 October 2003 superstorm,” *Journal of Geophysical Research: Space Physics*, vol. 113, no. A7, 2008.
- [64] I. Mann, D. Milling, I. Rae, L. Ozeke, A Kale, Z. Kale, K. Murphy, A Parent, M Usanova, D. Pahud, *et al.*, “The upgraded CARISMA magnetometer array in the THEMIS era,” *Space Science Reviews*, vol. 141, no. 1, pp. 413–451, 2008.
- [65] J. Krehbiel, L. Brace, R. Theis, W. Pinkus, and R. Kaplan, “The Dynamics Explorer Langmuir probe instrument,” *Space Science Instrumentation*, vol. 5, pp. 493–502, 1981.
- [66] P Travnicek, D Hercik, S Stverak, P Hellinger, J.-P. Lebreton, Z Kozacek, and J Brinek, “The DSLP Langmuir Probe experiment on-board Proba2: scientific objectives and description,” in *EGU General Assembly Conference Abstracts*, 2009, p. 11967.

- [67] F. Catapano, S. Buchert, I. Coco, E. Slominska, E. Qamili, L. Trenchi, and J. Bouffard, “Swarm Langmuir Probe measurements: analysis and characterization of the data quality,” in *EGU General Assembly Conference Abstracts*, 2020, p. 13 403.
- [68] I. Langmuir and H. Mott-Smith, “The theory of collectors in gaseous discharges,” *Phys. Rev.*, vol. 28, no. 4, p. 99, 1926.
- [69] H. M. Mott-Smith and I. Langmuir, “The theory of collectors in gaseous discharges,” *Physical Review*, vol. 28, no. 4, p. 727, 1926.
- [70] E. C. Whipple, “Potentials of surfaces in space,” *Reports on Progress in Physics*, vol. 44, no. 11, p. 1197, 1981.
- [71] R Chodura, “Plasma–wall transition in an oblique magnetic field,” *The Physics of Fluids*, vol. 25, no. 9, pp. 1628–1633, 1982.
- [72] W Fox, J Matteucci, C Moissard, D. Schaeffer, A Bhattacharjee, K Germaschewski, and S. Hu, “Kinetic simulation of magnetic field generation and collisionless shock formation in expanding laboratory plasmas,” *Physics of Plasmas*, vol. 25, no. 10, p. 102 106, 2018.
- [73] O. Larroche, “Kinetic simulation of a plasma collision experiment,” *Physics of Fluids B: Plasma Physics*, vol. 5, no. 8, pp. 2816–2840, 1993.
- [74] X.-L. Zhu, W. Chen, F. Wang, and Z.-X. Wang, “Hybrid-kinetic simulation of resonant interaction between energetic-ions and tearing modes in a tokamak plasma,” *Nuclear Fusion*, vol. 60, no. 4, p. 046 023, 2020.
- [75] K. Fujimoto, “Multi-scale kinetic simulation of magnetic reconnection with dynamically adaptive meshes,” *Frontiers in Physics*, vol. 6, p. 119, 2018.
- [76] J. Dargent, N. Aunai, B Lavraud, S. Toledo-Redondo, M. Shay, P. Cassak, and K Malakit, “Kinetic simulation of asymmetric magnetic reconnection with cold ions,” *Journal of Geophysical Research: Space Physics*, vol. 122, no. 5, pp. 5290–5306, 2017.
- [77] R. Marchand and P. A. R. Lira, “Kinetic Simulation of Spacecraft–Environment Interaction,” *IEEE Transactions on Plasma Science*, vol. 45, no. 4, pp. 535–554, 2017.
- [78] J.-L. Vay, P Colella, P McCorquodale, B Van Straalen, A Friedman, and D. Grote, “Mesh refinement for particle-in-cell plasma simulations: Applications to and benefits for heavy ion fusion,” *Laser and Particle Beams*, vol. 20, no. 4, pp. 569–575, 2002.
- [79] B. Wang, S. Ethier, W. Tang, K. Z. Ibrahim, K. Madduri, S. Williams, and L. Oliker, “Modern gyrokinetic particle-in-cell simulation of fusion plasmas on top supercomputers,” *The International Journal of High Performance Computing Applications*, vol. 33, no. 1, pp. 169–188, 2019.

- [80] Y. K. Batygin, “Particle-in-cell code BEAMPATH for beam dynamics simulations in linear accelerators and beamlines,” *Nuclear Instruments and Methods in Physics Research Section A: Accelerators, Spectrometers, Detectors and Associated Equipment*, vol. 539, no. 3, pp. 455–489, 2005.
- [81] J. Li, B. Ni, L. Xie, Z. Pu, J. Bortnik, R. M. Thorne, L. Chen, Q. Ma, S. Fu, Q. Zong, *et al.*, “Interactions between magnetosonic waves and radiation belt electrons: Comparisons of quasi-linear calculations with test particle simulations,” *Geophysical Research Letters*, vol. 41, no. 14, pp. 4828–4834, 2014.
- [82] E. Jaeger and T. Speiser, “Energy and pitch angle distributions for auroral ions using the current sheet acceleration model,” *Astrophysics and Space Science*, vol. 28, no. 1, pp. 129–144, 1974.
- [83] F. Mackay, R. Marchand, K. Kabin, and J. Lu, “Test kinetic modelling of collisionless perpendicular shocks,” *Journal of Plasma Physics*, vol. 74, no. 3, pp. 301–318, 2008.
- [84] G. Paesold and A. O. Benz, “Test particle simulation of the Electron Firehose instability,” *Astronomy & Astrophysics*, vol. 401, no. 2, pp. 711–720, 2003.
- [85] R. Marchand, “Test-Particle Simulation of Space Plasmas,” *Communications in Computational Physics*, vol. 8, no. 3, p. 471, 2010.
- [86] M. Palmroth, U. Ganse, Y. Pfau-Kempf, M. Battarbee, L. Turc, T. Brito, M. Grandin, S. Hoilijoki, A. Sandroos, and S. von Alfthan, “Vlasov methods in space physics and astrophysics,” *Living Reviews in Computational Astrophysics*, vol. 4, no. 1, pp. 1–54, 2018.
- [87] I. Silin and J. Büchner, “Vlasov-code simulations of collisionless plasmas,” in *Erfahrungen mit den IBM-Parallelrechnersystemen RS/6000 SP and pSeries690*, GWDG, 2003, pp. 35–50.
- [88] T. Dannert and F. Jenko, “Vlasov simulation of kinetic shear Alfvén waves,” *Computer Physics Communications*, vol. 163, no. 2, pp. 67–78, 2004.
- [89] J. Müller, S. Simon, U. Motschmann, J. Schüle, K.-H. Glassmeier, and G. J. Pringle, “AIKEF: Adaptive hybrid model for space plasma simulations,” *Computer Physics Communications*, vol. 182, no. 4, pp. 946–966, 2011.
- [90] P. L. Ventzek, T. J. Sommerer, R. J. Hoekstra, and M. J. Kushner, “Two-dimensional hybrid model of inductively coupled plasma sources for etching,” *Applied Physics Letters*, vol. 63, no. 5, pp. 605–607, 1993.
- [91] E. Valeo, “Fluid-PIC Hybrid Code Development for Laser-Plasma Interaction Simulation,” in *APS Division of Plasma Physics Meeting Abstracts*, 1996, 9Q–01.
- [92] R. Kawashima, Z. Wang, and K. Komurasaki, “Hybrid Vlasov-Fluid Model with High-Order Schemes for Partially Ionized Plasma Flows,” in *AIAA Scitech 2021 Forum*, 2021, p. 0553.
- [93] G. Bell, T. Hey, A. Szalay, *et al.*, “Beyond the data deluge,” *Science*, vol. 323, no. 5919, pp. 1297–1298, 2009.

- [94] A. Karpatne, G. Atluri, J. H. Faghmous, M. Steinbach, A. Banerjee, A. Ganguly, S. Shekhar, N. Samatova, and V. Kumar, “Theory-guided data science: A new paradigm for scientific discovery from data,” *IEEE Transactions on Knowledge and Data Engineering*, vol. 29, no. 10, pp. 2318–2331, 2017.
- [95] B. K. Spears, J. Brase, P.-T. Bremer, B. Chen, J. Field, J. Gaffney, M. Kruse, S. Langer, K. Lewis, R. Nora, *et al.*, “Deep learning: A guide for practitioners in the physical sciences,” *Physics of Plasmas*, vol. 25, no. 8, p. 080 901, 2018.
- [96] G. Carleo, I. Cirac, K. Cranmer, L. Daudet, M. Schuld, N. Tishby, L. Vogt-Maranto, and L. Zdeborová, “Machine learning and the physical sciences,” *Reviews of Modern Physics*, vol. 91, no. 4, p. 045 002, 2019.
- [97] M. Buchanan, “The power of machine learning,” Ph.D. dissertation, Nature Publishing Group, 2019.
- [98] H. B. Barlow, “Unsupervised learning,” *Neural Computation*, vol. 1, no. 3, pp. 295–311, 1989.
- [99] S. Feng, H. Zhou, and H. Dong, “Using deep neural network with small dataset to predict material defects,” *Materials & Design*, vol. 162, pp. 300–310, 2019.
- [100] A. Dawson, T. Palmer, and S Corti, “Simulating regime structures in weather and climate prediction models,” *Geophysical Research Letters*, vol. 39, no. 21, 2012.
- [101] G. Bonaccorso, *Machine learning algorithms*. Packt Publishing Ltd, 2017.
- [102] B. Mahesh, “Machine Learning Algorithms-A Review,” *International Journal of Science and Research (IJSR).[Internet]*, vol. 9, pp. 381–386, 2020.
- [103] G. James, D. Witten, T. Hastie, and R. Tibshirani, *An introduction to statistical learning*. Springer, 2013, vol. 112.
- [104] R. Yacouby and D. Axman, “Probabilistic Extension of Precision, Recall, and F1 Score for More Thorough Evaluation of Classification Models,” in *Proceedings of the First Workshop on Evaluation and Comparison of NLP Systems*, 2020, pp. 79–91.
- [105] H. R. Sofaer, J. A. Hoeting, and C. S. Jarnevich, “The area under the precision-recall curve as a performance metric for rare binary events,” *Methods in Ecology and Evolution*, vol. 10, no. 4, pp. 565–577, 2019.
- [106] Y. Han, L. Wang, W. Fu, H. Zhou, T. Li, and R. Chen, “Machine Learning-Based Short-term GPS TEC Forecasting during High Solar Activity and Magnetic Storm Periods,” *IEEE Journal of Selected Topics in Applied Earth Observations and Remote Sensing*, 2021.
- [107] M. Bobra, “Predicting solar activity using machine-learning methods,” in *AGU Fall Meeting Abstracts*, vol. 2017, 2017, SM14A–03.
- [108] M. G. Bobra and S. Couvidat, “Solar flare prediction using SDO/HMI vector magnetic field data with a machine-learning algorithm,” *The Astrophysical Journal*, vol. 798, no. 2, p. 135, 2015.

- [109] C. D. Baso and A. A. Ramos, “Enhancing SDO/HMI images using deep learning,” *Astronomy & Astrophysics*, vol. 614, A5, 2018.
- [110] R. M. McGranaghan, A. J. Mannucci, B. Wilson, C. A. Mattmann, and R. Chadwick, “New capabilities for prediction of high-latitude ionospheric scintillation: A novel approach with machine learning,” *Space Weather*, vol. 16, no. 11, pp. 1817–1846, 2018.
- [111] H. Breuillard, R. Dupuis, A. Retino, O. L. Contel, J. Amaya, and G. Lapenta, “Automatic classification of plasma regions in near-Earth space with supervised machine learning: Application to magnetospheric multi scale 2016-2019 observations,” *arXiv preprint arXiv:2009.00566*, 2020.
- [112] G. Liang, X. Zhu, and C. Zhang, “An empirical study of bagging predictors for different learning algorithms,” in *Twenty-Fifth AAAI Conference on Artificial Intelligence*, 2011.
- [113] A. Ghasemian, H. Hosseinmardi, A. Galstyan, E. M. Airoidi, and A. Clauset, “Stacking models for nearly optimal link prediction in complex networks,” *Proceedings of the National Academy of Sciences*, vol. 117, no. 38, pp. 23 393–23 400, 2020.
- [114] J. G. Laframboise, “Theory of spherical and cylindrical Langmuir probes in a collisionless, Maxwellian plasma at rest,” Toronto Univ Downsview (Ontario) Inst for Aerospace Studies, Tech. Rep., 1966.
- [115] F. F. Chen and D. Arnush, “The floating potential of cylindrical Langmuir probes,” *Physics of Plasmas*, vol. 8, no. 11, pp. 5051–5052, 2001.
- [116] J. Allen, R. Boyd, and P Reynolds, “The collection of positive ions by a probe immersed in a plasma,” *Proceedings of the Physical Society. Section B*, vol. 70, no. 3, p. 297, 1957.
- [117] A. Barjatya, C. M. Swenson, D. C. Thompson, and K. H. Wright Jr, “Invited article: Data analysis of the floating potential measurement unit aboard the International Space Station,” *Review of Scientific Instruments*, vol. 80, no. 4, p. 041 301, 2009.
- [118] A. Olowookere and R. Marchand, “Fixed Bias Probe Measurement of a Satellite Floating Potential,” *IEEE Transactions on Plasma Science*, vol. 49, no. 2, pp. 862–870, 2021.
- [119] A. Olowookere and R. Marchand, “Density–Temperature Constraint From Fixed-Bias Spherical Langmuir Probes,” *IEEE Transactions on Plasma Science*, vol. 49, no. 6, pp. 1997–1999, 2021.
- [120] R. D. Leach, *Failures and Anomalies Attributed to Spacecraft Charging*. National Aeronautics and Space Administration, Marshall Space Flight Center, 1995, vol. 1375.

- [121] V. M. Agüero, B. E. Gilchrist, S. D. Williams, W. J. Burke, L. Krause, and L. C. Gentile, “Current Collection Model Characterizing Shuttle Charging During the Tethered Satellite System Missions,” *Journal of Spacecraft and Rockets*, vol. 37, no. 2, pp. 212–217, 2000.
- [122] T. W. Flatley and H. E. Evans, *The Development of the Electric Field Meter for the Explorer VIII Satellite (1960)*. National Aeronautics and Space Administration, 1962.
- [123] R. Bourdeau, *Measurements of Sheath Currents and Equilibrium Potential on the Explorer VIII Satellite (1960)*. National Aeronautics and Space Administration, 1961.
- [124] D. McPherson, D. Cauffman, and W. Schober, “Spacecraft charging at high altitudes: SCATHA satellite program,” *Journal of Spacecraft and Rockets*, vol. 12, no. 10, pp. 621–626, 1975.
- [125] H. C. Koons, P. F. Mizera, J. F. Fennell, and D. F. Hall, “Spacecraft charging results from the SCATHA satellite,” (Aerospace Corp El Segundo CA Space Sciences Lab), Tech. Rep., 1981.
- [126] J. F. Fennell, “Description of P78-2 SCATHA Satellite and Experiments,” *The IMS Source Book*, p. 65, 1982.
- [127] E. Mullen, *SCATHA environmental atlas, 2*. Air Force Geophysics Laboratory, Air Force Systems Command, United State. . . , 1983, vol. 83.
- [128] E. Mullen, M. Gussenhoven, D. Hardy, T. Aggson, B. Ledley, and E Whipple, “SCATHA survey of high-level spacecraft charging in sunlight,” *Journal of Geophysical Research: Space Physics*, vol. 91, no. A2, pp. 1474–1490, 1986.
- [129] P. Craven, R. Olsen, J Fennell, D Croley, and T Aggson, “Potential modulation on the SCATHA spacecraft,” *Journal of Spacecraft and Rockets*, vol. 24, no. 2, pp. 150–157, 1987.
- [130] H. Nishimoto, H. Fujii, and T. Abe, “Observation of surface charging on Engineering Test Satellite V of Japan,” in *27th Aerospace Sciences Meeting*, 1989, p. 613.
- [131] K. H. Wright, C. M. Swenson, D. C. Thompson, A. Barjatya, S. L. Koontz, T. A. Schneider, J. A. Vaughn, J. I. Minow, P. D. Craven, V. N. Coffey, *et al.*, “Charging of the International Space Station as observed by the floating potential measurement unit: Initial results,” *IEEE Transactions on Plasma Science*, vol. 36, no. 5, pp. 2280–2293, 2008.
- [132] J. Lee, J. Doering, T. Potemra, and L. Brace, “Measurements of the ambient photoelectron spectrum from Atmosphere Explorer: I. AE-E measurements below 300 km during solar minimum conditions,” *Planetary and Space Science*, vol. 28, no. 10, pp. 947–971, 1980.

- [133] J. Lee, J. Doering, T. Potemra, and L. Brace, “Measurements of the ambient photoelectron spectrum from atmosphere explorer: II. AE-E measurements from 300 to 1000 km during solar minimum conditions,” *Planetary and Space Science*, vol. 28, no. 10, pp. 973–996, 1980.
- [134] I. Shkarofsky, “Accuracy of Langmuir probe measurements and skin potential on satellites,” *Journal of Geophysical Research*, vol. 76, no. 16, pp. 3746–3754, 1971.
- [135] N. Sanders and G. Inouye, “Secondary emission effects on spacecraft charging: Energy distribution considerations,” in *Spacecraft Charging Technology-1978*, vol. 2071, 1979, p. 747.
- [136] F. F. Chen, “Langmuir probe diagnostics,” in *IEEE-ICOPS Meeting, Jeju, Korea*, vol. 2, 2003.
- [137] V. Godyak and B. Alexandrovich, “Comparative analyses of plasma probe diagnostics techniques,” *Journal of Applied Physics*, vol. 118, no. 23, p. 233 302, 2015.
- [138] H. Shindo and Y. Horiike, “Floating potential in negative-ion-containing plasma,” *Japanese Journal of Applied Physics*, vol. 30, no. 1R, p. 161, 1991.
- [139] I. D. Sudit and R. C. Woods, “A study of the accuracy of various Langmuir probe theories,” *Journal of Applied Physics*, vol. 76, no. 8, pp. 4488–4498, 1994.
- [140] I Katz, D. Parks, M. Mandell, J. Harvey, D. Brownell Jr, S. Wang, and M Rotenberg, “A three dimensional dynamic study of electrostatic charging in materials, NASA Conf. Rep. CR-135256,” 1977.
- [141] M. J. Mandell, V. A. Davis, D. L. Cooke, A. T. Wheelock, and C J, “NASCAP-2k Spacecraft Charging Code Overview,” *IEEE Trans. Plasma Sci.*, vol. 34, pp. 2084–93, 2006.
- [142] T Muranaka, S Hosoda, J. Kim, S Hatta, K Ikeda, T Mamanaga, M Cho, H Usui, H. O. Ueda, K Koga, and T Goka, “Development of Multi-Utility Spacecraft Charging Analysis Tool (MUSCAT),” *IEEE Trans. Plasma Sci.*, vol. 36, no. 5, pp. 2336 –49, 2008.
- [143] J. Roussel, F Rogier, G Dufour, J. Matéo-Vélez, J Forest, A Hilgers, D Rogers, L Girard, and D Payan, “SPIS Open-Source Code: Methods, Capabilities, Achievements and Prospects,” *IEEE Trans. Plasma Sci.*, vol. 36, no. 5, pp. 2360 –8, 2008.
- [144] R. Marchand, “PTetra, a Tool to Simulate Low Orbit Satellite–Plasma Interaction,” *IEEE Transactions on Plasma Science*, vol. 40, no. 2, pp. 217–229, 2011.
- [145] N. Imtiaz and R. Marchand, “Particle-in-cell modeling of Dual Segmented Langmuir Probe on PROBA2,” *Astrophysics and Space Science*, vol. 360, no. 1, p. 15, 2015.

- [146] S Rehman, J Burchill, A. Eriksson, and R Marchand, “Earth magnetic field effects on Swarm electric field instrument,” *Planetary and Space Science*, vol. 73, no. 1, pp. 145–150, 2012.
- [147] J. Chalaturnyk and R. Marchand, “A First Assessment of a Regression-Based Interpretation of Langmuir Probe Measurements,” *Front. Phys.* 7: 63. doi: 10.3389/fphy, 2019.
- [148] R. L. Merlino, “Understanding Langmuir probe current-voltage characteristics,” *American Journal of Physics*, vol. 75, no. 12, pp. 1078–1085, 2007.
- [149] D. Knudsen, J. Burchill, S. Buchert, A. Eriksson, R. Gill, J.-E. Wahlund, L. Åhlén, M Smith, and B Moffat, “Thermal ion imagers and Langmuir probes in the Swarm electric field instruments,” *Journal of Geophysical Research: Space Physics*, vol. 122, no. 2, pp. 2655–2673, 2017.
- [150] D. G. Krige, “A statistical approach to some basic mine valuation problems on the Witwatersrand,” *Journal of the Southern African Institute of Mining and Metallurgy*, vol. 52, no. 6, pp. 119–139, 1951.
- [151] H. Wackernagel, “Multivariate geostatistics: An introduction with applications,” in *International Journal of Rock Mechanics and Mining Sciences and Geomechanics Abstracts*, Springer, vol. 33, 1996, 363A–363A.
- [152] K. Dai, G. Liu, K. Lim, and Y. Gu, “Comparison between the radial point interpolation and the kriging interpolation used in meshfree methods,” *Computational Mechanics*, vol. 32, no. 1-2, pp. 60–70, 2003.
- [153] M. L. Stein, *Interpolation of Spatial Data: Some Theory for Kriging*. Springer Science & Business Media, 2012.
- [154] I. A. Basheer and M Hajmeer, “Artificial neural networks: Fundamentals, computing, design, and application,” *Journal of Microbiological Methods*, vol. 43, no. 1, pp. 3–31, 2000.
- [155] I. Goodfellow, Y. Bengio, and A. Courville, *Deep Learning*. MIT Press, 2016, <http://www.deeplearningbook.org>.
- [156] H.-M. Gutmann, “A radial basis function method for global optimization,” *Journal of Global Optimization*, vol. 19, no. 3, pp. 201–227, 2001.
- [157] M. D. Buhmann, *Radial Basis Functions: Theory and Implementations*. Cambridge University Press, 2003, vol. 12.
- [158] C. Rusu and V. Rusu, “Radial basis functions versus geostatistics in spatial interpolations,” in *IFIP International Conference on Artificial Intelligence in Theory and Practice*, Springer, 2006, pp. 119–128.
- [159] L. Goembel, “Measuring spacecraft potential with an electron spectrometer,” in *SCT*, 1998, pp. 287–290.
- [160] J.-C. Mateo-Velez, J.-F. Roussel, D. Sarrail, F. Boulay, V. Inguibert, and D. Payan, “Ground plasma tank modeling and comparison to measurements,” *IEEE Transactions on Plasma Science*, vol. 36, no. 5, pp. 2369–2377, 2008.

- [161] K. A. Lynch, “The Dartmouth Elephant plasma facility,” *AGUFM*, vol. 2017, SM31C–04, 2017.
- [162] M. J. Rycroft, “Active experiments in space plasmas,” *Eos, Transactions American Geophysical Union*, vol. 61, no. 41, pp. 657–657, 1980.
- [163] J. E. Borovsky and G. L. Delzanno, “Active Experiments in Space: The Future,” *Frontiers in Astronomy and Space Sciences*, vol. 6, p. 31, 2019.
- [164] G. L. Delzanno, J. E. Borovsky, M. F. Thomsen, B. E. Gilchrist, and E. Sanchez, “Can an electron gun solve the outstanding problem of magnetosphere-ionosphere connectivity?” *Journal of Geophysical Research: Space Physics*, vol. 121, no. 7, pp. 6769–6773, 2016.
- [165] I. B. Bernstein and I. N. Rabinowitz, “Theory of Electrostatic Probes in a Low-Density Plasma,” *The Physics of Fluids*, vol. 2, no. 2, pp. 112–121, 1959.
- [166] S. Lam, “Unified theory for the Langmuir probe in a collisionless plasma,” *The Physics of Fluids*, vol. 8, no. 1, pp. 73–87, 1965.
- [167] F. F. Chen, “Numerical computations for ion probe characteristics in a collisionless plasma,” *Journal of Nuclear Energy. Part C, Plasma Physics, Accelerators, Thermonuclear Research*, vol. 7, no. 1, p. 47, 1965.
- [168] X. Chen and G. Sanchez-Arriaga, “Orbital motion theory and operational regimes for cylindrical emissive probes,” *Physics of Plasmas*, vol. 24, no. 2, p. 023 504, 2017.
- [169] K. K. Niyogi and I. M. Cohen, “Continuum electrostatic probe theory with magnetic field,” *The Physics of Fluids*, vol. 16, no. 1, pp. 69–74, 1973.
- [170] M. Tuszewski and J. Tobin, “The accuracy of Langmuir probe ion density measurements in low-frequency RF discharges,” *Plasma Sources Science and Technology*, vol. 5, no. 4, p. 640, 1996.
- [171] J. K. Hargreaves, *The solar-terrestrial environment: an introduction to geospace—the science of the terrestrial upper atmosphere, ionosphere, and magnetosphere*. Cambridge University Press, 1992.
- [172] G. Chisham, M. Lester, S. Milan, M. Freeman, W. Bristow, A. Grocott, K. McWilliams, J. Ruohoniemi, T. Yeoman, P. L. Dyson, *et al.*, “A decade of the Super Dual Auroral Radar Network (SuperDARN): Scientific achievements, new techniques and future directions,” *Surveys in Geophysics*, vol. 28, no. 1, pp. 33–109, 2007.
- [173] R. Schunk and A. Nagy, “Ionospheres: Physics, plasma physics, and chemistry. Cambridge: University Press, 628 p,” 2009.
- [174] M. M. Martinović, K. G. Klein, S. R. Gramze, H. Jain, M. Maksimović, A. Zaslavsky, C. Salem, I. Zouganelis, and Z. Simić, “Solar Wind Electron Parameters Determination on Wind Spacecraft Using Quasi-Thermal Noise Spectroscopy,” *Journal of Geophysical Research: Space Physics*, vol. 125, no. 8, e2020JA028113, 2020.

- [175] F. dos Santos Prol, M. Hernández-Pajares, M. Tadeu de Assis Honorato Muella, and P. de Oliveira Camargo, “Tomographic imaging of ionospheric plasma bubbles based on GNSS and radio occultation measurements,” *Remote Sensing*, vol. 10, no. 10, p. 1529, 2018.
- [176] E. Sardon, A Rius, and N Zarraoa, “Estimation of the transmitter and receiver differential biases and the ionospheric total electron content from Global Positioning System observations,” *Radio Science*, vol. 29, no. 03, pp. 577–586, 1994.
- [177] B. W. Reinisch, I. A. Galkin, G. Khmyrov, A. Kozlov, K Bibl, I. Lisysyan, G. Cheney, X Huang, D. Kitrosser, V. Paznukhov, *et al.*, “New Digisonde for research and monitoring applications,” *Radio Science*, vol. 44, no. 01, pp. 1–15, 2009.
- [178] M. J. Nicolls and C. J. Heinselman, “Three-dimensional measurements of traveling ionospheric disturbances with the Poker Flat Incoherent Scatter Radar,” *Geophysical Research Letters*, vol. 34, no. 21, 2007.
- [179] L. Lomidze, D. J. Knudsen, J. Burchill, A. Kouznetsov, and S. C. Buchert, “Calibration and validation of Swarm plasma densities and electron temperatures using ground-based radars and satellite radio occultation measurements,” *Radio Science*, vol. 53, no. 1, pp. 15–36, 2018.
- [180] R. Yan, Z. Zhima, C. Xiong, X. Shen, J. Huang, Y. Guan, X. Zhu, and C. Liu, “Comparison of electron density and temperature from the CSES satellite with other space-borne and ground-based observations,” *Journal of Geophysical Research: Space Physics*, vol. 125, no. 10, e2019JA027747, 2020.
- [181] H. Carlson and J Sayers, “Discrepancy in electron temperatures deduced from Langmuir probes and from incoherent scatter radars,” *Journal of Geophysical Research*, vol. 75, no. 25, pp. 4883–4886, 1970.
- [182] G. Wrenn, D. Clark, W. Raitt, and H. Carlson, “Modulation Langmuir probe and incoherent scatter radar measurements of ionospheric electron temperature,” *Journal of Atmospheric and Terrestrial Physics*, vol. 35, no. 3, pp. 405–413, 1973.
- [183] P. Diego, I. Coco, I. Bertello, M. Candidi, and P. Ubertini, “Ionospheric Plasma Density Measurements by Swarm Langmuir Probes: Limitations and possible Corrections,” *Annales Geophysicae Discussions*, pp. 1–15, 2019.
- [184] J. Boedo and D. Rudakov, “Estimation of plasma ion saturation current and reduced tip arcing using Langmuir probe harmonics,” *Review of Scientific Instruments*, vol. 88, no. 3, p. 033 505, 2017.
- [185] J. Guthrie, R. Marchand, and S. Marholm, “Inference of plasma parameters from fixed-bias multi-needle Langmuir probes (m-NLP),” *Measurement Science and Technology*, vol. 32, no. 9, p. 095 906, 2021.

- [186] R. Marchand, Y. Miyake, H. Usui, J. Deca, G. Lapenta, J.-C. Matéo-Vélez, R. Ergun, A. Sturmer, V. Génot, A. Hilgers, *et al.*, “Cross-comparison of spacecraft-environment interaction model predictions applied to solar probe plus near perihelion,” *Physics of Plasmas*, vol. 21, no. 6, p. 062 901, 2014.
- [187] J Deca, G Lapenta, R Marchand, and S. Markidis, “Spacecraft charging analysis with the implicit particle-in-cell code iPic3D,” *Physics of Plasmas*, vol. 20, no. 10, p. 102 902, 2013.
- [188] P. A. R. Lira, R. Marchand, J. Burchill, and M. Förster, “Determination of Swarm Front Plate’s Effective Cross Section From Kinetic Simulations,” *IEEE Transactions on Plasma Science*, vol. 47, no. 8, pp. 3667–3672, 2019.
- [189] H. Bridge, J. Belcher, R. Butler, A. Lazarus, A. Mavretic, J. Sullivan, G. Siscoe, and V. Vasyliunas, “The plasma experiment on the 1977 Voyager mission,” *Space Science Reviews*, vol. 21, no. 3, pp. 259–287, 1977.
- [190] J.-J. Berthelier, M. Godefroy, F. Leblanc, E. Seran, D Peschard, P Gilbert, and J Artru, “IAP, the thermal plasma analyzer on DEMETER,” *Planetary and Space Science*, vol. 54, no. 5, pp. 487–501, 2006.
- [191] A. Sharma, A. Patil, R. Haridas, and M. Parrot, “Detection of ionospheric perturbations associated with earthquake using data of IAP and ISL instruments of DEMETER satellite,” in *2011 XXXth URSI General Assembly and Scientific Symposium*, IEEE, 2011, pp. 1–4.
- [192] J. Burch, P. Reiff, J. Menietti, R. Heelis, W. Hanson, S. Shawhan, E. Shelley, M Sugiura, D. Weimer, and J. Winningham, “IMF By-dependent plasma flow and Birkeland currents in the dayside magnetosphere: 1. Dynamics Explorer observations,” *Journal of Geophysical Research: Space Physics*, vol. 90, no. A2, pp. 1577–1593, 1985.
- [193] R. Heelis and W. Coley, “East-west ion drifts at mid-latitudes observed by Dynamics Explorer 2,” *Journal of Geophysical Research: Space Physics*, vol. 97, no. A12, pp. 19 461–19 469, 1992.
- [194] M. Adrian, A. Viñas, P. Moya, and D. Wendel, “Solar wind magnetic fluctuations and electron non-thermal temperature anisotropy: Survey of WIND-SWE-VEIS observations,” *The Astrophysical Journal*, vol. 833, no. 1, p. 49, 2016.
- [195] K.-S. Chung, “Mach probes,” *Plasma Sources Science and Technology*, vol. 21, no. 6, p. 063 001, 2012.
- [196] K.-S. Chung, S.-H. Hong, and K.-H. Chung, “Measurements of Plasma Flow Velocity in DC Plasma Jets using Perpendicular and Parallel Mach Probes,” *Japanese Journal of Applied Physics*, vol. 34, no. 8R, p. 4217, 1995.
- [197] Y. Amagishi and T. Miyazaki, “Plasma flow measurements with Mach probe,” *Journal of the Physical Society of Japan*, vol. 67, no. 11, pp. 3774–3778, 1998.

- [198] Y.-S. Choi, H.-J. Woo, K.-S. Chung, M.-J. Lee, D. Zimmerman, and R. McWilliams, “Determination of plasma flow velocity by Mach probe and triple probe with correction by laser-induced fluorescence in unmagnetized plasmas,” *Japanese Journal of Applied Physics*, vol. 45, no. 7R, p. 5945, 2006.
- [199] C. S. MacLatchy, C. Boucher, D. A. Poirier, and J. Gunn, “Gundestrup: A Langmuir/Mach probe array for measuring flows in the scrape-off layer of TdeV,” *Review of Scientific Instruments*, vol. 63, no. 8, pp. 3923–3929, 1992.
- [200] J.-P. Lebreton, S Stverak, P Travnicek, M Maksimovic, D Klinge, S Merikallio, D. Lagoutte, B Poirier, P.-L. Bletly, Z. Kozacek, *et al.*, “The ISL Langmuir probe experiment processing onboard DEMETER: Scientific objectives, description and first results,” *Planetary and Space Science*, vol. 54, no. 5, pp. 472–486, 2006.
- [201] E. Seran, J.-J. Berthelie, F. Saouri, and J.-P. Lebreton, “The spherical segmented Langmuir probe in a flowing thermal plasma: numerical model of the current collection,” in *Annales Geophysicae*, Copernicus GmbH, vol. 23, 2005, pp. 1723–1733.
- [202] N. Imtiaz, R. Marchand, and J.-P. Lebreton, “Modeling of current characteristics of segmented Langmuir probe on DEMETER,” *Physics of Plasmas*, vol. 20, no. 5, p. 052903, 2013.
- [203] C. Geuzaine and J.-F. Remacle, “Gmsh: A 3-D finite element mesh generator with built-in pre-and post-processing facilities,” *International Journal for Numerical Methods in Engineering*, vol. 79, no. 11, pp. 1309–1331, 2009.
- [204] R Marchand, F Mackay, J. Lu, and K Kabin, “Consistency check of a global MHD simulation using the test-kinetic approach,” *Plasma Physics and Controlled Fusion*, vol. 50, no. 7, p. 074007, 2008.
- [205] G. Voitcu, M. Echim, and R. Marchand, “Comparative study of forward and backward test-kinetic simulation approaches,” *Computer Physics Communications*, vol. 183, no. 12, pp. 2561–2569, 2012.
- [206] A. R. Heryudono and T. A. Driscoll, “Radial basis function interpolation on irregular domain through conformal transplantation,” *Journal of Scientific Computing*, vol. 44, no. 3, pp. 286–300, 2010.
- [207] T. A. Driscoll and A. R. Heryudono, “Adaptive residual subsampling methods for radial basis function interpolation and collocation problems,” *Computers & Mathematics with Applications*, vol. 53, no. 6, pp. 927–939, 2007.
- [208] Q. Zhang, Y. Zhao, and J. Levesley, “Adaptive radial basis function interpolation using an error indicator,” *Numerical Algorithms*, vol. 76, no. 2, pp. 441–471, 2017.
- [209] Y. R. Park, T. J. Murray, and C. Chen, “Predicting sun spots using a layered perceptron neural network,” *IEEE Transactions on Neural Networks*, vol. 7, no. 2, pp. 501–505, 1996.

- [210] N. Barkhatov and S. Revunov, “Neural network classification of discontinuities in space plasma parameters,” *Geomagnetism and Aeronomy*, vol. 50, no. 7, pp. 894–904, 2010.
- [211] H. Chen, V Chandrasekar, H. Tan, and R. Cifelli, “Rainfall estimation from ground radar and TRMM precipitation radar using hybrid deep neural networks,” *Geophysical Research Letters*, vol. 46, no. 17-18, pp. 10 669–10 678, 2019.
- [212] C. M. Bishop *et al.*, *Neural networks for pattern recognition*. Oxford University Press, 1995.
- [213] T. Bazzi, R. Ismail, and M. Zohdy, “Comparative performance of several recent supervised learning algorithms,” *Learning*, vol. 1, no. 1, p. 1, 2018.
- [214] J. Zhang, “Gradient descent based optimization algorithms for deep learning models training,” *arXiv preprint arXiv:1903.03614*, 2019.
- [215] P. Goldsborough, “A tour of tensorflow,” *arXiv preprint arXiv:1610.01178*, 2016.
- [216] D. P. Kingma and J. Ba, “Adam: A method for stochastic optimization,” *arXiv preprint arXiv:1412.6980*, 2014.
- [217] S Santandrea, K Gantois, K Strauch, F Teston, E Tilmans, C Baijot, D Gerrits, A De Groof, G Schwehm, and J Zender, “PROBA2: Mission and spacecraft overview,” *Solar Physics*, vol. 286, no. 1, pp. 5–19, 2013.
- [218] European Space Agency, *Http://p2sa.esac.esa.int/p2sa/#ftp*, European Space Agency, Ed.

Appendix A:

Table A.1: Sample of the synthetic data sets for the idealise probe. I_{1-10} are the currents collected by the 10 segments, V_X and V_Y are the components of the transverse velocity, and n is the plasma density.

I_1	I_2	I_3	I_4	I_5	I_6	I_7	I_8	I_9	I_{10}	V_X	V_Y	n
10^{-8} A	m/s	m/s	10^{10} m $^{-3}$									
2.511	2.575	2.576	2.513	2.474	1.281	1.375	1.377	1.284	1.225	-97.224	319.245	18.73
1.632	1.669	1.633	1.573	1.573	0.833	0.890	0.835	0.744	0.743	-381.765	286.646	12.04
2.023	1.933	1.950	2.051	2.097	1.031	0.897	0.922	1.073	1.142	290.339	-552.216	15.11
0.904	0.898	0.872	0.863	0.883	0.465	0.455	0.415	0.401	0.431	-342.214	-86.038	6.476
10.818	10.773	10.766	10.806	10.843	5.559	5.500	5.491	5.544	5.588	8.272	-50.338	84.19
1.090	1.072	1.055	1.064	1.085	0.522	0.494	0.470	0.482	0.514	-119.318	-197.951	8.169
3.037	3.007	3.033	3.081	3.084	1.519	1.475	1.514	1.582	1.586	155.505	-124.488	22.90
0.962	0.940	0.930	0.946	0.966	0.580	0.546	0.531	0.555	0.586	-47.686	-335.975	6.446
0.607	0.599	0.595	0.600	0.607	0.303	0.291	0.284	0.291	0.303	-45.116	-146.383	4.579
0.627	0.626	0.628	0.629	0.629	0.323	0.323	0.325	0.327	0.326	33.885	-9.634	4.572
0.189	0.188	0.189	0.190	0.189	0.098	0.097	0.098	0.099	0.099	58.928	-16.949	1.160
0.359	0.378	0.398	0.392	0.368	0.152	0.182	0.214	0.205	0.166	533.022	643.129	2.540
5.659	5.923	6.128	5.987	5.700	2.660	3.023	3.308	3.111	2.714	267.740	557.536	44.500
0.669	0.659	0.651	0.657	0.668	0.338	0.321	0.309	0.318	0.336	-89.003	-191.466	4.838
11.817	11.899	12.799	13.280	12.669	5.144	5.243	6.375	7.003	6.203	753.683	67.738	112.0
13.669	12.858	12.524	13.115	13.837	8.152	7.085	6.664	7.417	8.373	-89.712	-764.198	106.0